# Analytical and numerical study of microswimming using the 'bead-spring model'

## Analytische und numerische Studie des Mikroschwimmens anhand des 'Teilchen-Feder-Modellsystems'

Der

**Naturwissenschaftlichen Fakultät**

der

**Friedrich-Alexander-Universität Erlangen-Nürnberg**

---



**FRIEDRICH-ALEXANDER
UNIVERSITÄT
ERLANGEN-NÜRNBERG**

**NATURWISSENSCHAFTLICHE
FAKULTÄT**

---

zur

**Erlangung des Doktorgrades Dr. rer. nat.**

vorgelegt von

**Jayant Pande**

aus

**Neu-Delhi, Indien**

Als Dissertation genehmigt
von der naturwissenschaftlichen Fakultät
der Friedrich-Alexander-Universität Erlangen-Nürnberg


Tag der mündlichen Prüfung:                    13. 12. 2016

Vorsitzender des Promotionsorgans:             Prof. Dr. Georg Kreimer
Gutachter                                      Prof. Dr. Ana-Sunčana Smith
                                               Prof. Dr. Jens Harting
                                               Prof. Dr. Markus Deserno (Univ. Pittsburgh)

*To my parents*

*In memory of my grandparents and aunt*

# Contents

# Part I

# Summary

# Summary

In this thesis we use the bead-spring microswimmer design as a model system to study mechanical microswimming. The basic form of such a swimmer was introduced as the 'three-sphere swimmer' in Najafi and Golestanian [2004] and has found wide use in theoretical, numerical and experimental research. In our work, we have modified and extended the model in various ways, which, as explained in this thesis, allow us to gain insight into many general principles of microswimming, for instance the interplay between fluid drag force and swimmer elasticity in determining the efficiency of motion. The work presented here consists of both analytical solution of the equations of motion in the different investigated cases and corresponding numerical study.

We begin this thesis with an introduction (chapter 0) to the world of low Reynolds number locomotion, and in particular to that of microswimming, explaining the current state of knowledge in the field regarding biological microswimmers and models thereof, both theoretical and experimental. We then explain in chapter 1 the details of, and the differences between, the Golestanian three-sphere swimmer and our bead-spring model. The Golestanian model consists of three spheres aligned along one line with the distances between two neighbouring spheres in each pair being changed in a controlled manner (which determines the swimming stroke), leading to propagation of the assembly. In the bead-spring model, we replace the specification of the stroke by that of the forces driving the motion, allow non-spherical and shape-varying beads in the design, and, in the last part of the thesis, investigate swimmer motion beyond the low Reynolds number (Stokes) regime. These changes result in a more comprehensive description of the motion with the influences of different factors such as the fluid viscosity, the energy input, the elasticity of the swimmer and its instantaneous and mean shapes all becoming important, unlike in the Golestanian swimmer where these influences

are all subsumed in the specification of the swimming stroke. We use our model to calculate the velocity of our swimmer both with rigid and deformable spheres, and to different orders in the relative magnitude of bead size and bead separation.

In chapter 2, we explain the two simulation methods used by us, the waLBerla system and the LB3D code. Both of these are based on the lattice Boltzmann method (LBM), and their main difference lies in their being coupled respectively to a rigid body physics engine, which allows us to simulate any combinations of rigid objects in fluids, and an immersed boundary method (IBM) solver with which we can simulate deformable membranes.

In chapter 3, we compare the swimmer velocities as obtained from theory and the two simulation systems for swimmers with rigid beads. We find good agreement which expectedly becomes better as the simulation systems become more idealised, such as by an increased simulation domain size and smaller Reynolds numbers of motion. We also explain how and why some microswimmers swim faster in more viscous fluids. We show that this puzzling phenomenon, observed experimentally for many species of bacteria, can occur in fully Newtonian fluids–a result which runs counter to the prevailing wisdom in the field–and arises from the dichotomous effects that the drag force has on motion at low Reynolds number. In particular, the so-called 'aberrant' regime of motion, wherein the swimmer gets quicker as the fluid viscosity increases, is expected to show up for all mechanical microswimmers swimming due to the influence of sufficiently weak driving forces. The simulations fully support the theoretical prediction for the onset of the aberrant regime.

In chapter 4, we use the LB3D code to simulate swimmers with deformable beads, to answer the question of whether passive shape changes–which are the changes in shape of a deformable swimmer in response to the fluid, not as a driving mechanism for motion–can be beneficial for swimming. This relates to the as yet unexplained phenomenon of *metaboly*, wherein spirochetes, which otherwse swim by flagellar propulsion, regularly change their shapes during their motion, without its being clear whether these shape changes are beneficial for locomotion, for food capture, or some other purpose. Restricting our attention to our model, we show that passive shape changes can result in both faster and slower swimming, and that this response depends on the swimmer's elasticity. The theory accurately predicts both the regimes, where the shape changes respectively promote and hinder the motion, that are visible in the simulations.

In chapter 5 we look at active effects of shape, by studying the different swimming speeds of swimmers with rigid beads of different shapes. For this we allow the beads to be ellipsoids of revolution, and calculate the optimal aspect ratios of the ellipsoids (given a fixed volume or surface area) that maximize the swimming velocity for equal driving forces. We find that depending on the stiffness coefficient of the springs, the same shape (for instance, the ellipsoid of the lowest drag

coefficient) may result in the fastest or the slowest swimmer, owing to the different energy costs of deforming springs of low and high stiffness. We show that this happens due to the swimming in the two cases being dominated either by a reduction in the drag force opposing the beads or by the hydrodynamic interaction amongst them.

In chapter 6 we expand the scope of our study to incorporate the onset of non-Stokesian effects in microswimming. Using the waLBerla simulation system, we systematically increase the forces driving the beads, thereby raising the Reynolds number of motion and ultimately pushing the swimmer beyond the Stokes regime. We show that the limit of this regime may be determined by matching the coasting exhibited by the swimmer to that of an underdamped harmonic oscillator, with the damping constant arising from the Stokes drag law. The effective radius of the swimmer thus found agrees excellently with that obtained from theory, and indicates that inertial effects in microswimming set in at increased driving forces (or, equivalently, larger swimming strokes) or at increased swimmer masses. Building on this heuristic investigation, we modify our theoretical model by adding a mass acceleration term in the governing equations of motion of the three beads, and show that solution of the resultant system predicts swimmer velocities which are in good agreement with those observed in simulations (and which differ significantly from the Stokes-regime calculation results). These calculations confirm the identification of the Stokes, non-Stokes and intermediate regimes seen in the simulations.

We conclude in chapter 7 by a discussion of the main results presented in our work, and future possibilities for its extension.

16

# Zusammenfassung

In dieser Dissertation nutzen wir das Teilchen-Feder Design eines Mikroschwimmers als ein Modellsystem, um mechanisches Mikroschwimmen zu untersuchen. Die Grundform eines solchen Schwimmers wurde als der 'Drei-Kugel-Schwimmer' in Najafi and Golestanian [2004] eingeführt und wurde im Folgenden in theoretischen, numerischen und experimentallen Untersuchungen ausgiebig genutzt. In unserer Arbeit haben wir das Grundmodell auf verschiedene Arten modifiziert und erweitert. Wie in dieser Dissertation beschrieben erlaubt uns dies Einblicke in viele grundlegende Prinzipien des Mikroschwimmens wie zum Beispiel das Zusammenspiel zwischen Widerstandskräften des Fluids und der Elastizität des Schwimmers um die Effizienz der Bewegung zu ermitteln. Die hier präsentierte Arbeit ist eine Untersuchung, die sowohl aus dem analytischen Lösen der Bewegungsgleichungen für die verschiedenen Fälle, als auch aus den entsprechenden numerischen Studien besteht.

Wir beginnen diese Dissertation mit einer allgemeinen Einleitung (Kapitel 0) in die Welt der Bewegungen bei kleinen Reynoldszahlen, insbesondere in die des Mikroschwimmens. Dann klären wir den aktuellen Wissensstand über biologische Mikroschiwmmer um dann das Kapitel mit theoretischen und experimentellen Modellen dazu zu beschließen. Danach erklären wir in Kapitel 1 die Details des Golestanian'schen Drei-Kugel-Schwimmers und die Unterschiede zu unserem Teilchen-Feder Modell. Im Golestanian'schen Modell sind die drei Kugeln entlang einer Linie ausgerichtet und die Abstände zwischen zwei benachbarten Kugeln werden für jedes Paar in einer kontrollierten Art und Weise verändert, was den Schwimmschlag bestimmt und zu einer Bewegung des Schwimmers führt. Wir ersetzen in dem Teilchen-Feder Modell die Vorgaben an den Schwimmschlag mit denen der treibenden Kräfte für die Bewegung, lassen auch nicht-sphärische und formverändernde Teilchen in unserem Design zu und un-

17

tersuchen im letzten Teil der Dissertation die Bewegungen des Schwimmers jenseits des Stokes-Regimes. Diese Änderungen resultieren in einer allgemeineren Beschreibung der Bewegung unter dem Einfluss der verschiedenen Akteure wie der Fluidviskosität, dem Energieeintrag, der Elastizität des Schwimmers und seiner instantanen und mittleren Form, wobei jeder einen wichtigen Beitrag zum Schwimmverhalten leistet. Im Gegensatz dazu werden diese Einflüsse im Golestanian'schen Schwimmer in den Vorgaben an den Schwimmschlag zusammengefasst. In unserem Modell berechnen wir die Geschwindigkeit des Schwimmers sowohl mit festen, als auch mit verformbaren Teilchen und verändern darüber hinaus das Verhältnis aus Teilchengrößen zu den Abständen zwischen den Teilchen.

In Kapitel 2 erklären wir die beiden von uns genutzten Simulationsmethoden waLBerla und LB3D. Beide Simulationsmethoden basieren auf der Lattice-Boltzmann-Methode (LBM) und unterscheiden sich hauptsächlich darin, wie sie an Simulationsmethoden für die Bewegung der Teilchen gekoppelt sind. Bei waLBerla handelt es sich um eine Physik-Engine für starre Körper, die jede beliebige Kombination von starren Körpern in einem Fluid simulieren kann. Im Gegensatz dazu handelt es sich bei LB3D um die 'Immersed Boundary Methode' (IBM), mit der schließlich auch deformierbare Membranen simuliert werden können.

In Kapitel 3 vergleichen wir die Theorie mit den beiden Simulationsmethoden anhand der Geschwindigkeiten für Schwimmer mit starren Teilchen. Wir erhalten eine gute Übereinstimmung, die wie erwartet noch besser wird, wenn das simulierte System weiter idealisiert wird, z.B. durch eine größere Simulationsumgebung oder kleinere Reynoldszahlen. Wir erklären zudem ob und wie einige Mikroschwimmer schneller in viskoseren Fluiden schwimmen können. Wir zeigen, dass dieses faszinierende und für viele Bakterienarten experimentell beobachtete Phänomen in einem vollkommenen Newton'schen Fluid auftreten kann – ein Ergebnis, das der vorherrschenden Lehrmeinung des Feldes widerspricht. Dieses Phänomen lässt sich durch einen zweigeteilten Effekt von Widerstandskräften des Fluids auf die Bewegung bei kleinen Reynoldszahlen erklären. Insbesondere das so genannten aberrante Regime, in dem der Schwimmer schneller wird als die Fluidviskosität erhöht wird, wird für alle mechanische Mikroschwimmer, die unter dem Einfluss von ausreichend kleinen Antriebskräften schwimmen, erwartet. Auch unsere Simulationen unterstützen die theoretischen Vorhersagen für das aberrante Regime.

In Kapitel 4 nutzen wir den LB3D Simulationscode für Schwimmer mit deformierbaren Teilchen, um Fragen bezüglich passive Formänderungen, d.h. Formänderungen von deformierbaren Teilchen aufgrund des Einflusses des Fluids und nicht als Mechanismus für eine Fortbewegung, beantworten zu können. Diese Fragestellung ist mit dem bislang unerklärten Phänomen 'Metaboly' verbunden, wo Spirochetes, die sonst durch einen Antrieb durch ihr Flagellum schwimmen, ihre Form während der Bewegung verändern. Dabei ist noch unklar, ob diese

Formänderungen für die Fortbewegung, zur Jagd von Nahrung oder für andere Gründe nützlich sind. Bezogen auf unser Modell zeigen wir, dass passive Formänderungen sowohl schnelleres als auch langsameres Schwimmen verursachen können und dass das konkrete Ergebnis von der Elastizität des Schwimmers abhängt. Die Theorie sagt die beiden, in der Simulation gefundenen Regime präzise voraus.

In Kapitel 5 untersuchen wir den Einfluss der Teilchenform auf die Schwimmgeschwindigkeit. Dafür betrachten wir die Teilchenkörper als Ellipsoide und berechnen ihr optimales Aspektverhältnis unter einem gegebenen Volumen oder einer gegebenen Oberfläche, das die Schwimmgeschwindigkeit für gleiche Antriebskräfte maximiert. Als Funktion der Federstärke beobachten wir, dass die gleiche Form, wie zum Beispiel der Ellipsoid für den geringsten Widerstandskoeffizienten, zum schnellsten oder zum langsamsten Schwimmer führen kann. Der Grund dafür liegt in den verschiedenen energetischen Kosten für die Verformung von Federn mit verschiedenen Federstärken. Des Weiteren zeigen wir, dass dieser Effekt entsteht, weil die Schwimmbewegungen in den beiden Fällen entweder durch eine Reduktion der Widerstandskräfte entgegen der Teilchen oder durch die hydrodynamische Wechselwirkung zwischen den Teilchen bestimmt wird.

In Kapitel 6 erweitern wir die Reichweite unserer Untersuchung durch die Betrachtung von Effekten auf das Mikroschwimmen jenseits des Stokes-Regimes. Mit Hilfe der waLBerla-Simulationsmethode können wir systematisch die bestimmenden Kräfte auf die Teilchen und damit die Reynoldszahlen erhöhen, so dass schließlich der Schwimmer das Stokes-Regime verlässt. Wir zeigen, dass die Grenzen dieses Regimes durch eine Abbildung des Schwimmers auf einen schwach gedämpften harmonischen Oszillator beschrieben werden kann. Die Abklingkonstante der Dämpfung ist dabei durch das Stokes'sche Gesetz gegeben. Der dafür gefundene effektive Radius des Schwimmers ist in außerordentlich guter Übereinstimmung mit dem Radius aus der Theorie. Dies zeigt, dass Trägheitskräfte für das Mikroschwimmen relevant werden, sobald die Antriebskräfte (oder entsprechend die Schwimmschläge) größer oder die Schwimmer massiver werden. Aufbauend auf dieser heuristischen Untersuchung modifizieren wir unser theoretisches Modell durch Hinzufügen eines Beschleunigungsterms für die Massen zu den bestimmenden Gleichungen für die drei Teilchen. Die Lösungen dieses modifizierten Systems sagen Schwimmergeschwindigkeiten voraus, die in guter Übereinstimmung mit den in unseren Simulationen beobachteten Geschwindigkeiten stehen, und dabei signifikant von den Lösungen im Stokes-Regime abweichen. Diese Rechnungen bestätigen das Stokes-, das Nicht-Stokes- und das dazwischen liegende Regime, die alle in Simulationen beobachtet wurden.

Wir beenden diese Arbeit mit einer Diskussion der wichtigsten Ergebnisse und zukünftigen Weiterentwicklungen in Kapitel 7.

In dieser Dissertation nutzen wir das Teilchen-Feder Design eines Mikroschwimmers als ein Modellsystem, um mechanisches Mikroschwimmen zu untersuchen.

20

Die Grundform eines solchen Schwimmers wurde als der 'Drei-Kugel-Schwimmer' in Najafi Golestanian, Phys. Rev. E (2004) eingefhrt und wurde im Folgenden in theoretischen, numerischen und experimentallen Untersuchungen ausgiebig genutzt. In unserer Arbeit haben wir das Grundmodell auf verschiedene Arten modifiziert und erweitert. Wie in dieser Dissertation beschrieben erlaubt uns dies Einblicke in viele grundlegende Prinzipien des Mikroschwimmens wie zum Beispiel das Zusammenspiel zwischen Widerstandskrften des Fluids und der Elastizitt des Schwimmers um die Effizienz der Bewegung zu ermitteln. Die hier prsentierte Arbeit ist eine Untersuchung, die sowohl aus dem analytischen Lsen der Bewegungsgleichungen fr die verschiedenen Flle, als auch aus den entsprechenden numerischen Studien besteht.

Wir beginnen diese Dissertation mit einer allgemeinen Einleitung (Kapitel 0) in die Welt der Bewegungen bei kleinen Reynoldszahlen, insbesondere in die des Mikroschwimmens. Dann klren wir den aktuellen Wissensstand ber biologische Mikroschiwmmer um dann das Kapitel mit theoretischen und experimentellen Modellen dazu zu beschlieen. Danach erklren wir in Kapitel 1 die Details des Golestanian'schen Drei-Kugel-Schwimmers und die Unterschiede zu unserem Teilchen-Feder Modell. Im Golestanian'schen Modell sind die drei Kugeln entlang einer Linie ausgerichtet und die Abstnde zwischen zwei benachbarten Kugeln werden fr jedes Paar in einer kontrollierten Art und Weise verndert, was den Schwimmschlag bestimmt und zu einer Bewegung des Schwimmers fhrt. Wir ersetzen in dem Teilchen-Feder Modell die Vorgaben an den Schwimmschlag mit denen der treibenden Krfte fr die Bewegung, lassen auch nicht-sphrische und formverndernde Teilchen in unserem Design zu und untersuchen im letzten Teil der Dissertation die Bewegungen des Schwimmers jenseits des Stokes-Regimes. Diese nderungen resultieren in einer allgemeineren Beschreibung der Bewegung unter dem Einfluss der verschiedenen Akteure wie der Fluidviskositt, dem Energieeintrag, der Elastizitt des Schwimmers und seiner instantanen und mittleren Form, wobei jeder einen wichtigen Beitrag zum Schwimm-verhalten leistet. Im Gegensatz dazu werden diese Einflsse im Golestanian'schen Schwimmer in den Vorgaben an den Schwimmschlag zusammengefasst. In unserem Modell berechnen wir die Geschwindigkeit des Schwimmers sowohl mit festen, als auch mit verformbaren Teilchen und verndern darber hinaus das Verhltnis aus Teilchengren zu den Abstnden zwischen den Teilchen.

In Kapitel 2 erklren wir die beiden von uns genutzten Simulationsmethoden Walberla und LB3D. Beide Simulationsmethoden basieren auf der Lattice-Boltzmann-Methode (LBM) und unterscheiden sich hauptschlich darin, wie sie an Simulationsmethoden fr die Bewegung der Teilchen gekoppelt sind. Bei Walberla handelt es sich um eine Physik-Engine fr starre Krper, die jede beliebige Kombination von starren Krpern in einem Fluid simulieren kann. Im Gegensatz dazu handelt es sich bei LB3D um die 'Immersed Boundary Methode' (IBM), mit

der schlielich auch deformierbare Membranen simuliert werden knnen.

In Kapitel 3 vergleichen wir die Theorie mit den beiden Simulationsmetho-den anhand der Geschwindigkeiten fr Schwimmer mit starren Teilchen. Wir erhalten eine gute bereinstimmung, die wie erwartet noch besser wird, wenn das simulierte System weiter idealisiert wird, z.B. durch eine grere Simulations-umgebung oder kleinere Reynoldszahlen. Wir erklren zudem ob und wie einige Mikroschwim-mer schneller in viskoseren Fluiden schwimmen knnen. Wir zeigen, dass dieses faszinierende und fr viele Bakterienarten experimentell beobachtete Phnomen in einem vollkommenen Newton'schen Fluid auftreten kann – ein Ergebnis, das der vorherrschenden Lehrmeinung des Feldes widerspricht. Dieses Phnomen lsst sich durch einen zweigeteilten Effekt von Widerstandskrften des Fluids auf die Bewe-gung bei kleinen Reynoldszahlen erklren. Insbesondere das so genannten "aber-rante" Regime, in dem der Schwimmer schneller wird als die Fluidviskositt erht wird, wird fr alle mechanische Mikroschwimmer, die unter dem Einfluss von aus-reichend kleinen Antriebskrften schwimmen, erwartet. Auch unsere Simulationen untersttzen die theoretischen Vorhersagen fr das aberrante Regime.

In Kapitel 4 nutzen wir den LB3D Simulationscode fr Schwimmer mit de-formierbaren Teilchen, um Fragen bezglich passive Formnderungen, d.h. Form-nderungen von deformierbaren Teilchen aufgrund des Einflusses des Fluids und nicht als Mechanismus fr eine Fortbewegung, beantworten zu knnen. Diese Fragestel-lung ist mit dem bislang unerklrten Phnomen 'Metaboly' verbunden, wo Spiro-chetes, die sonst durch einen Antrieb durch ihr Flagellum schwimmen, ihre Form whrend der Bewegung verndern. Dabei ist noch unklar, ob diese Formnderun-gen fr die Fortbewegung, zur Jagd von Nahrung oder fr andere Grnde ntzlich sind. Bezogen auf unser Modell zeigen wir, dass passive Formnderungen sowohl schnelleres als auch langsameres Schwimmen verursachen knnen und dass das konkrete Ergebnis von der Elastizitt des Schwimmers abhngt. Die Theorie sagt die beiden, in der Simulation gefundenen Regime przise voraus.

In Kapitel 5 untersuchen wir den Einfluss der Teilchenform auf die Schwim-mgeschwindigkeit. Dafr betrachten wir die Teilchenkrper als Ellipsoide und berech-nen ihr optimales Aspektverhltnis unter einem gegebenen Volumen oder einer gegebenen Oberflche, das die Schwimmgeschwindigkeit fr gleiche Antriebskrfte maximiert. Als Funktion der Federstrke beobachten wir, dass die gleiche Form, wie zum Beispiel der Ellipsoid fr den geringsten Widerstandskoeffizienten, zum schnellsten oder zum langsamsten Schwimmer fhren kann. Der Grund dafr liegt in den verschiedenen energetischen Kosten fr die Verformung von Federn mit ver-schiedenen Federstrken. Des Weiteren zeigen wir, dass dieser Effekt entsteht, weil die Schwimmbewegungen in den beiden Fllen entweder durch eine Reduktion der Widerstandskrfte entgegen der Teilchen oder durch die hydrodynamische Wech-selwirkung zwischen den Teilchen bestimmt wird.

In Kapitel 6 erweitern wir die Reichweite unserer Untersuchung durch die Be-

trachtung von Effekten auf das Mikroschwimmen jenseits des Stokes-Regimes. Mit Hilfe der Walberla-Simulationsmethode knnen wir systematisch die bestimmenden Krfte auf die Teilchen und damit die Reynoldszahlen erhhen, so dass schlielich der Schwimmer das Stokes-Regime verlsst. Wir zeigen, dass die Grenzen dieses Regimes durch eine Abbildung des Schwimmers auf einen schwach gedmpften harmonischen Oszillator beschrieben werden kann. Die Abklingkonstante der Dmpfung ist dabei durch das Stokes'sche Gesetz gegeben. Der dafr gefundene effektive Radius des Schwimmers ist in außerordentlich guter bereinstimmung mit dem Radius aus der Theorie. Dies zeigt, dass Trgheitskrfte fr das Mikroschwimmen relevant werden, sobald die Antriebskrfte (oder entsprechend die Schwimmschlge) grer oder die Schwimmer massiver werden. Aufbauend auf dieser heuristischen Untersuchung modifizieren wir unser theoretisches Modell durch Hinzufgen eines Beschleunigungsterms fr die Massen zu den bestimmenden Gleichungen fr die drei Teilchen. Die Lsungen dieses modifizierten Systems sagen Schwimmergeschwindigkeiten voraus, die in guter bereinstimmung mit den in unseren Simulationen beobachteten Geschwindigkeiten stehen, und dabei signifikant von den Lsungen im Stokes-Regime abweichen. Diese Rechnungen besttigen das Stokes-, das Nicht-Stokes- und das dazwischen liegende Regime, die alle in Simulationen beobachtet wurden.

Wir beenden diese Arbeit mit einer Diskussion der wichtigsten Ergebnisse und zuknftigen Weiterentwicklungen in Kapitel 7.

# Part II

# Thesis

*0*

# Introduction

In this thesis we study **mechanically-driven microswimmers** (hereafter also often called simply 'swimmers', since it is clear that we are always concerned with mechanical swimming at the micro-scales, unless explicitly stated otherwise). As the name suggests, these are entities typically of microscopic sizes which can utilise mechanical forces to swim, or propel themselves autonomously under their own agency, in fluids. Their dimensions are usually of the order of microns, although there is no precise size limitation. Biologically most micro-organisms such as bacteria, archaea, algae, protozoa, etc., can be classified as microswimmers, and indeed a great part–a majority, according to some studies–of the earth's biomass can be included in this category [Whitman *et al.*, 1998, Biddle *et al.*, 2006, Lipp *et al.*, 2008, Kallmeyer *et al.*, 2012]. In addition to these natural organisms, there are many existing and planned artificial contraptions which are of microscopic dimensions and swim in fluid environments, and are thus also examples of microswimmers. Such contraptions include drug delivery systems[Tierno *et al.*, 2008a, Scogna *et al.*, 2011, Patra *et al.*, 2013], lab-on-a-chip devices [Craighead, 2006, El-Ali *et al.*, 2006, Yeo *et al.*, 2011, Sackmann *et al.*, 2014], medical probes [Yager *et al.*, 2006, Nelson *et al.*, 2010, Gervais *et al.*, 2011, JianFeng and Cho, 2014], etc.

Our interest will be centred on the motion of mechanical microswimmers. Given their dominance in terms of the numbers of individuals as well as the total biomass, it should come as no surprise that the way biological microswimmers interact with each other and with their environments has vital consequences for all life on earth. Both harmful and salubrious effects of micro-organisms (also called microbes) on the health of other organisms are well-studied [Costerton *et al.*, 1999, Hudault *et al.*, 2001, Wanke, 2001, Collignon, 2009, Merchant *et al.*, 2012]. Similarly, for artificial microswimmers it is a crucially important task to fully understand and predict the characteristics of their motion, if the purposes for

which they are fabricated are to be carried out efficiently and safely.

In this thesis therefore we study the physical features of the motion of microswimmers. Our analysis will be focussed on one particular model of a microswimmer, the **bead-spring swimmer** (treated in detail in chapter 1), but our guiding principle and purpose throughout will be to extract wisdom about the general features of microswimming using this model. We shall focus exclusively on the physical questions involved, deriving from the fluid dynamics of the problem, and show that in most cases, the features of swimming at micro-scales run directly counter to those at the macro-scale. Note that there are many microswimmers in experiment and theory which are not mechanically driven, such as those swimming due to chemical reactions [Fournier-Bidoz *et al.*, 2005, Golestanian *et al.*, 2005, Howse *et al.*, 2007, Rückner and Kapral, 2007, Tao and Kapral, 2008, Popescu *et al.*, 2010, Baraban *et al.*, 2012] or thermal expansion of parts of the swimmer [Jiang *et al.*, 2010, Buttinoni *et al.*, 2012, de Buyl and Kapral, 2013, Braun and Cichos, 2013]. Such swimmers lie outside the purview of this thesis.

This introductory chapter is structured as follows. We start with a description of the main concepts involved in treating mathematical problems of motion at low Reynolds numbers (see section 0.1), and then provide a brief overview of microswimmers in general and artificial microswimmers in particular, with a special focus on the different mathematical models of microswimmers that exist and numerical and experimental realisations of the same. We finish with a description of the various chapters in this thesis.

## 0.1 Fundamental concepts of low Reynolds number motion

The world of microswimming is typically a world where a lot of effort has to be expended for motion, as seen in the typically low efficiencies of motion of microswimmers [Purcell, 1997, Avron *et al.*, 2004, Chattopadhyay *et al.*, 2006, Alouges *et al.*, 2009, Osterman and Vilfan, 2011]. The main reason for this is the immense frictional resistance to motion that microswimmers habitually face in fluids, due to their microscopic sizes and negligible masses. The mathematical reflection of this statement is in the very small Reynolds numbers $Re$ [Rott, 1990] of motion of microswimmers, and in the next section we explain the main features of flows with small $Re$. Note however that the condition of negligibly small $Re$ does not *always* obtain, and in some cases, for instance the one treated by us in chapter 6, the low $Re$ description becomes invalid.

### 0.1.1 The Navier-Stokes and the Stokes equations

The flow of a general fluid treated as a continuum is described by the famous Navier-Stokes (N-S) equation, which was formulated by the physicists Claude-Louis Navier and George Gabriel Stokes in the 19$^{th}$ century. For an incompressible Newtonian fluid of a constant density, which is the only case we will consider in this thesis, the Navier-Stokes equation reads

$$\rho\left(\frac{\partial\mathbf{u}(\mathbf{r},t)}{\partial t} + (\mathbf{u}(\mathbf{r},t)\cdot\nabla)\,\mathbf{u}(\mathbf{r},t)\right) = -\nabla p(\mathbf{r},t) + \eta\nabla^2\mathbf{u}(\mathbf{r},t) + \mathbf{f}(\mathbf{r},t), \quad (0.1)$$

where $\rho$ and $\eta$ are the density and the dynamic viscosity of the fluid, respectively, $\mathbf{u}(\mathbf{r},t)$ and $p(\mathbf{r},t)$ are its velocity and pressure, respectively, at the point $\mathbf{r}$ at the time instant $t$, and $\mathbf{f}(\mathbf{r},t)$ is the force density on the fluid at the same point and the same instant of time. An incompressible fluid additionally satisfies the equation

$$\nabla\cdot\mathbf{u}(\mathbf{r},t) = 0, \quad (0.2)$$

which is simply a statement of the conservation of mass (the equation of continuity) in this case.

The Navier-Stokes equation, while a great success in describing continuum flow in all known scenarios, is unfortunately very difficult–and, as yet, seemingly impossible–to solve in the general case, so much so that it has been named as one of the famous seven Millenium Problems in mathematics, each carrying a prize money of USD 1 million for solution [Carlson *et al.*, 2006]. Particular instances of the equation therefore necessitate appropriate simplifications which may facilitate solution while still describing the phenomena in question reasonably accurately. Fortunately, one such simplification is easily done in the world of microswimming. For this, consider a microswimmer with a typical length dimension $L$, a typical velocity $U$, a mass $M$ and a friction coefficient $\gamma$. By non-dimensionalising the different terms in Eq. (0.1) with appropriate combinations of these variable, we get the equation [Dhont, 1996]

$$\left(\frac{\rho L^2\gamma}{M\eta}\right)\frac{\partial\mathbf{u}'}{\partial t'} + \left(\frac{\rho LU}{\eta}\right)(\mathbf{u}'\cdot\nabla)\,\mathbf{u}' = -\nabla'p' + \nabla'^2\mathbf{u}' + \mathbf{f}', \quad (0.3)$$

where the primes denote non-dimensional counterparts of the respective unprimed variables. Here time has been non-dimensionalised as $t' = t/(M/\gamma)$, which means that over the diffusive time scale $\tau_D \gg M/\gamma$ (which is usually the time scale of interest for microswimmers), the time derivative of the velocity $\partial\mathbf{u}'/\partial t'$, both due to friction and due to changes in the external force $\mathbf{f}'$, is zero [Dhont, 1996]. For microswimmers and colloidal particles in general, it turns out that the

Reynolds number *Re* of the flow, defined as

$$Re = \frac{\rho L U}{\eta} \tag{0.4}$$

is usually much smaller than 1. In that case the second term in Eq. (0.1) can also be neglected, and we finally have the following equation for the original unprimed variables,

$$\eta \nabla^2 \mathbf{u}\,(\mathbf{r}, t) - \nabla p\,(\mathbf{r}, t) + \mathbf{f}\,(\mathbf{r}, t) = 0, \tag{0.5}$$

which is the famous Stokes equation. If the flow in a fluid in a given scenario can be described well by Eq. (0.5), we will say that the fluid (or the flow, or the motion) is in the **Stokes regime** (or **Stokes flow**). When this does not happen, then we shall say that the fluid (or motion, etc.) is in the **non-Stokes regime** (or **non-Stokes flow**). The immense theoretical simplification contained within the Stokes equation in comparison to the Navier Stokes equation is the absence of the non-linear term in velocity, $(\mathbf{u} \cdot \nabla)\,\mathbf{u}$, and of the time-derivative $\partial \mathbf{u}/\partial t$. Both of these features impart very interesting properties to the motion described by the Stokes equation, as we briefly explain in the following sections. Note that the Reynolds number of motion is never strictly zero, so the Stokes equation never exactly describes the fluid flow. In most cases relevant to microswimming, however, it turns out to be conveniently accurate.

## 0.1.2  Green's function of the Stokes equation: the Oseen tensor

Due to the linearity of the Stokes equation (0.5), the velocity at each point in a fluid in the Stokes regime is proportional to a force acting on it at any point. The proportionality is specified by the Oseen tensor $\mathbf{T}(\mathbf{r})$, such that

$$\mathbf{u}(\mathbf{r}) = \mathbf{T}(\mathbf{r} - \mathbf{r}_0) \cdot \mathbf{f}_0, \tag{0.6}$$

where $\mathbf{f}_0$ is a force applied at the point $\mathbf{r}_0$ in the fluid. The Oseen tensor is given by [Oseen, 1927]

$$\mathbf{T}(\mathbf{r}) = \frac{1}{8\pi\eta r}\left(\mathbb{I} + \frac{\mathbf{rr}}{r^2}\right). \tag{0.7}$$

Mathematically the Oseen tensor is the Green's function for the fluid velocity of the Stokes equation which admits such a function since it is linear. Due to its fundamental importance in describing the velocity fields in Stokes flow, it is also called the **stokeslet**.

In a similar manner, the Green's function of the Stokes equation for the pressure $p(\mathbf{r})$ can also be found, since the equation (0.5) is also linear for the pressure.

The resulting tensor is called the pressure tensor $\mathbf{g}(\mathbf{r})$, and is given by

$$\mathbf{g}(\mathbf{r}) = \frac{\mathbf{r}}{4\pi r^3}. \qquad (0.8)$$

The equation analogous to Eq. (0.6) describing the pressure field everywhere in the fluid is

$$p(\mathbf{r}) = \mathbf{g}(\mathbf{r} - \mathbf{r}_0) \cdot \mathbf{f}_0, \qquad (0.9)$$

where again $\mathbf{f}_0$ is a point force applied at $\mathbf{r}_0$. Lastly, due again to the linearity of the Stokes equation, equations (0.6) and (0.9) can be generalised to distributions of applied forces, by integrating over the individual point contributions in the fluid [Dhont, 1996].

An important consequence of the form of the velocity-force relation in Eq. (0.6) is the anisotropy with regard to the direction. It is easy to see that the flow velocity $\mathbf{u}_{\parallel}(\mathbf{r})$ in the direction of the applied force $\mathbf{f}_0$ equals $\mathbf{f}_0 / (4\pi\eta|\mathbf{r}|)$, while the flow velocity $\mathbf{u}_{\perp}(\mathbf{r})$ perpendicular to $\mathbf{f}_0$ equals $\mathbf{f}_0 / (8\pi\eta|\mathbf{r}|)$. This anisotropy means that by changing their shapes suitably, microswimmers can succeed in eliciting different drag forces from the fluid at different points during their motion, and this can be a vital part of their swimming strategy [Childress, 1981].

## 0.1.3   Kinematic reversibility

In the Stokes equation (0.5), there is no explicit time-dependence, since the time derivative of the velocity field $\partial\mathbf{u}/\partial t$ in Eq. (0.1) has been disposed of in arriving at Eq. (0.5). This results in the curious effect of making the fluid everywhere, till infinity if the domain is not bounded, respond perfectly instantaneously to any forces applied anywhere within the domain. This also means that if over time the applied forces within the fluid are reversed, the flow will reverse perfectly too. This property is sometimes called **kinematic reversibility** (where the qualifier 'kinematic' distinguishes this property from the concept of reversibility in thermodynamics; viscous flows constantly dissipate energy and are in that respect clearly thermodynamically irreversible). A very striking demonstration of this was presented by Taylor in a famous video in which a mixture of two coloured liquids (of sufficiently high viscosities so as to impart Stokesian characteristics to the flows) was made to demix almost perfectly, simply by reversing the stirring mechanism which caused the two liquids to mix in the first place [Taylor, 1967].

This fact has biological consequences for the motion of organisms in the Stokes regime. For instance, consider a swimmer like a scallop with only one degree of freedom of movement, such as the ability to open and close its mouth. In flow that is perfectly Stokesian, any distance that the scallop traverses in the length of time in which it closes its mouth is negated exactly by the negative dis-
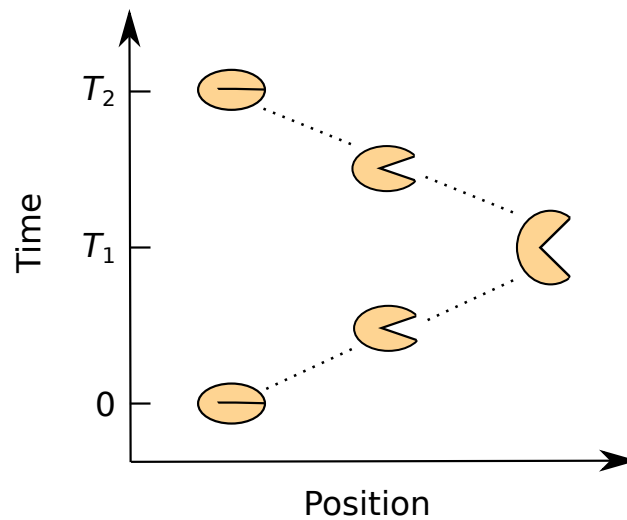
Figure 0.1: The net zero motion at Stokes flow of a scallop which can only open and close its mouth. The distance covered in the first half-cycle is cancelled by the negative distance covered in the second half-cycle.

tance covered in the time period during which it opens its mouth (Fig. 0.1). The net effect is of the scallop not swimming at all over the course of the entire swimming motion. A related feature is that in the Stokes regime the rate of applying the force in the fluid is immaterial, so that for a swimmer, the net distance covered in two cycles in which the same shape transformations are carried out is the same, irrespective of whether the two cycles are of equal duration or not. The impossibility of motion by a scallop in Stokes flow, and in general by any swimmer with a single degree of freedom and executing reversible strokes, was highlighted by Purcell in a famous lecture in 1977 [Purcell, 1977], and has come to be known as **Purcell's scallop theorem**. A motion where the strokes executed are reversible in time is also termed as 'reciprocal'. Recently Bet *et al*. have reformulated the scallop theorem in a general way, showing explicitly that a stroke is reciprocal and leads to no net movement if the area enclosed by it in the internal coordinate space is zero [Bet *et al.*, 2016].

In Stokes flow, therefore, a minimum of two degrees of freedom are required in order for persistent motion to occur (an exception to this being motion with a helical screw, where reciprocal motion is not required in order to return the screw to its initial configuration). A scallop with just one degree of freedom does swim in the ocean, of course, and the reason is that it inhabits a conveniently non-Stokesian world, where the rate of change of shapes does become important due to inertia and the scallop can exploit this fact by opening and closing its mouth at different speeds to gain a net displacement per cycle.

## 0.1.4   Nature of swimming: pushers, pullers and neutral swimmers

It is easy to see from Eqs. (0.6) and (0.7) that in the far field limit of $|\mathbf{r}| \to 0$, the velocity field due to a stokeslet, which is a non-zero force applied at a single point in the fluid, drops off as $|\mathbf{r}|^{-1}$. Microswimmers, however, have a net zero force and torque acting on them (assuming they are swimming autonomously), and to the leading order are therefore force dipoles, unlike the stokeslet which is a force monopole. A multipole expansion of the velocity fields produced by their motion, in terms of powers of $|\mathbf{r}|^{-1}$, therefore results in the leading order being at least two, *i.e.* the leading order term is $|\mathbf{r}|^{-2}$ (unless even the second order is absent, as can happen when, for instance, particular symmetries in the swimmer design cancel off the $|\mathbf{r}|^{-2}$ terms in the flow fields).

If we denote the strength of the force dipole by $p$, then two kinds of swimmers can be distinguished, depending on the sign of $p$. If $p$ is positive, then the swimmer is called a **pusher**, and if $p$ is negative, then the swimmer is a **puller**. There are a few basic differences between these kinds of swimmers. Pushers generally swim by pushing the fluid behind them away from themselves (with 'in front' and 'behind' defined with respect to the swimming direction). This is usually done through the use of flagella or similar swimming apparatus. A typical example of a pusher is the bacterium *Escherichia coli* (Fig. 0.3 (a)). Pullers in contrast swim by pulling the fluid in front of them towards themselves, again with the help of flagella or similar appendages. A typical puller example is the alga *Chlamydomonas reinhardtii* (Fig. 0.3 (b)).

From our point of view, the most significant difference between pushers and pullers is the different flow fields that they generate in a fluid during their motion. Pushers push out fluid in both directions along the axis of motion, and pull in fluids from both directions perpendicular to this axis. For this reason they are also called 'extensile' swimmers. Pullers exhibit exactly the opposite behaviour of pulling in fluid along the swimming axis and pushing it out perpendicular to this axis, and are also termed 'contractile' swimmers. These flow fields result in two pushers swimming side-by-side attracting each other, as is the case with two pullers swimming one behind the other. Similarly, two pushers swimming one behind the other repel each other, as do two pullers swimming side-by-side. The average directions of the fluid flow around both of these kinds of swimmers, in reference frames moving with the swimmers, are displayed in Fig. 0.2, parts (a) and (c). Note that not all microswimmers can be characterised as pushers or pullers; part (b) of Fig. 0.2 shows such a swimmer along with the the directions of the average local flow fields generated by it.
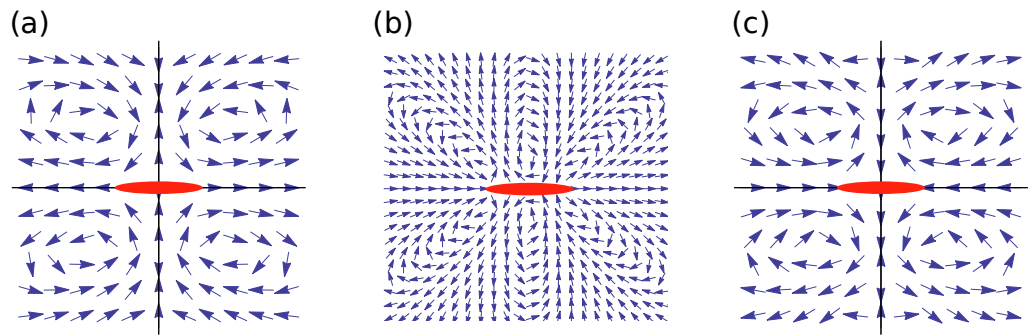
Figure 0.2: The local directions of average flow fields around (a) pushers, (b) neutral swimmers, and (c) pullers, in the frames of reference of the swimmers. The swimmer in each case is denoted by the red figure in the centre, and the swimming is in the horizontal direction, *i.e.* the swimming axis coincides with the long axis of the swimmer.

## 0.2  Different kinds of microswimmers

As seen in section 0.1.3, microswimmers require in general at least two degrees of freedom in configurational space to overcome the limitation imposed on their motion by the scallop theorem. There are many different ways to incorporate these degrees of freedom, and this is evidenced by the dazzling variety of mechanisms that Nature has equipped her tiny inhabitants with to enable them to move. Human ingenuity is a bit more limited, and the designs for artificial microswimmers that have been proposed–whether as theoretical aids intended to deepen our understanding of the world of micro-locomotion or as blueprints for fabrication– typically involve only a bare few degrees of freedom. Here we review some of the most ubiquitous of both biological and human-designed microswimmers.

### 0.2.1  Biological microswimmers

The swimmers in nature come in a great variety of shapes and forms. A majority can nevertheless be classified as swimming due to some appendages to the main swimmer body or due to the deformation of the main swimmer body itself.

The swimming appendages possessed by members of the former class are usually either flagella or cilia. Flagella (Fig. 0.3 (a)-(c)) are relatively long filaments attached to the cell body which are most commonly either rotated as a helix or paddled like oars to move the fluid surrounding the swimmer [Lauga and Powers, 2009]. (Here we make mention of a 'cell' body since the common biological microswimmers like bacteria, *Paramecia*, etc. are typically unicellular organisms.) A swimmer may possess one, two or many flagella, and these may be attached
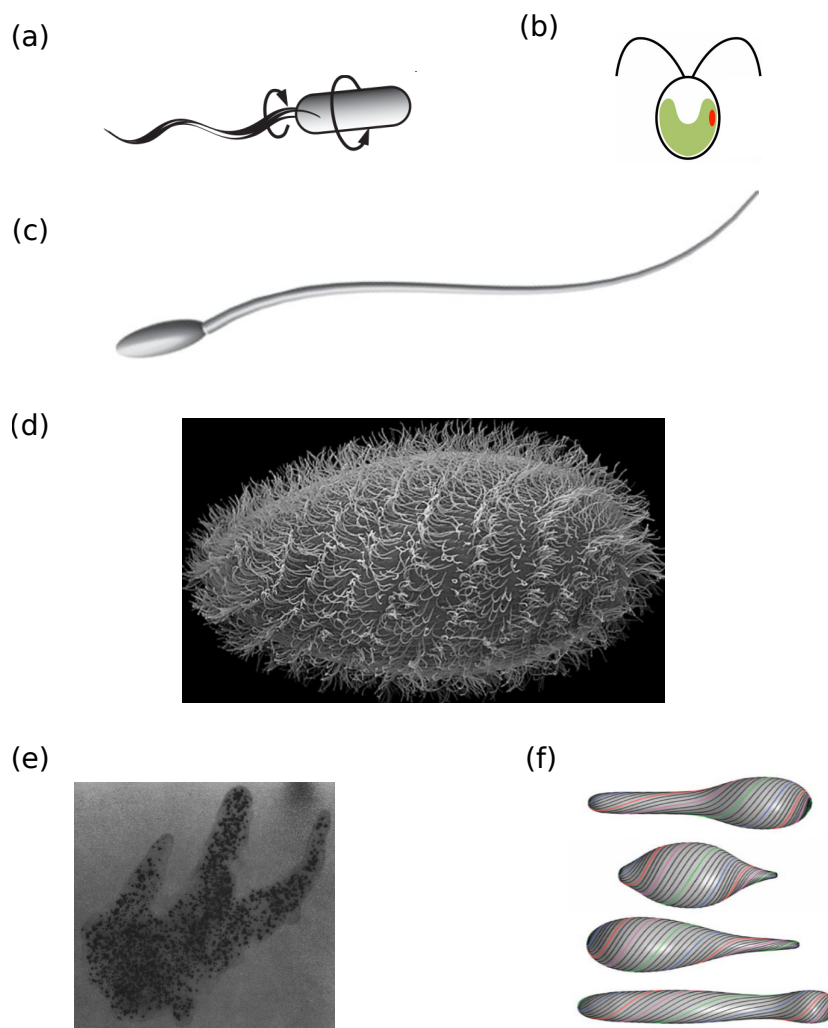
Figure 0.3: Some examples of biological microswimmers. Part (a) shows the bacterium *Escherichia coli* with a flagellar bundle at its back which it uses to push the fluid away from it. Adapted from [DiLuzio *et al.*, 2005]. Part (b) shows the algal cell *Chlamydomonas reinhardtii*, which uses its two flagella to pull the fluid from its front towards its hind side. Adapted from [Ueki *et al.*, 2016]. Part (c) shows a representation of a *Peromyscus* sperm cell, with a single flagellum driving its motion. Adapted from [Fisher *et al.*, 2014]. Part (d) shows a *Paramecium chlorelligerum* cell, with beautiful metachronal waves running across the cilia on its surface. Adapted from [Kreutz *et al.*, 2012]. Part (e) shows the amoeboid organism *Chaos carolinense*. Adapted from [Chapman-Andresen, 1976]. Part (f) shows a schematic representation of the metaboly process in a euglenid. Adapted from [Arroyo *et al.*, 2012].

either at the end(s) of the cell body or all over the surface. The 'run-and-tumble' motion of some common bacteria like *Escherichia coli* and *Salmonella* results from the bundling and unbundling of many flagella on the body [Calladine, 1975, Armitage and Macnab, 1987, Turner *et al.*, 2000, Darnton and Berg, 2007, Vogel and Stark, 2010]. In the 'run' stage of the motion, all the flagella are bundled together and the bundle rotates as a helix counterclockwise, driving the swimmer. In the 'tumble' stage, one flagellum dissociates from the bundle and starts rotating in a clockwise direction, causing the bacterium to realign in a random direction, at which point the run stage commences anew [Macnab, 1977, Berg, 2004, Darnton *et al.*, 2007, Hyon *et al.*, 2012, Vogel and Stark, 2013, Calladine *et al.*, 2013]. For bacteria with a single flagellum, the tumbling motion is accomplished through the use of a buckling instability in the flagellum [Son *et al.*, 2013]. Sperm cells (Fig. 0.3 (c)) in contrast may execute a whip-like beating motion of their flagella, in addition to a helical or planar wave-like motion, to drive the cell [Hatsumi and Wakahama, 1986, Quicke *et al.*, 1992, Bray, 2000, Cosson *et al.*, 2003, Woolley, 2003, Eisenbach and Giojalas, 2006, Friedrich and Jülicher, 2007, Werner and Simmons, 2008, Kaupp *et al.*, 2008, Friedrich *et al.*, 2010, Alvarez *et al.*, 2014]. Swimmers may utilise other kinds of flagellar mechanisms, such as internal flagella [Berg, 1976, Charon *et al.*, 1984, Goldstein and Charon, 1990], flagella with a stop-start mechanism of the motor driving the flagellum [Armitage and Schmitt, 1997], flagella alternately pushing and pulling the cell [Koyasu and Shirakihara, 1984], etc.

Cilia (Fig. 0.3 (d)) are typically arrangements of many filaments which cover the swimmer body and beat together in coordinated ways [Blake and Sleigh, 1974, Brennen and Winet, 1977, Sleigh *et al.*, 1988, Salathe, 2007, Smith *et al.*, 2008]. They differ from flagella mainly in their smaller lengths but larger thicknesses [Elgeti *et al.*, 2015, Purcell, 1977], and in the asymmetry of their beating. While flagellar beats are close to uniform, ciliary beats have a 'power stroke', in which the cilia are extended, and a 'recovery stroke', in which they are folded leading to less hydrodynamic drag [Bray, 2000]. An interesting instance of coordination between cilia is an effect termed as 'metachronal waves', wherein cilia tightly packed together over a surface have waves propagating over the entire arrangement of the cilia, like a 'Mexican wave' in a football stadium, due to a constant phase difference between neighbouring cilia [Tamm and Horridge, 1970, Machemer, 1972, Sleigh *et al.*, 1988, Okamoto and Nakaoka, 1994, Elgeti and Gompper, 2013].

Many micro-organisms use changes of shape of their body itself to help them to propagate. Two common processes for the shape change are amoeboid movement and euglenoid movement or metaboly. Amoeboid movement is exhibited by many organisms which alter their shape by extending bulges of cytoplasm, called pseudopods, from within their plasma membrane and then retracting them at other points on the cell body (Fig. 0.3 (e)). Well-known examples of such organisms are

the multicellular *Dictyostelium discoideum* and *Entamoeba histolytica*, which can reside in the human intestine and cause amoebic dysentery. Metaboly or euglenoid movement is exhibited by some species of euglenids, such as *Eutreptiella gymnastica* Throndsen [1969], and comprises of periodic deformation of the entire cell body with a large amplitude (Fig. 0.3 (f)). Neither the underlying mechanism nor even the purpose of metaboly is well-understood, since the primary mechanism by which euglenids move is through flagellar beating. There is however evidence to suggest that metaboly can be an efficient mode of motility in simple fluids and could become important in granular or complex media [Arroyo *et al.*, 2012].

The above is just a brief description of some common motility strategies of micro-organisms in nature. As may be expected, many other mechanisms exist, such as a differential rotation of the outer body membrane and the inner cytoplasmic membrane of a cell [Berg, 1976, Murphy *et al.*, 2008], using the actin cytoskeleton of a host cell to generate an actin comet which propels the swimmer [Kawska *et al.*, 2012], and swimming by changes in the helicity of the body which cause kinks to propagate down it [Shaevitz *et al.*, 2005].

## 0.2.2   Microswimmer models

In addition to the above-described biological swimmers, there are many artificial models of microswimmers, which either serve as simplistic pictures describing the essential features of locomotion of particular biological swimmers, or as designs for the fabrication of artificial machines either now or in the future, or even as explicatory devices whose main purpose is to shed light on some chosen asppects of microswimming. Here we recount a few of the most important such models.

The first mathematical model of a body which could propel itself in a viscous fluid at negligibly small Reynolds numbers was that of Taylor's swimming sheet, proposed in Taylor [1951] (Fig. 0.4 (a)). In this pioneering study, the two-dimensional sheet was taken to be infinite in extent and to have small amplitude transverse waves on its surface. This is a simplistic model of the beating of sperm flagella. Given the form of the surface oscillations, Taylor showed that the velocity of the sheet could be calculated to desired orders in (amplitude × wavenumber). Interestingly, for a given surface oscillation, the swimming velocity of the sheet does not depend on the viscosity of the fluid. The reason for this becomes clear when one considers the fact that the viscosity affects the load on the sheet and the work done by it in deforming, but this load (or work) is subsumed in the waveform and therefore does not show up in the final result [Lauga and Powers, 2009]. This is in fact a generic feature of locomotion in Newtonian fluids in the Stokes regime: to observe the true dependence of the swimming velocities on the fluid viscosity, it is necessary to give a meaningful energy/force input and let the swimming deformation emerge as a response to this input. This observation will be important for

our own results concerning the effect of viscosity on microswimming presented in section 3.3.

A swimmer model next only in primacy to Taylor's swimming sheet is the one proposed by Purcell in his lecture already alluded to [Purcell, 1977]. It consists of a body with three rigid parts connected together by two hinges (Fig. 0.4 (b)). The individual parts can rotate around these hinges forming angles $\theta_1$ and $\theta_2$ as shown in the figure, and these two angles provide the two requisite independent degrees of freedom that the scallop theorem mandates. When these angles are changed appropriately, such as in the cycle marked by the instantaneous shapes $S_1$ to $S_5$ in Fig. 0.4 (b), the swimmer can propel itself in a fluid, although the direction of motion is not trivial to guess [Becker *et al.*, 2003].

Another swimmer which has come to be very important in the field is the three-sphere swimmer introduced in Najafi and Golestanian [2004]. It consist of three spheres connected together in a line, with the two independent degrees of freedom being the relative distances between two neighbouring spheres, also called the arm lengths (Fig. 0.4 (c)). This swimmer can be seen as following the same design philosophy as Purcell's swimmer in having three body parts changing their relative positions, but it offers the great advantage that the relative displacements of these body parts, as well as the motion of the swimmer, are all along one axis, thus making the analysis of the motion much simpler. For this reason this swimmer has found wide use in analytical [Pooley *et al.*, 2007, Alouges *et al.*, 2008, Golestanian, 2008, Alexander *et al.*, 2008, Zargar *et al.*, 2009, Alouges *et al.*, 2009, Najafi and Golestanian, 2010], numerical [Earl *et al.*, 2007, Pooley and Yeomans, 2008] and experimental [Leoni *et al.*, 2009] research. In our work we employ a bead-spring model which is based on the three-sphere swimmer but incorporates some essential differences which are necessary for our investigations. We explain both the three sphere swimmer and our bead-spring model in detail in chapter 1.

A swimmer which dispenses with one of the spheres in the three sphere model is the pushmepullyou [Avron *et al.*, 2005]. It has just two spheres connected by an arm of variable length, and the second degree of freedom is attained by making the volumes of the spheres vary in time subject to a total volume preservation constraint (Fig. 0.4 (d)). This swimmer can in fact be seen as being equivalent to the three sphere model, with the near and far configurations of two neighbouring spheres being replaced by the small and large configurations of a single sphere, respectively. The equivalence of the two situations lies in the fact that both of these deformations have the effect of changing the hydrodynamic radius of an actual sphere or an effective sphere composed of two neighbouring spheres. For comparable dimensions and driving, the pushmepullyou swimmer has been found to be more efficient than the three sphere model if large amplitudes of the swimming strokes are allowed, and its efficiency is higher than that of biological flagellar

(a)



(b)

(c)

(d)

(e)
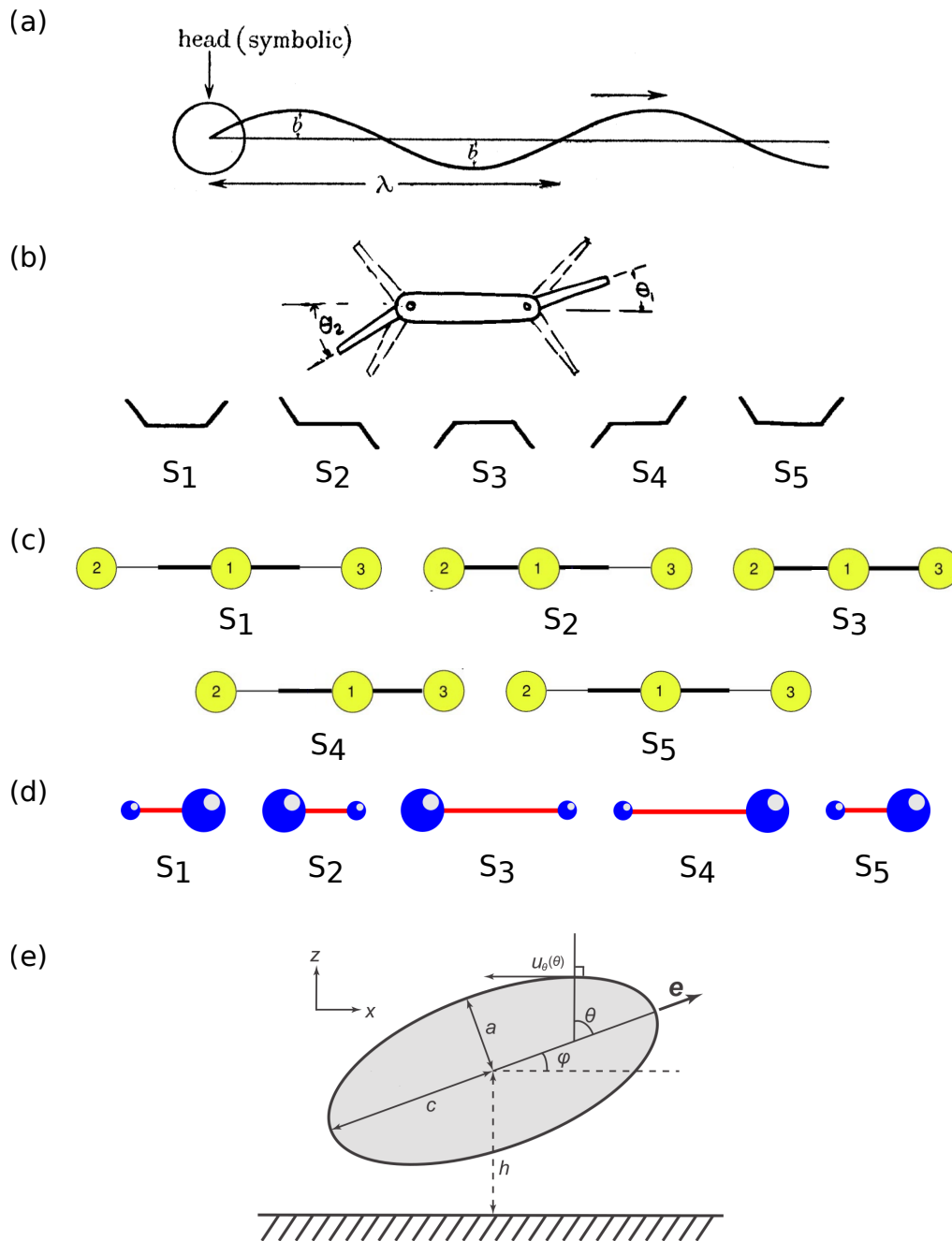
Figure 0.4: Some examples of microswimmer models. Part (a) shows Taylor's swimming sheet, modelling the beating motion of a sperm flagellum. Taken from [Taylor, 1951]. Part (b) shows Purcell's swimmer, with a double switchblade-like structure (top), and the shapes comprising one swimming cycle (bottom). Adapted from [Purcell, 1977]. Part (c) shows the different configurations of the three-sphere swimmer comprising one swimming cycle. Adapted from [Najafi and Golestanian, 2004]. Part (d) shows the pushmepullyou swimmer, with the different configurations it adopts in one swimming cycle. Adapted from [Avron et al., 2005]. Part (e) shows the schematic representation of a squirmer. Taken from [Ishimoto and Gaffney, 2013].

swimmers [Avron *et al.*, 2005].

Another popular swimmer model is that of a squirmer, which consists of a sphere with an effective slip velocity prescribed for the average fluid flow close to the sphere surface (Fig. 0.4 (e)). It was introduced by Lighthill [Lighthill, 1952], and later extended by Blake [Blake, 1971], in order to describe the swimming speeds of and the flows surrounding micro-organisms like *Volvox* and *Paramecium*, whose surfaces are covered with thousands of beating cilia which impart a net non-zero flow to the fluid in the vicinity of the organisms. The squirmer is thus a representative of a common approach in the field, wherein instead of resolving fully the components and the forces of a swimmer an effective force field, which controls the main features of the motion, is assumed to act on the swimmer [Drescher *et al.*, 2010, Friedrich and Jülicher, 2012]. For a squirmer, with a particular form of the velocity field on its surface squirmer assumed, it is found that the swimming velocity is independent of the fluid viscosity [Lighthill, 1952], which harks back to our earlier discussion of the effects of the viscosity being invisible when the stroke is prescribed.

There are many other swimmer models which have been proposed, such as a surface treadmiller [Leshansky *et al.*, 2007], a bilayer vesicle jellyfish [Evans *et al.*, 2010], rotating two-sphere swimmers [Ogrin *et al.*, 2008], and many-scallop swimmers [Lauga and Bartolo, 2008], among others.

### 0.2.3  Microswimmers in experiments

There are a number of experimental models which seek to recreate or build upon biological or theoretical swimming mechanisms such as the ones described above. An important example of such a model swimmer, the first of its kind at the microscale, was constructed by Dreyfus *et al.* in 2005, and consisted of a chain of paramagnetic filaments attached to a main body which was made of a red blood cell [Dreyfus *et al.*, 2005]. Actuation by an external alternating magnetic field caused the chain to wiggle, in a fashion somewhat reminiscent of a sperm cell, and the whole assembly to swim in the direction of the chain (unlike a sperm cell). Another swimmer which copies the wiggling motion of sperm was presented in Williams *et al.* [2014]. It is made up of a polydimethylsiloxane filament which has a small head and a long tail with heart muscle cells grown on it. Contraction of the heart muscle cells causes the filament to deform leading to motion of the assembly. More examples of biology-inspired swimmers are those with artificial cilia [Vilfan *et al.*, 2010, Branscomb and Alexeev, 2010, Masoud and Alexeev, 2011] such as those using microtubule bundles [Sanchez *et al.*, 2011], magnetic bead chains [Kim and Netz, 2006] and micro-pillars mounted on piston-like actuators [Keissner and Brücker, 2012], or rotating discs and spheres [Grzybowsk *et al.*, 2000, Bleil *et al.*, 2006, Tierno *et al.*, 2008b], which mimic the rotating

motion of the green alga *Volvox*.

## 0.3   Structure of the thesis

This thesis is structured as follows. Following this chapter, we introduce in chapter 1 the swimmer model that we shall use throughout this work, the **bead-spring swimmer**, and present the calculation of the velocity of this swimmer under various conditions, such as with rigid beads, with deformable beads, and to different orders in certain important parameters. This chapter contains the bulk of our calculations presented in this thesis–with the notable exception of the calculation of the velocity of a swimmer with inertia which we discuss in chapter 6–and we shall make use of the results found here throughout the rest of the work to discuss various features of microswimming. In chapter 2 we explain the lattice Boltzmann method (LBM) of simulations in brief, and give details of the two LBM simulation systems used by us, the waLBerla-*pe* system and LB3D. In chapter 3 we first verify the basic calculations presented in chapter 1 by comparing their predictions to results from simulations, and then show that our theory can help explain a puzzling phenomenon in microswimming, which is that some microswimmers have been observed to swim faster when the viscosity of the ambient fluid is increased, in apparent contradiction of theoretical models based on simple Newtonian fluids. In chapter 4 we study the question of whether the swimming velocity can be enhanced if the body of the swimmer, not counting the swimming appendages like flagella, etc., is able to deform in response to the fluid flow around it. In chapter 5 we determine the optimal shapes for the beads in our swimmer when they are restricted to be prolate or oblate ellipsoids of a fixed volume or surface area. In doing this we identify two regimes of motion wherein the swimming is dominated either by a reduction of the resistive drag faced by the swimmer, or by an increase in the hydrodynamic interaction amongst various motile parts of the swimmer. In chapter 6 we extend our study to include inertial effects in the swimmer's motion, which are absent in purely Stokesian flow. For this we first identify the limits of the Stokes regime for our swimmer by likening its relaxation in a fluid to that of an underdamped harmonic oscillator, and then calculate the velocity of the swimmer in the inertial case explicitly by modifying the equations of motion appropriately. We show that our calculation provides results which compare favourably to simulations when the driving forces (and thereby the swimming strokes, the swimming velocities and the Reynolds numbers of motion) are too large for the Stokes approximation to be valid. We finish in chapter 7 by summing up our work, and describing a few worthwhile directions in which it may be extended.

<div style="text-align: right;">*1*</div>

# The bead-spring model of a microswimmer

The basic microswimmer model that will be employed by us throughout this thesis will be one composed of three bodies connected in series through springs and driven by known forces (Fig. 1.1). The three bodies will have the possibility of being spherical or non-spherical in shape, and of rigid or deformable material.
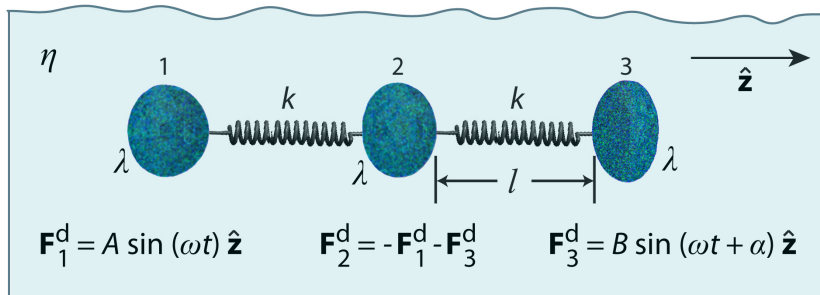
Figure 1.1: Basic bead-spring swimmer model composed of bodies, which may be non-spherical and of non-constant shape, connected by springs in a line. In the model the forces driving the motion are specified. Figure taken from publication **P3** [Pande *et al.*, 2016a].

We shall refer to our model as the bead-spring model. The design of our model is inspired from that of the three-sphere swimmer introduced in Najafi and Golestanian [2004]. While our swimmer resembles the Najafi-Golestanian one (henceforth in the thesis, and popularly in the literature, referred to as the 'Golestanian model') in geometry to the extent that both are composed of three objects connected in a series arrangement which imparts to them the freedom to travel along a line, our design is different in a few essential ways. The most important difference is that in our model we resolve the forces upon the swimmer fully

and let the swimming stroke emerge as a response to the forces, whereas in the Golestanian model the swimming stroke is assumed. Other differences include the inclusion of springs, the use of non-spherical beads, the use of deformable beads, and the consideration of the effects arising from the swimmer's inertia. We shall show how each feature of our model is crucial in obtaining some result about microswimming that we present in our thesis. To allow a full appreciation of these points, we first present a short overview of the Golestanian model.

## 1.1 The Golestanian three-sphere swimmer model

The Golestanian swimmer has been a popular one in the microswimming community owing to its simplicity, and has been employed in a number of analytical and simulation-based studies concerning microswimming [Pooley *et al.*, 2007, Alouges *et al.*, 2008, Golestanian, 2008, Alexander *et al.*, 2008, Zargar *et al.*, 2009, Alouges *et al.*, 2009, Najafi and Golestanian, 2010, Earl *et al.*, 2007, Pooley and Yeomans, 2008]. Experimental realisations of the model are rarer but exist [Leoni *et al.*, 2009].

The Golestanian model is made up of three spheres in a series arrangement (Fig. 1.2). The two required degrees of freedom in the swimmer are the lengths of the two arms–where an arm is defined as one of the two line segments whose end-points are the centres of two neighbouring spheres–which can change independently of each other. The motion is held to occur in purely Stokesian flow. An important feature of the model is that the swimming stroke, *i.e.* the dependence of the length of the arms on time, is assumed to be known *a priori*.

The main idea underlying the model is that if the swimming stroke breaks time and space symmetries, the swimmer executes persistent motion along the line on which the spheres lie. The breaking of time and space symmetries is important to ensure non-reciprocality in the stroke and thereby satisfy the demands of the scallop theorem (see section 0.1.3 in the Introduction). Fig. 1.2 shows one full cycle of the three-sphere swimmer composed of four steps, at the end of which the swimmer has travelled a distance $\Delta$ along its axis. Note that if the steps (b) and (c) of the cycle were interchanged, then the swimmer would not move, in accordance with the scallop theorem.

The advantage in specifying the stroke is that the equations of motion adopt an algebraic form which can be easily solved. As a particular example, assume that the swimming stroke is sinusoidal so that the two armlengths $L_1(t)$ and $L_2(t)$ are given by

$$L_1(t) = l + d_1 \cos(\omega t + \delta_1),$$
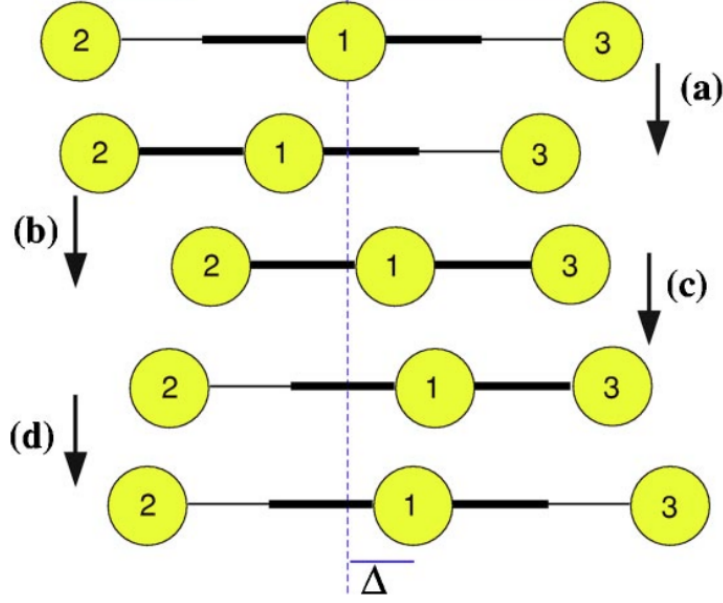$$L_2(t) = l + d_2 \cos(\omega t + \delta_2), \tag{1.1}$$

Figure 1.2: The Golestanian three-sphere microswimmer model, showing the swimming cycle composed of four steps (a), (b), (c) and (d). The total distance covered in a cycle is $\Delta$. Figure taken from [Golestanian and Ajdari, 2008].

where $l$ denotes the mean length of both the arms, $\omega$ denotes the strokes frequency, and $d_i$ and $\delta_i$ denote respectively the stroke amplitude and phase shift of the $i^{\text{th}}$ arm. To allow the model to be solved, the far-field approximation must be made, in which the distances between the spheres dominate the other length scales, *i.e.* $r_i \ll l_j$ and $d_i \ll l_j$, where $r_i$ are the radii of the spheres. Under these conditions, the velocity of the swimmer comes out to be [Golestanian and Ajdari, 2008]

$$\mathbf{v}_{\text{stroke}} = G d_1 d_2 \omega \sin\left(\delta_1 - \delta_2\right) \hat{\mathbf{z}}, \tag{1.2}$$

where the swimmer is taken to be aligned along the $z$-axis. Here $\mathbf{v}_{\text{stroke}}$ is the swimming velocity (with the subscript referring to the stroke-dependence of its calculation), and $G$ is a geometrical constant which for equal sphere radii $r$ and equal mean arm-lengths $l$ is given by $G = 7r/\left(24l^2\right)$.

## 1.2 Our microswimmer model: the bead-spring swimmer

Like the Golestanian swimmer, our swimmer is composed of three objects (which we call 'beads') arranged in series (Fig. 1.1). It however differs from the Golesta-

nian model in the following important respects:

1. We specify the forces driving the motion instead of the swimming stroke, which in our description emerges in response to the forces.

2. The three beads in the swimmer can be non-spherical.

3. The shapes of the three beads can vary in time during a cycle.

4. The motion is not always strictly restricted to the Stokesian realm. In the last part of this thesis we shall consider the effects of inertia on swimming, which are completely absent in Stokesian motion.

The main effect of introducing the above changes in the model *vis-á-vis* the Golestanian swimmer is that it allows us much greater freedom in exploring the various influences of different kinds of forces on the swimming motion. The study of these force influences is worthwhile as it imparts insight into many interesting and important aspects of microswimming, as we shall show in this thesis. Our force-based approach is also more basic in the sense that a swimming stroke in practice results from the responsive realignment of the parts of a swimmer's body to the different forces acting on them. The price that this primacy of approach extracts is a complication in the analysis, with the equations of motion no longer solvable algebraically.

In this chapter, we explain our methods of solving our model for the velocity of the swimmer with all of the above modifications to the Golestanian model, except for the calculation of the motion in a non-Stokesian realm, which is deferred to Chapter 6.

### 1.2.1   Velocity calculation for a swimmer with rigid beads [*]

We first assume that the three beads are rigid and possibly non-spherical, and that the fluid flow is completely Stokesian. In subsequent sections, we shall consider the cases of deformable beads and non-Stokesian flow. In our swimmer the beads are connected by harmonic springs (Fig. 1.1), and the forces driving the motion are sinusoidal, of the form

$$
\begin{aligned}
\mathbf{F}_1^{\mathrm{d}}(t) &= A \sin\left(\omega t\right) \hat{\mathbf{z}}, \\
\mathbf{F}_2^{\mathrm{d}}(t) &= -\mathbf{F}_1^{\mathrm{d}}(t) - \mathbf{F}_3^{\mathrm{d}}(t), \text{ and} \\
\mathbf{F}_3^{\mathrm{d}}(t) &= B \sin\left(\omega t + \alpha\right) \hat{\mathbf{z}}, \text{ with } \alpha \in \left[-\pi, \pi\right].
\end{aligned}
\tag{1.3}
$$

[*]This section has been adapted from publication **P2** [Pande *et al.*, 2016b], with changes for consistency.

Here *A* and *B* are non-negative amplitudes of the time-dependent driving forces $\mathbf{F}_1^d(t)$ and $\mathbf{F}_3^d(t)$ applied along the $\hat{\mathbf{z}}$-direction to the outer beads at the frequency $\omega$ and with the phase difference $\alpha$. The force $\mathbf{F}_2^d(t)$ on the middle bead is set by the condition for autonomous propulsion, which requires the net driving force on the device to vanish at all times. For simplicity, we assume the two springs to be identical to each other and the three beads to be identical in shape too. The theory can be very easily extended to dissimilar springs and beads, but the end result obtained in the case of identical springs and identical beads is the most concise and convenient to express (here Eq. (1.11)). Indeed, later when we evaluate the swimming velocity of a swimmer with deformable beads (section 1.2.3), we will necessarily have to preserve the dissimilarity of shape in the three beads, since the shape deformation of the three beads over a swimming cycle will in general be different, even if the initial shapes of the three beads are identical.

The springs are identical, then, with a stiffness constant *k* and a rest length *l* which is much larger than the bead dimensions as well as the oscillation amplitudes of the arm lengths (this being again the far-field approximation which was adopted in the Golestanian model). We find it convenient to define a 'reduced friction coefficient' $\lambda$ of the beads as

$$\lambda = \gamma / (6\pi\eta), \tag{1.4}$$

where $\gamma$ is the Stokes drag coefficient of each bead and $\eta$ is the dynamic viscosity of the fluid. For a sphere, the reduced parameter $\lambda$ is nothing but its radius. Due to the far-field aproximation made, by which $\lambda \ll l$, the precise shape of each bead is not directly visible to the other two beads which see its influence only through the far flow fields generated by its motion. In this scenario, the shape of a bead enters the picture only through its modulation of the drag force faced by the bead itself– which affects the motion of the fluid around it and thereby that of the other two beads. This means that for non-spherical beads, the reduced friction coefficient $\lambda$ plays the same role as the radius of a spherial bead in the model [Pande and Smith, 2015].

The fluid is taken to be Newtonian and its flow is governed by the Stokes and incompressibility equations,

$$\eta\nabla^2\mathbf{u}(\mathbf{r},t) - \nabla p(\mathbf{r},t) + \mathbf{f}(\mathbf{r},t) = 0 \text{ and} \tag{1.5}$$

$$\nabla \cdot \mathbf{u} = 0. \tag{1.6}$$

Here $\eta$ is the dynamic viscosity of the fluid, related to the kinematic viscosity $\nu$ as $\eta = \nu\rho$, where $\rho$ is the fluid density. The fluid moves with a velocity $\mathbf{u}(\mathbf{r},t)$ under a pressure $p(\mathbf{r},t)$ at the point $\mathbf{r}$ at time *t*. The force density $\mathbf{f}(\mathbf{r},t)$ acting on the

fluid is given by

$$\mathbf{f}\left(\mathbf{r}, t\right) = \sum_{i=1}^{3} \left(\mathbf{F}_i^{\mathrm{d}}(t) + \mathbf{F}_i^{\mathrm{s}}(t)\right) \delta\left(\mathbf{r} - \mathbf{R}_i(t)\right), \qquad (1.7)$$

where the index $i = 1, 2, 3$ denotes the $i$-th bead placed at the position $\mathbf{R}_i(t)$ subject to a driving force $\mathbf{F}_i^{\mathrm{d}}(t)$ and a net spring force $\mathbf{F}_i^{\mathrm{s}}(t)$. The latter can be written as

$$\mathbf{F}_i^{\mathrm{s}}(t) = \sum_{j \neq i}^{3} \mathbf{G}\left(\mathbf{R}_i(t) - \mathbf{R}_j(t)\right), \text{ with}$$

$$\mathbf{G}\left(\mathbf{R}_i(t) - \mathbf{R}_j(t)\right) = -k\left(\frac{\mathbf{R}_i(t) - \mathbf{R}_j(t)}{|\mathbf{R}_i(t) - \mathbf{R}_j(t)|}\right)\left(|\mathbf{R}_i(t) - \mathbf{R}_j(t)| - l\right) \qquad (1.8)$$

if $i$ and $j$ denote neighboring beads, and $\mathbf{G}\left(\mathbf{R}_i(t) - \mathbf{R}_j(t)\right) = \mathbf{0}$ otherwise. Assuming no slip at the fluid-bead interfaces, the instantaneous velocity $\mathbf{v}_i(t)$ of each bead [Doi and Edwards, 1988] is given by

$$\mathbf{v}_i(t) = \dot{\mathbf{R}}_i(t) = \left(\mathbf{F}_i^{\mathrm{d}}(t) + \mathbf{F}_i^{\mathrm{s}}(t)\right) / \left(6\pi\eta\lambda\right)$$
$$+ \sum_{j \neq i}^{3} \mathbf{T}\left(\mathbf{R}_i(t) - \mathbf{R}_j(t)\right) \cdot \left(\mathbf{F}_j^{\mathrm{d}}(t) + \mathbf{F}_j^{\mathrm{s}}(t)\right), \qquad (1.9)$$

where $\mathbf{T}\left(\mathbf{r}\right)$ is the Oseen tensor [Happel and Brenner, 1965, Oseen, 1927]. Here in $\dot{\mathbf{R}}_i(t)$ and throughout the thesis, a (double) dot over a variable denotes its (double) derivative with respect to time.

As borne out by simulations, the bead positions in the steady state take the form

$$\mathbf{R}_i(t) = \mathbf{S}_{i0} + \boldsymbol{\xi}_i(t) + \mathbf{v}_{\mathrm{force}}\, t, \qquad (1.10)$$

where $\boldsymbol{\xi}_i(t)$ denotes small sinusoidal oscillations, which will be taken as perturbation variables around the equilibrium configuration $\mathbf{S}_{i0}$ of the swimmer. The swimmer moves with a cycle-averaged velocity $\mathbf{v}_{\mathrm{force}}$, where the subscript refers to the fact that the treatment is force-centric as opposed to being stroke-centric like $\mathbf{v}_{\mathrm{stroke}}$ in section 1.1. Under this assumption, we can write the mean swimming velocity $\mathbf{v}_{\mathrm{force}}$ as the average velocity of the centre of reaction $\mathbf{C}(t)$ of the swimmer [Happel and Brenner, 1965] over one swimming cycle $\tau$, given by

$$\mathbf{v}_{\mathrm{force}} = \frac{1}{\tau} \int_0^\tau \mathrm{d}t\, \dot{\mathbf{C}}(t) = \frac{1}{\tau} \int_0^\tau \mathrm{d}t \sum_{i=1}^{3} \lambda_i \dot{\mathbf{R}}_i(t) \Big/ \sum_{i=1}^{3} \lambda_i. \qquad (1.11)$$

Following the method in Felderhof [2006], we expand the functions of the relative positions $(\mathbf{R}_i(t) - \mathbf{R}_j(t))$ in Eq. (1.9) in terms of series of the variables $(\boldsymbol{\xi}_i(t) - \boldsymbol{\xi}_j(t))$ centred around the equilibrium configuration, which can be taken to be the configuration at time $t = 0$. The different variables expanded to the first order in $(\boldsymbol{\xi}_i(t) - \boldsymbol{\xi}_j(t))$ are

$$\mathbf{G}\left(\mathbf{R}_i(t) - \mathbf{R}_j(t)\right) =$$
$$\mathbf{G}\left(\mathbf{R}_i(0) - \mathbf{R}_j(0)\right) + \left.\frac{\partial \mathbf{G}\left(\mathbf{R}_i(t) - \mathbf{R}_j(t)\right)}{\partial \mathbf{R}_i(t)}\right|_{t=0} \cdot \left(\boldsymbol{\xi}_i(t) - \boldsymbol{\xi}_j(t)\right)$$
$$= \mathbf{H}_{ij} \cdot \left(\boldsymbol{\xi}_i(t) - \boldsymbol{\xi}_j(t)\right), \text{ with } \mathbf{H}_{ij} = \left.\frac{\partial \mathbf{G}\left(\mathbf{R}_i(t) - \mathbf{R}_j(t)\right)}{\partial \mathbf{R}_i(t)}\right|_{t=0}, \quad (1.12)$$

and

$$\mathbf{T}\left(\mathbf{R}_i(t) - \mathbf{R}_j(t)\right) =$$
$$\mathbf{T}\left(\mathbf{R}_i(0) - \mathbf{R}_j(0)\right) + \left.\frac{\partial \mathbf{T}\left(\mathbf{R}_i(t) - \mathbf{R}_j(t)\right)}{\partial \mathbf{R}_i(t)}\right|_{t=0} \cdot \left(\boldsymbol{\xi}_i(t) - \boldsymbol{\xi}_j(t)\right)$$
$$= \mathbf{T}_{ij} + \mathbf{V}_{ij} \cdot \left(\boldsymbol{\xi}_i(t) - \boldsymbol{\xi}_j(t)\right),$$
$$\text{with } \mathbf{T}_{ij} = \mathbf{T}\left(\mathbf{R}_i(0) - \mathbf{R}_j(0)\right) \text{ and } \mathbf{V}_{ij} = \left.\frac{\partial \mathbf{G}\left(\mathbf{R}_i(t) - \mathbf{R}_j(t)\right)}{\partial \mathbf{R}_i(t)}\right|_{t=0}. \quad (1.13)$$

Combining Eqs. (1.12)-(1.13) and using the fact that $\mathbf{F}_i^d(t)$ and $\mathbf{F}_i^s(t)$, the driving and the spring forces, sum to zero over the three bodies at each instant, we expand all terms in Eq. (1.11) to the lowest surviving order in $\boldsymbol{\xi}_i(t)$. Since the displacements $\boldsymbol{\xi}_i(t)$ directly arise from the driving forces $\mathbf{F}_j^d(t)$, this also means the lowest surviving order in $\mathbf{F}_j^d(t)$ [Felderhof, 2006]. Moreover, since both the displacements and the driving forces are sinusoidal, it turns out that all terms in Eq. (1.11) of the zeroth or first order in $\boldsymbol{\xi}_i(t)$ or $\mathbf{F}_j^d(t)$ average to zero over a cycle. We calculate to the second order in $\boldsymbol{\xi}_i/l$, therefore, and the final velocity for the swimmer to the lowest surviving order in $\lambda/l$ comes out to be

$$\mathbf{v}_{\text{force}} = \frac{7\lambda\omega\left[AB\left(k^2 + 12\pi^2\eta^2\omega^2\lambda^2\right)\sin\alpha + 2\left(A^2 - B^2\right)\pi\eta\omega k\lambda\right]}{24l^2\left(k^2 + 4\pi^2\eta^2\omega^2\lambda^2\right)\left(k^2 + 36\pi^2\eta^2\omega^2\lambda^2\right)}\hat{\mathbf{z}}. \quad (1.14)$$

We have thus found the velocity of our swimmer in the rigid-bead case.

**Comparison with the stroke-based formulation** [†]

With the method described above, it is possible to find the swimming stroke that is assumed by the swimmer and then to use Eq. (1.2) to find the swimming velocity as a function of this stroke. In this way the two approaches of finding the swimming velocity–*i.e.* assuming known driving forces and assuming known strokes–may be reconciled. The stroke parameters are found to be

$$d_1 = \sqrt{\frac{A^2 k^2 + 4\pi^2 \eta^2 \omega^2 \lambda^2 \left(4A^2 + B^2 + 4AB \cos \alpha\right) - 4AB\pi\eta\omega k\lambda \sin \alpha}{k^4 + 40\pi^2 \eta^2 \omega^2 k^2 \lambda^2 + 144\pi^4 \eta^4 \omega^4 \lambda^4}}, \quad (1.15)$$

$$d_2 = \sqrt{\frac{B^2 k^2 + 4\pi^2 \eta^2 \omega^2 \lambda^2 \left(A^2 + 4B^2 + 4AB \cos \alpha\right) + 4AB\pi\eta\omega k\lambda \sin \alpha}{k^4 + 40\pi^2 \eta^2 \omega^2 k^2 \lambda^2 + 144\pi^4 \eta^4 \omega^4 \lambda^4}}. \quad (1.16)$$

Defining $\beta$ as the stroke phase shift $\beta = \delta_1 - \delta_2$, its sinusoidal function is given by

$$\sin \beta = \frac{N}{D}, \text{ where} \quad (1.17)$$

$$N = 2\left(A^2 - B^2\right)\pi\eta\omega k\lambda + AB\left(k^2 + 12\pi^2 \eta^2 \omega^2 \lambda^2\right)\sin \alpha, \text{ and} \quad (1.18)$$

$$
\begin{aligned}
D = \Bigg\{ & A^2 B^2 k^4 + 4\pi\eta\omega\lambda \Bigg[ \pi\eta\omega k^2 \lambda \left(A^4 + 6A^2 B^2 + B^4\right) \\
& + 4\pi^3 \eta^3 \omega^3 \lambda^3 \left(4A^4 + 25A^2 B^2 + 4B^4\right) \\
& + 4AB\pi\eta\omega\lambda \cos \alpha \left(A^2 + B^2\right)\left(k^2 + 20\pi^2 \eta^2 \omega^2 \lambda^2\right) \\
& + 2A^2 B^2 \pi\eta\omega\lambda \left(k^2 + 16\pi^2 \eta^2 \omega^2 \lambda^2\right)\cos\left(2\alpha\right) \\
& + ABk \sin \alpha \left(A^2 - B^2\right)\left(k^2 + 12\pi^2 \eta^2 \omega^2 \lambda^2\right) \Bigg] \Bigg\}^{1/2}. \quad (1.19)
\end{aligned}
$$

We may now recast the stroke-based velocity form of Eq. (1.2) into the force-based one of Eq. (1.14). A comparison between the two, deferred to Fig. 1.3, shows that the two velocities agree in the limit $\lambda \ll l$.

---

[†]This section has been adapted from publication **P5** [Pickl *et al.*, 2016], with changes for consistency.

## 1.2.2  Calculation of swimming velocity to higher orders in $\lambda/l$

‡

It is possible to find the velocity of the swimmer to higher orders in $\lambda/l$. While this leads to nominally greater accuracy in the result, it should be remembered that the $\lambda \ll l$ condition is nevertheless important if we are to include non-spherical beads in the model by using their $\lambda$ as their effective radius. It also turns out, as we shall show by comparing the velocity result for different orders in $\lambda/l$, that the increase in the accuracy on including higher order terms is insignificant, about 5% or smaller if $\lambda/l < 1/5$.

To do the calculation in section 1.2.1 to higher orders in $\lambda/l$, we replace the Oseen tensor by the Rotne-Prager one [Rotne and Prager, 1969], which gives the hydrodynamic interaction terms to one order higher than the Oseen approximation. This involves the use of the method of reflections [Aguirre and Murphy, 1973]. Section 5.10 in Dhont [1996] provides the Rotne-Prager matrix for a suspension of spheres of equal radii. Following a similar procedure, we here present for the interested reader the derivation of the matrix for beads with possibly unequal reduced friction coefficients $\lambda_i$.

We start with the flow field induced in an initially motionless fluid by a bead of radius $\lambda_j$ and velocity $\mathbf{v}_j$ positioned instantaneously at the origin of the coordinate system. This flow field $\mathbf{u}(\mathbf{r})$ at the point $\mathbf{r}$ in the fluid is given by

$$\mathbf{u}(\mathbf{r}) = \left\{ \frac{3}{4} \frac{\lambda_j}{|\mathbf{r}|} \left( \mathbb{I} + \frac{\mathbf{r}\mathbf{r}}{|\mathbf{r}|^2} \right) + \frac{1}{4} \left( \frac{\lambda_j}{|\mathbf{r}|} \right)^3 \left( \mathbb{I} - 3\frac{\mathbf{r}\mathbf{r}}{|\mathbf{r}|^2} \right) \right\} \cdot \mathbf{v_j}. \tag{1.20}$$

For our assembly of beads, the flow field induced by each bead then affects the motion of the other beads. The change in the other beads' velocities is given by Faxén's theorem for translational motion [Faxén, 1922], which states that the velocity $\mathbf{v}_i$ acquired by a sphere of radius $a_i$ immersed at the position $\mathbf{r}_i$ in a fluid with a flow velocity field $\mathbf{u}(\mathbf{r})$ is given by

$$\mathbf{v}_i = \frac{-1}{6\pi\eta a_i}\mathbf{F}_i^{\mathrm{h}} + \mathbf{u}(\mathbf{r}_i) + \frac{1}{6}a_i^2\nabla_i^2\mathbf{u}(\mathbf{r}_i), \tag{1.21}$$

where $\mathbf{F}_i^{\mathrm{h}}$ is the hydrodynamic drag force on the sphere in question.

In our case, clearly, the velocity $\mathbf{v}_i$ of the $i^{\mathrm{th}}$ bead is affected by the fluid flow $\mathbf{u}(\mathbf{r})$ induced by the $j^{\mathrm{th}}$ bead swimming with the velocity $\mathbf{v}_j$ at the instantaneous position $\mathbf{r}_j$ in the fluid. Since the velocity of the $j^{\mathrm{th}}$ bead in the absence of any

---

‡This section has been adapted from publication **P5** [Pickl *et al.*, 2016], with changes for consistency.

other bead is given by the Stokes drag law

$$\mathbf{v}_j = \frac{-1}{6\pi\eta\lambda_j}\mathbf{F}^{\mathrm{h}}_j, \tag{1.22}$$

therefore, combining Eqs. (1.20)-(1.22), we find the velocity of the $i^{\mathrm{th}}$ bead in terms of the drag forces on the $i^{\mathrm{th}}$ and the $j^{\mathrm{th}}$ beads as

$$\begin{aligned}
\mathbf{v}_i =& \frac{-1}{6\pi\eta\lambda_i}\mathbf{F}^h_i \\
&+ \left(\frac{-1}{6\pi\eta\lambda_j}\right)\left(1 + \frac{1}{6}\lambda_i^2\nabla_i^2\right)\left\{\left[\frac{3}{4}\left(\frac{\lambda_j}{r_{ij}}\right)(\mathbb{I} + \hat{\mathbf{r}}_{ij}\hat{\mathbf{r}}_{ij}) + \frac{1}{4}\left(\frac{\lambda_j}{r_{ij}}\right)^3(\mathbb{I} - 3\hat{\mathbf{r}}_{ij}\hat{\mathbf{r}}_{ij})\right]\cdot\mathbf{F}^h_j\right\},
\end{aligned} \tag{1.23}$$

where $\hat{\mathbf{r}}_{ij} \equiv \dfrac{(\mathbf{r}_i - \mathbf{r}_j)\,(\mathbf{r}_i - \mathbf{r}_j)}{|\mathbf{r}_i - \mathbf{r}_j|^2}$ and $r_{ij} \equiv |\mathbf{r}_i - \mathbf{r}_j|$.

We will find the Laplacian in eq. (1.23) explicitly, by making use of spherical polar coordinates, in which

$$\nabla^2 \equiv \frac{1}{r^2}\frac{\partial}{\partial r}\left(r^2\frac{\partial}{\partial r}\right) + \frac{1}{r^2\sin\theta}\frac{\partial}{\partial\theta}\left(\sin\theta\frac{\partial}{\partial\theta}\right) + \frac{1}{r^2\sin^2\theta}\left(\frac{\partial^2}{\partial\phi^2}\right). \tag{1.24}$$

Therefore, we have immediately $\nabla^2\left(\dfrac{1}{r^3}\right) = 6r^{-5}$ and $\nabla^2\left(\dfrac{1}{r}\right) = 0$, for $r \neq 0$.

To find $\mathbf{v}_i$, we will first show that $\nabla_i^2\left\{\dfrac{1}{r_{ij}}[\mathbb{I} + \hat{\mathbf{r}}_{ij}\hat{\mathbf{r}}_{ij}]\right\} = 2\left(\dfrac{1}{r_{ij}}\right)^3[\mathbb{I} - 3\hat{\mathbf{r}}_{ij}\hat{\mathbf{r}}_{ij}]$ and $\nabla_i^2\left\{\left(\dfrac{1}{r_{ij}}\right)^3[\mathbb{I} - 3\hat{\mathbf{r}}_{ij}\hat{\mathbf{r}}_{ij}]\right\} = 0$. For this, assume that $\mathbf{r}_j = \mathbf{0}$, *i.e.*, we are shifting the coordinate system in order to let $\mathbf{r}_j$ coincide with the origin. Then, we need to find $\nabla^2\left\{\dfrac{1}{r}[\mathbb{I} + \hat{\mathbf{r}}\hat{\mathbf{r}}]\right\}$ and $\nabla^2\left\{\left(\dfrac{1}{r}\right)^3[\mathbb{I} - 3\hat{\mathbf{r}}\hat{\mathbf{r}}]\right\}$. Explicitly, we have

$$\begin{aligned}
\frac{\mathbb{I} + \hat{\mathbf{r}}\hat{\mathbf{r}}}{r} &= \frac{1}{r}\begin{pmatrix} 1 + \sin^2\theta\cos^2\phi & \sin^2\theta\cos\phi\sin\phi & \sin\theta\cos\theta\cos\phi \\ \sin^2\theta\cos\phi\sin\phi & 1 + \sin^2\theta\sin^2\phi & \sin\theta\cos\theta\sin\phi \\ \sin\theta\cos\theta\cos\phi & \sin\theta\cos\theta\sin\phi & 1 + \cos^2\theta \end{pmatrix} \\
&= M \text{ (say)}. 
\end{aligned} \tag{1.25}$$

Whereas,

$$\frac{2}{r^3}\left(\mathbb{I} - 3\hat{\mathbf{r}}\hat{\mathbf{r}}\right) = \frac{2}{r^3}\begin{pmatrix} 1 - 3\sin^2\theta\cos^2\phi & -3\sin^2\theta\cos\phi\sin\phi & -3\sin\theta\cos\theta\cos\phi \\ -3\sin^2\theta\cos\phi\sin\phi & 1 - 3\sin^2\theta\sin^2\phi & -3\sin\theta\cos\theta\sin\phi \\ -3\sin\theta\cos\theta\cos\phi & -3\sin\theta\cos\theta\sin\phi & 1 - 3\cos^2\theta \end{pmatrix}$$
$$= N \text{ (say).} \tag{1.26}$$

$$\therefore \nabla^2 M_{11} = \left(1 + \sin^2\theta\cos^2\phi\right)\nabla^2\left(1/r\right) + \frac{\cos^2\phi}{r^3\sin\theta}\frac{\partial}{\partial\theta}\left[\sin\theta\frac{\partial\left(\sin^2\theta\right)}{\partial\theta}\right]$$

$$+ \frac{\sin^2\theta}{r^3\sin^2\theta}\frac{\partial^2\left(\cos^2\phi\right)}{\partial\phi^2}$$

$$= \frac{2}{r^3}\left(1 - 3\sin^2\theta\cos^2\phi\right)$$

$$= N_{11}.$$

Calculating the other components similarly, we find that indeed $\nabla^2 M = N$, and $\nabla^2 N = 0$.

Therefore, using the above relations and Eq. (1.23), we can find the second-order velocities as

$$\mathbf{v}_i = \frac{-1}{6\pi\eta\lambda_i}\mathbf{F}_i^h + \sum_{j \neq i}\left(\frac{-1}{6\pi\eta\lambda_j}\right)\left[\frac{3}{4}\left(\frac{\lambda_j}{r_{ij}}\right)\left(\mathbb{I} + \hat{\mathbf{r}}_{ij}\hat{\mathbf{r}}_{ij}\right) + \frac{1}{4}\left(\frac{\lambda_j}{r_{ij}}\right)^3\left(\mathbb{I} - 3\hat{\mathbf{r}}_{ij}\hat{\mathbf{r}}_{ij}\right)\right]\cdot\mathbf{F}_j^h$$

$$- \sum_{j \neq i}\frac{1}{36\pi\eta\lambda_j}\lambda_i^2\left\{\frac{3}{4}\lambda_j\left[2\left(\frac{1}{r^3}\right)^2\left(\mathbb{I} - 3\hat{\mathbf{r}}_{ij}\hat{\mathbf{r}}_{ij}\right)\right] + \frac{1}{4}\left(\frac{\lambda_j}{r_{ij}}\right)^3(0)\right\}\cdot\mathbf{F}_j^h$$

$$\Rightarrow \mathbf{v}_i = \frac{-1}{6\pi\eta\lambda_i}\mathbf{F}_i^h - \sum_{j \neq i}\left[\frac{1}{8\pi\eta r_{ij}}\left(\mathbb{I} + \hat{\mathbf{r}}_{ij}\hat{\mathbf{r}}_{ij}\right) + \frac{1}{24\pi\eta}\frac{\lambda_j^2 + \lambda_i^2}{r_{ij}^3}\left(\mathbb{I} - 3\hat{\mathbf{r}}_{ij}\hat{\mathbf{r}}_{ij}\right)\right]\cdot\mathbf{F}_j^h \tag{1.27}$$

$$= \frac{-1}{6\pi\eta\lambda_i}\mathbf{F}_i^h - \sum_{j \neq i}\left[\mathbf{T}\left(\mathbf{r}_{ij}\right) + \mathbf{T}_1\left(\mathbf{r}_{ij}\right)\right]\cdot\mathbf{F}_j^h, \tag{1.28}$$

where $\mathbf{T}\left(\mathbf{r}_{ij}\right)$ and $\mathbf{T}_1\left(\mathbf{r}_{ij}\right)$ denote respectively the first and the second terms in the summation in Eq. (1.27) ($\mathbf{T}\left(\mathbf{r}\right)$ being the Oseen tensor). The matrix in the square bracket on the right hand side of Eq. (1.27) is the Rotne-Prager matrix for an assembly of beads of reduced friction coefficients $\lambda_i$.

Using Eq. (1.28) we can write out in full the velocities of the three beads in

our swimmer as

$$
\mathbf{v}_1 = \frac{1}{6\pi\eta} \begin{pmatrix} 0 \\ 0 \\ \dfrac{F_1^{\text{d+s}}}{\lambda_1} + \left( \dfrac{3}{2L_1} - \dfrac{\lambda_1^2 + \lambda_2^2}{2L_1^3} \right) F_2^{\text{d+s}} + \left[ \dfrac{3}{2(L_1 + L_2)} - \dfrac{\lambda_1^2 + \lambda_3^2}{2(L_1 + L_2)^3} \right] F_3^{\text{d+s}} \end{pmatrix},
$$
$$(1.29)$$

$$
\mathbf{v}_2 = \frac{1}{6\pi\eta} \begin{pmatrix} 0 \\ 0 \\ \left( \dfrac{3}{2L_1} - \dfrac{\lambda_1^2 + \lambda_2^2}{2L_1^3} \right) F_1^{\text{d+s}} + \dfrac{F_2^{\text{d+s}}}{\lambda_2} + \left( \dfrac{3}{2L_2} - \dfrac{\lambda_2^2 + \lambda_3^2}{2L_2^3} \right) F_3^{\text{d+s}} \end{pmatrix}, \text{ and}
$$
$$(1.30)$$

$$
\mathbf{v}_3 = \frac{1}{6\pi\eta} \begin{pmatrix} 0 \\ 0 \\ \left[ \dfrac{3}{2(L_1 + L_2)} - \dfrac{\lambda_1^2 + \lambda_3^2}{2(L_1 + L_2)^3} \right] F_1^{\text{d+s}} + \left( \dfrac{3}{2L_2} - \dfrac{\lambda_2^2 + \lambda_3^2}{2L_2^3} \right) F_2^{\text{d+s}} + \dfrac{F_3^{\text{d+s}}}{\lambda_3} \end{pmatrix}.
$$
$$(1.31)$$

Here $F_i^{\text{d+s}}$ is the magnitude of the sum of the spring and driving forces on the $i^{\text{th}}$ bead, which can replace the (negative of the) drag force on the bead since the spring, the driving and the drag forces on each bead always sum to zero. It should also be noted that the arm lengths $L_i$, the forces $F_i^{\text{d+s}}$ and the velocities $\mathbf{v}_i$ in Eqs. (1.29)-(1.31) all vary with time and their time-dependence has been suppressed for brevity of expression.

Eqs. (1.29)-(1.31) replace Eq. (1.9) as the equations of motion for the present calculation. We now follow the procedure outlined in section 1.2.1, with appropriate changes such as introducing

$$
\mathbf{W}_{ij} = \left. \frac{\partial \mathbf{T}_1 (\mathbf{r}_{ij})}{\partial \mathbf{r}_j} \right|_{S_0} \tag{1.32}
$$

along with

$$
\mathbf{V}_{ij} = \left. \frac{\partial \mathbf{T} (\mathbf{r}_{ij})}{\partial \mathbf{r}_j} \right|_{S_0} \tag{1.33}
$$

as before, to find the velocity of the swimmer to one order higher in $\lambda/l$ than before. The final expression obtained for the velocity is rather long; to simplify

its expression here we state it fully for the case of equal driving force amplitudes $A = B$, in which case it reads

$$\mathbf{v}_{\text{force-RP}} = \frac{A^2\omega\lambda(28l - 45\lambda)\left[(2l - 5\lambda)k^2 + 24\pi^2\eta^2\omega^2\lambda^2l\right])}{192l^3\left[(l - 5\lambda)k^4 + 4\pi^2\eta^2\omega^2\lambda^2(8l - 33\lambda)k^2 + 144\pi^4\eta^4\omega^4\lambda^4l\right]}\hat{\mathbf{z}},$$
(1.34)

where the subscript 'force-RP' denotes the use of the Rotne-Prager matrix in finding the velocity within the force-based formulation.

We can also find the corresponding expression in the stroke-based formulation, by extending the calculation in Golestanian and Ajdari [2008] using Eqs. (1.29)-(1.31) in place of Eq. (1.9). In terms of the swimming stroke specified in Eq. (1.1), the velocity comes out to be

$$\mathbf{v}_{\text{stroke-RP}} = \frac{(28l - 99\lambda)\lambda d_1 d_2\omega\sin(\phi_1 - \phi_2)}{24l^2(4l - 17\lambda)}\hat{\mathbf{z}},$$
(1.35)

again for equal reduced friction coefficients $\lambda_i = \lambda$ of the beads and equal mean lengths $l_i = l$ of the two arms of the swimmer, and where the subscript 'stroke-RP' marks the stroke-based nature of the formulation and the use of the Rotne-Prager matrix instead of the Oseen tensor.

We observe that the velocity expressions in Eqs. (1.34) and (1.35) reduce to those in Eqs. (1.14) and (1.2), respectively, when only the lowest order terms in $\lambda/l$ are kept in the numerator and the denominator, as they should. We also note that the difference between the two velocity expressions in the stroke-based formulation is only of a geometric factor at the beginning of the expression, which is not the case for the velocity expressions obtained from the two force-based formulations.

**Comparison of different theoretical velocity formulae**

We can compare the four theoretical velocity formulae obtained for our swimmer, namely by using the force-centric and the stroke-centric approaches to two different orders in $\lambda/l$. Fig. 1.3 shows such a comparison for a swimmer composed of beads with $\lambda_i = \lambda = 4$ lattice units and with varying mean arm lengths. This simple comparison sheds light on a few interesting features. Firstly, and as expected, the four velocity expressions converge to the same curve as the $\lambda/l$ ratio becomes smaller. Importantly, the two curves (in blue and black) corresponding to the lowest order expressions in $\lambda/l$ envelope the curves (in red and green) which result on using the higher order theory. This suggests that the true velocity expression lies in between the red and the green curves, and, if that is so, that shows that
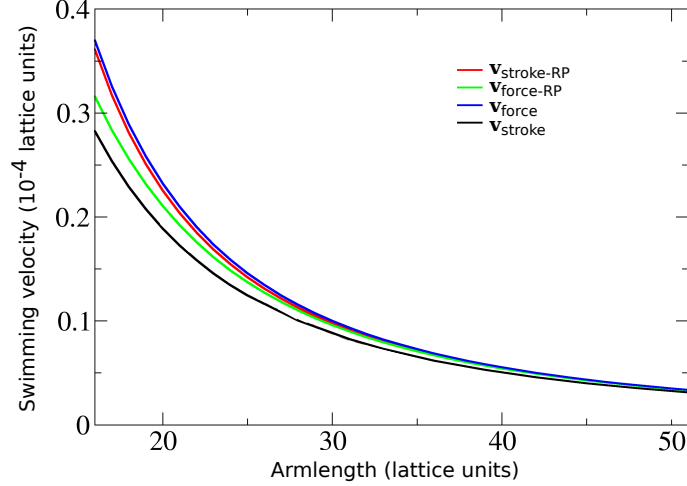
Figure 1.3: Comparison of theoretically calculated velocities of a swimmer as a function of its arm length, from both force- and stroke-based approaches.

the force-based curve in blue approximates it better than the stroke-based one in black. We also see that the difference between the lowest order force-based curve (in blue) and the higher order one (in green) is quite small, $\lesssim 5\%$, for $\lambda/l$ ratios of $1/5$ or smaller. We shall therefore in all our subsequent investigations use the lowest order expression in the velocity, $\mathbf{v}_{\text{force}}$, as the higher order expression provides only a small correction, the significance of which is negligible when compared with lattice Boltzmann simulations of the swimmer as presented subsequently in the thesis.

### 1.2.3   Velocity calculation for a swimmer with deformable beads §

We now extend the method described in section 1.2.1 to enable the inclusion of deformable beads in the model. The deformability of the beads is taken into account in the model by allowing the reduced friction coefficient $\lambda_i$ to be weakly variable in time. For a cyclic variation in $\lambda_i(t)$, as will be obtained in the steady

---

§This section has been adapted from publication **P3** [Pande *et al.*, 2016a], with changes for consistency.

state motion of the swimmer, it can be expressed in a Fourier series in $\omega t$ as

$$\lambda_i(t) = a_i + \sum_{n=1}^{\infty} b_i^n \sin\left(n\omega t + \phi_i^n\right), \quad i = 1, 2, 3. \tag{1.36}$$

Here $a_i$ is the reduced friction coefficient of the mean shape of the $i^{\text{th}}$ bead, and $b_i^n$ and $\phi_i^n$ are the amplitude and the phase shift of the contribution from the $n^{\text{th}}$ frequency mode. The condition of weak deformability is satisfied by requiring $b_i^n/a_j \ll 1$ and $b_i^n/|\xi_j(t)| \ll 1$ to hold for all $i$, $j$, and $n$ and time $t$. In the calculation, we shall assume that $\lambda_i(t)$ and thus all the coefficients in Eq. (1.36) are known, as will be the case when, for instance, the analysis is done after the corresponding simulation or experiment is performed. This is therefore a partly geometry-based approach, even though it is not stroke-based, because the swimming stroke itself is not known at the beginning of the calculation.

Due to a varying $\lambda_i(t)$, the time derivative $\dot{\mathbf{C}}(t)$ of the centre of reaction of the swimmer too is redefined as

$$\dot{\mathbf{C}}(t) = \sum_{i=1}^{3} \lambda_i(t)\dot{\mathbf{R}}_i(t) / \sum_{i=1}^{3} \lambda_i(t) \tag{1.37}$$

$$= \frac{\sum\limits_{i=0} \left( a_i + \sum\limits_{n=1}^{\infty} b_i^n \sin\left(n\omega t + \phi_i^n\right) \dot{\mathbf{R}}_i(t) \right)}{\left( \sum\limits_{j=1}^{3} a_j \right) \left( 1 + \sum\limits_{k=1}^{3} \sum\limits_{m=1}^{\infty} \bar{b}_k^m \sin(m\omega t + \phi_k^m) \right)}, \tag{1.38}$$

where $\bar{b}_k^m = b_k^m / \sum\limits_{l=1}^{3} a_l$. Here $\dot{\mathbf{R}}_i(t)$ can be written, using Eqs. (1.8), (1.9) and (1.36), as

$$\dot{\mathbf{R}}_i(t) = \frac{\mathbf{F}_i^{\text{d}}(t) + \sum\limits_{j\neq i}^{3} \mathbf{G}\left(\mathbf{R}_i(t) - \mathbf{R}_j(t)\right)}{6\pi\eta \left( a_i + \sum\limits_{n=1}^{\infty} b_i^n \sin\left(n\omega t + \phi_i^n\right) \right)}$$

$$+ \sum_{j\neq i}^{3} \mathbf{T}\left(\mathbf{R}_i(t) - \mathbf{R}_j(t)\right) \cdot \left[ \mathbf{F}_j^{\text{d}}(t) + \sum_{k\neq j}^{3} \mathbf{G}\left(\mathbf{R}_i(t) - \mathbf{R}_j(t)\right) \right]. \tag{1.39}$$

Combining this with Eqs. (1.12)-(1.13) and the fact that, as in the rigid bead case,

58

the spring and driving forces always sum to zero, we get

$$\dot{\mathbf{C}}(t) = \frac{\left(1 - \sum_{p=1}^{3} \sum_{m=1}^{\infty} \bar{b}_p^m \sin(m\omega t + \phi_p^m)\right)}{\sum_{j=1}^{3} a_j} \times$$

$$\sum_{i=1}^{3} \sum_{j \neq i}^{3} \left\{ \left( a_i + \sum_{n=1}^{\infty} b_j^n \sin(n\omega t + \phi_j^n) \right) \cdot \left( \mathbf{T}_{ij} + \left( \boldsymbol{\xi}_i(t) - \boldsymbol{\xi}_j(t) \right) \cdot \mathbf{V}_{ij} \right) \cdot$$

$$\left( \mathbf{F}_j^{\mathrm{d}}(t) + \sum_{k \neq j}^{3} \left( \boldsymbol{\xi}_j(t) - \boldsymbol{\xi}_k(t) \right) \cdot \mathbf{H}_{jk} \right) \right\}. \tag{1.40}$$

Making use of the condition $b_i^n / |\boldsymbol{\xi}_j(t)| \ll 1$, we expand all terms in Eq. (1.11) to the lowest surviving order in $\boldsymbol{\xi}_i(t)$. As in the rigid bead case, the zeroth and first order terms in $\boldsymbol{\xi}_i(t)$ or $\mathbf{F}_j^{\mathrm{d}}(t)$ average to zero over a cycle. Checking now for the second order terms, it can be easily shown that only the $n = 1$ terms for the surface fluctuation $\sum_{n=1}^{\infty} b_j^n \sin(n\omega t + \phi_j^n)$ contribute, since all the other modes also evaluate to zero due to the orthogonality of the sinusoidal functions.

Therefore, given sufficiently weak periodic surface deformations of any functional form, only the driving frequency modes contribute to the swimming motion. The terms that survive in Eq. (1.40) are all sinusoidal functions, and the equation then becomes straightforward to solve, finally yielding an expression for $\mathbf{v}_{\mathrm{def}}$ of the form

$$\mathbf{v}_{\mathrm{def}} = \mathbf{v}_{\mathrm{force}} + \sum_{i=1}^{3} \mathbf{m}_i b_i^1, \tag{1.41}$$

where $\mathbf{v}_{\mathrm{def}}$ denotes the velocity of the swimmer in the deformable bead case and $\mathbf{v}_{\mathrm{force}}$ is as found in Eq. (1.11). The coefficients $\mathbf{m}_i$ are independent of the shape deformation amplitudes $b_j^1$. Due to their bulky expressions, these coeffficients are not presented here.

In conclusion, Eqs. (1.11) and (1.41) provide the expressions for the velocity of a three bead swimmer with rigid and weakly deformable beads, respectively, and in the next few chapters we shall explore various properties of microswimming with the help of these these analytical expressions and the simulation methods described in the next chapter.

## 1.2.4 Calculation of swimmer effective radius $r_{\text{eff}}$ [¶]

In the rest of the thesis, particularly in chapter 6, we will occasionally make use of the effective radius $r_{\text{eff}}$ of our swimmer. Here we present its calculation.

For negligibly small oscillation amplitudes, *i.e.* to the zeroth order in $d_i/l_j$ (from Eq. (1.1)), the $r_{\text{eff}}$ for the swimmer over a cycle is the same as that of the equilibrium configuration moving rigidly with a constant velocity. To obtain such a configuration, we let the three beads have effective friction coefficients $\lambda_1$, $\lambda_2$ and $\lambda_3$, and let constant forces $\lambda_1\mathbf{F}$, $\lambda_2\mathbf{F}$ and $\lambda_3\mathbf{F}$ respectively act on the three beads, with $\mathbf{F} = F\hat{\mathbf{z}}$. We will first show that in the steady state these forces indeed result in a rigid equilibrium configuration, *i.e.* the springs are unextended.

Assume that in the steady state both the springs are extended, with the respective extensions being $\Delta l_1$ and $\Delta l_2$. Then, the forces on the left, middle and right spheres, apart from the hydrodynamic forces, are respectively $(\lambda_1 F + k\Delta l_1)$, $(\lambda_2 F + k\Delta l_2 - k\Delta l_1)$, and $(\lambda_3 F - k\Delta l_2)$, all in the $+z$-direction. Since we are considering the steady state, all the three spheres are assumed to be moving with the same speed, which equals $\dfrac{F_i^{\text{d+s}}}{6\pi\eta\lambda_i}$. Therefore, we have

$$\frac{(\lambda_1 F + k\Delta l_1)}{6\pi\eta\lambda_1} = \frac{(\lambda_2 F + k\Delta l_2 - k\Delta l_1)}{6\pi\eta\lambda_2} = \frac{(\lambda_3 F - k\Delta l_2)}{6\pi\eta\lambda_3}. \qquad (1.42)$$

$$\Rightarrow F + \frac{k\Delta l_1}{\lambda_1} = F + \frac{k\Delta l_2}{\lambda_2} - \frac{k\Delta l_1}{\lambda_2} = F - \frac{k\Delta l_2}{\lambda_3}. \qquad (1.43)$$

$$\Rightarrow \frac{\Delta l_1}{\lambda_1} = \frac{\Delta l_2 - \Delta l_1}{\lambda_2} = -\frac{\Delta l_2}{\lambda_3}. \qquad (1.44)$$

If $\Delta l_1$ is positive (negative), then $\Delta l_2$ must be negative (positive), and then the middle term is negative (positive), resulting in a contradiction. Therefore, the only solution to the above equation is

$$\Delta l_1 = \Delta l_2 = 0 \qquad (1.45)$$

which is what we wanted to show.

---

[¶] This section has been adapted from publication **P4** [Pande* *et al.*, 2016], with changes for consistency.

Then the velocity of the swimmer in the steady state is

$$\mathbf{v}_{\text{force}} = \frac{1}{3T} \int_0^T \sum_{i=1}^3 \mathbf{v}_i \, dt$$

$$= \frac{1}{3T} \int_0^T \sum_{i=1}^3 \left[ \frac{1}{6\pi\eta\lambda_i} \lambda_i \mathbf{F} + \sum_{j\neq i}^3 \mathbf{T} \left( \mathbf{R}_i - \mathbf{R}_j \right) \cdot \lambda_j \mathbf{F} \right] dt. \tag{1.46}$$

As the springs are always at their rest lengths, all the terms in the above expression are time-independent, and therefore can be taken out of the time integral. So

$$\mathbf{v}_{\text{force}} = \frac{\mathbf{F}}{6\pi\eta} + \frac{1}{3} \left[ \sum_{i=1}^3 \sum_{j\neq i}^3 \lambda_j \mathbf{T} \left( \mathbf{R}_i - \mathbf{R}_j \right) \right] \cdot \mathbf{F}$$

$$= \frac{\mathbf{F}}{6\pi\eta} + \frac{1}{3} \left( \lambda_1 \mathbf{T}_{12} + \lambda_1 \mathbf{T}_{13} + \lambda_2 \mathbf{T}_{21} + \lambda_2 \mathbf{T}_{23} + \lambda_3 \mathbf{T}_{31} + \lambda_3 \mathbf{T}_{32} \right) \cdot \mathbf{F}, \tag{1.47}$$

where $\mathbf{T}_{ij}$ is shorthand for $\mathbf{T} \left( \mathbf{R}_i - \mathbf{R}_j \right)$.

Now,

$$\lambda_1 \left( \mathbf{T}_{12} + \mathbf{T}_{13} \right) \cdot \mathbf{F} = \frac{1}{8\pi\eta} \left( \frac{1}{l_1} + \frac{1}{l_1 + l_2} \right) (2\lambda_1 \mathbf{F}).$$

$$\lambda_2 \left( \mathbf{T}_{21} + \mathbf{T}_{23} \right) \cdot \mathbf{F} = \frac{1}{8\pi\eta} \left( \frac{1}{l_2} + \frac{1}{l_1} \right) (2\lambda_2 \mathbf{F}).$$

$$\lambda_3 \left( \mathbf{T}_{31} + \mathbf{T}_{32} \right) \cdot \mathbf{F} = \frac{1}{8\pi\eta} \left( \frac{1}{l_1 + l_2} + \frac{1}{l_2} \right) (2\lambda_3 \mathbf{F}).$$

Therefore,

$$\mathbf{v} = \frac{\mathbf{F}}{6\pi\eta} + \frac{2\mathbf{F}}{3} \left( \frac{1}{8\pi\eta} \right) \left[ \lambda_1 \left( \frac{1}{l_1} + \frac{1}{l_1 + l_2} \right) + \lambda_2 \left( \frac{1}{l_1} + \frac{1}{l_2} \right) \right.$$

$$\left. + \lambda_3 \left( \frac{1}{l_1 + l_2} + \frac{1}{l_2} \right) \right]$$

$$= \frac{\mathbf{F}}{6\pi\eta} \left\{ 1 + \frac{1}{2} \left[ \lambda_1 \left( \frac{1}{l_1} + \frac{1}{l_1 + l_2} \right) + \lambda_2 \left( \frac{1}{l_1} + \frac{1}{l_2} \right) \right. \right.$$

$$\left. \left. + \lambda_3 \left( \frac{1}{l_1 + l_2} + \frac{1}{l_2} \right) \right] \right\}. \tag{1.48}$$

By the definition of $r_{\text{eff}}$, we have

$$\mathbf{v} = \frac{\mathbf{F}_{\text{total}}}{6\pi\eta r_{\text{eff}}} = \frac{(\lambda_1 + \lambda_2 + \lambda_3)\mathbf{F}}{6\pi\eta r_{\text{eff}}}, \tag{1.49}$$

from where we get

$$\frac{1}{r_{\text{eff}}} = \frac{1}{\lambda_1 + \lambda_2 + \lambda_3}\left\{1 + \frac{1}{2}\left[\lambda_1\left(\frac{1}{l_1} + \frac{1}{l_1 + l_2}\right) + \lambda_2\left(\frac{1}{l_1} + \frac{1}{l_2}\right)\right.\right.$$
$$\left.\left. + \lambda_3\left(\frac{1}{l_1 + l_2} + \frac{1}{l_2}\right)\right]\right\}. \tag{1.50}$$

For identical and equidistant beads (for which we have $\lambda_i = \lambda$ and $l_i = l$), the above expression for the swimmer effective radius simplifies to

$$r_{\text{eff}} = \frac{6\lambda l}{2l + 5\lambda}. \tag{1.51}$$

For identical beads, the expression in Eq. (1.51), correct to the first order in $\lambda/l$ and the zeroth order in $d_i/l$, can also be obtained from the swimmer effective radius provided in Eq. (40) in Golestanian and Ajdari [2008].

# 2

# Simulation methods

To run the different simulations discussed in this thesis, we use one of two simulation systems, the waLBerla-*pe* system [Feichtinger *et al.*, 2011] and the LB3D code [Krüger *et al.*, 2013, 2014]. While both these systems utilise the lattice Boltzmann method (LBM) for the simulation of the fluid, they differ in the way the particles within the fluid are described. In the waLBerla-*pe* system, the particles are handled by *pe* which is a rigid body physics engine, and thus can only simulate objects which are composed of unions of bodies which are rigid. In LB3D, in contrast, the particles are described using the immersed boundary method (IBM), which treats every object as deformable in essence. In the following we first introduce the lattice Boltzmann method and then give details of both the simulation systems employed.

## 2.1   The lattice Boltzmann method (LBM)

The main philosophy behind the LBM is the use of simple local models–in which each fluid element (lattice cell) requires information only about the fluid elements in its vicinity–which incorporate the physics of microscopic processes, while requiring only the averaged macroscopic properties in a fluid, like the momentum, to satisfy the macroscopic equations [Succi, 2001]. It was introduced in McNamara and Zanetti [1988], and utilises the Boltzmann equation (see Eq. (2.1)) to solve for the microscopic particle velocity distribution function, from the hydrodynamic moments of which macroscopic quantities like the mass density and the momentum density can be obtained [Yu *et al.*, 2003, Aidun and Clausen, 2010]. The method was subsequently expanded theoretically in Higuera and Jimenez [1989], Koelman [1991], Qian *et al.* [1992] and Chen *et al.* [1992]. It preserves the simplicity and locality of operations of the lattice gas automata method [Hardy *et al.*, 1976, Frisch *et al.*, 1986, 1987]–in which it finds its origins–while avoiding its

shortcomings. The LBM is a relatively simple method which can resolve flow problems without explicitly solving the Navier-Stokes equations (Eq. (0.1)), and is highly scalable and parallelisable. Unlike direct Navier-Stokes solvers which are limited to continuum descriptions–to be precise, those where the ratio of the molecular mean free path to a characteristic flow length scale (a ratio termed the Knudsen number $Kn$) is negligibly small–the LBM can be used for mesoscopic flows which have a wider range of $Kn$. The continuum description of the Navier-Stokes equation can still be formally derived by expanding the distribution functions in the lattice Boltzmann equation (Eq. (2.2)) in terms of the scaled time and space variables, as pioneered by Chapman and Enskog [Chapman, 1916, Enskog, 1917]. For all these reasons, it has gained wide popularity in the last three decades and has found use in solving a number of problems with simple, complex and multi-phase flows (for some comprehensive reviews, see Benzi *et al.* [1992], Chen and Doolen [1998], Luo [2000] and Aidun and Clausen [2010]).

From a physicist's point of view, the main ingredient in the LBM is the lattice Boltzmann equation, which is simply a discretized form of the Boltzmann equation. To see this, begin with the Boltzmann equation

$$\left(\frac{\partial}{\partial t} + \mathbf{v} \cdot \nabla\right) f(\mathbf{r}, \mathbf{v}, t) = Q, \tag{2.1}$$

for the particle distribution function (PDF) $f(\mathbf{r}, \mathbf{v}, t)$, which is the probability of finding a particle with velocity $\mathbf{v}$ at position $\mathbf{r}$ at time $t$. Here $Q$ is a complicated integral collision operator which balances the particle interactions and thus ensures that Eq. (2.1) is a statement of particle conservation. In Boltzmann's equation, the precise form of $Q$ comes from assuming Boltzmann's famous *Stosszahlansatz* hypothesis of binary collisions and molecular chaos. In the LBM, the collision operator can be more general, and can in principle incorporate many-particle collisions. Various simplifications of this operator are possible and become important in particular executions of the LBM due to the complexity of the term (see for instance the simplifications in sections 2.2.1 and 2.2.2), but here we leave it in its most general form. Discretisation of space in terms of a set of chosen points which move with velocities $\mathbf{c}_i$, and then use of a coupled finite difference method for the space and time derivatives (with the space and time differences coupled as $\Delta \mathbf{r}_i = \mathbf{c}_i \Delta t$ and $\Delta t = 1$) lead to the general, non-linear, lattice Boltzmann equation (LBE)

$$f_i^*(\mathbf{r}_i^* + \mathbf{c}_i^*, t^* + 1) - f_i^*(\mathbf{r}_i^*, t^*) = Q^*(\mathbf{r}_i^*, t^*) \tag{2.2}$$

where the primes denote dimensionless (lattice) counterparts of the respective variables. Due to the possibility of including many-particle collisions in $Q$, the
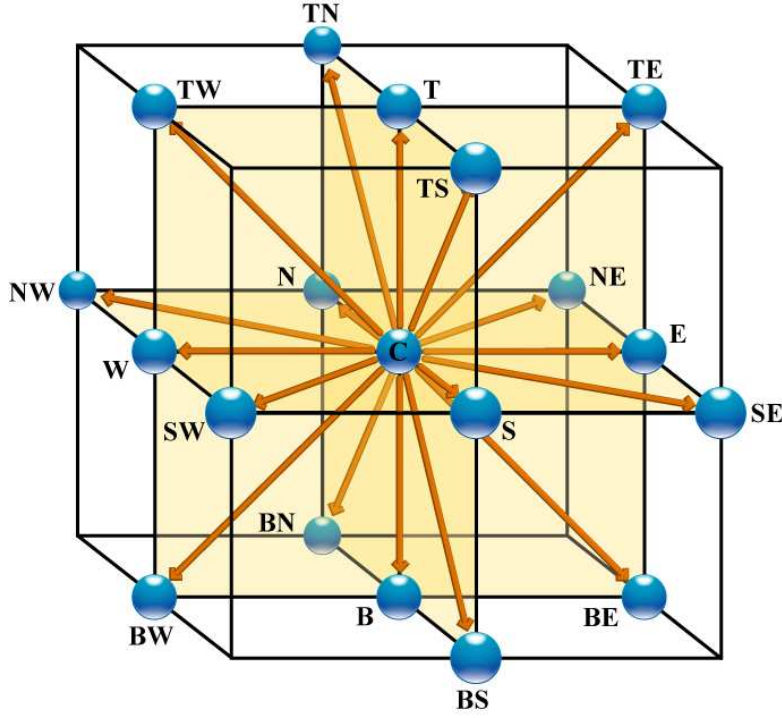
Figure 2.1: The D3Q19 velocity phase discretisation model. The direction labels are 'N' for 'north', 'S' for 'south', 'E' for 'east', 'W' for 'west', 'T' for 'top', 'B' for 'bottom' and 'C' for 'centre'. Figure taken from publication **P6** [Pickl *et al.*, 2012].

LBE can be used for dense fluids instead of dilute gases which the Boltzmann equation is restricted to due to its requirement of the collisions being always binary.

In both the simulation frameworks employed in this thesis we use the common D3Q19 velocity phase discretisation model originally developed in Qian *et al.* [1992], which has 19 discrete velocity directions (Q19) in three dimensions (D3) (Fig. 2.1). The LBE in Eq. (2.2) gives the time evolution of the PDFs, and is usually solved in two steps, known as the collision step and the streaming step. The collision step is a local relaxation of the PDFs $f_i$ towards their equilibrium values $f_i^{\text{eq}}$, which are given by truncating the Maxwell-Boltzmann distribution as

$$f_i^{\text{eq}}(\rho, \mathbf{v}) = \omega_i \rho \left[ 1 + \frac{\mathbf{c}_i \cdot \mathbf{v}}{c_s^2} + \frac{(\mathbf{c}_i \cdot \mathbf{v})^2}{2c_s^4} - \frac{\mathbf{v} \cdot \mathbf{v}}{2c_s^2} \right], \qquad (2.3)$$

where $\rho$ is the fluid density, $\omega_i$ are weighting constants which arise from the space discretisation of the velocity, and $c_s$ is the speed of sound on the lattice, which

in the D3Q19 model equals $c_s = 1/\sqrt{3}$. The streaming step advects all the PDFs (except the one in the 'C' direction in Fig. 2.1, pointing from a cell to the cell itself) to their neighbouring lattice sites (in the D3Q19 model) depending on the velocity. For this reason only the information of the nearest neighbours is needed at each time step. Due to this locality of the cell updates, the LBM can be implemented extremely efficiently [Pohl *et al.*, 2003, Wellein *et al.*, 2005] and can be easily parallelised [Körner *et al.*, 2005].

## 2.2   Details of the two LB simulation systems used

The two simulation systems we use, waLBerla-*pe* and LB3D, both accord with the above general description of the LBM. There are however some differences in the implementation of the method and its coupling to the respective particle solvers, which we briefly explain below.

### 2.2.1   The waLBerla-*pe* system

waLBerla (Widely Applicable Lattice-Boltzmann solver from ERLAngen) is a simulation system for the fluid which utilises the LBM as described above [Feichtinger *et al.*, 2011]. For our waLBerla simulations presented in this thesis, we use a collision operator model, called the two-relaxation time (TRT) model, which was introduced in Ginzburg *et al.* [2008]. As the name suggests, this model uses two characteristic relaxation times in the simulations, called $\lambda^+$ and $\lambda^+$, and in our implementation these relaxation times are defined as $\lambda^+ = \tau^{-1}$ and $\lambda^- = 8(2 - \tau^{-1})/(8 - \tau^{-1})$, with $\tau$ being a time scale. Such a definition of the relaxation times promotes accuracy at solid boundaries [Ginzburg *et al.*, 2008]. The TRT model divides the PDFs $f_i$ and their equilibrium values $f_i^{\text{eq}}$ into symmetric and antisymmetric parts, denoted by '$+$' and '$-$' superscripts, respectively. In terms of these quantities the collision operator $Q^*$ in Eq. (2.2) can be written as

$$Q^* = -\lambda^{+*} \left[ f_i^{+*}(\mathbf{r}_i^*, t) - f_i^{+\text{eq}*}(\rho^*, \mathbf{v}^*) \right] - \lambda^{-*} \left[ f_i^{-*}(\mathbf{r}_i^*, t) - f_i^{-\text{eq}*}(\rho^*, \mathbf{v}^*) \right].$$
(2.4)

The waLBerla system is coupled in our simulations with *pe* (Physics Engine), which can simulate arbitrary unions of some base collection of rigid bodies [Iglberger, 2010]. In *pe* the individual bodies are resolved in full, which distinguishes our simulations from many other systems wherein the immersed bodies are treated as point masses. This becomes important when, for instance, swimmers of different shapes need to be compared [Pickl *et al.*, 2012]. Like waLBerla, *pe* supports parallelised simulations running on up to hundreds of thousands of cores [Götz *et al.*, 2010].
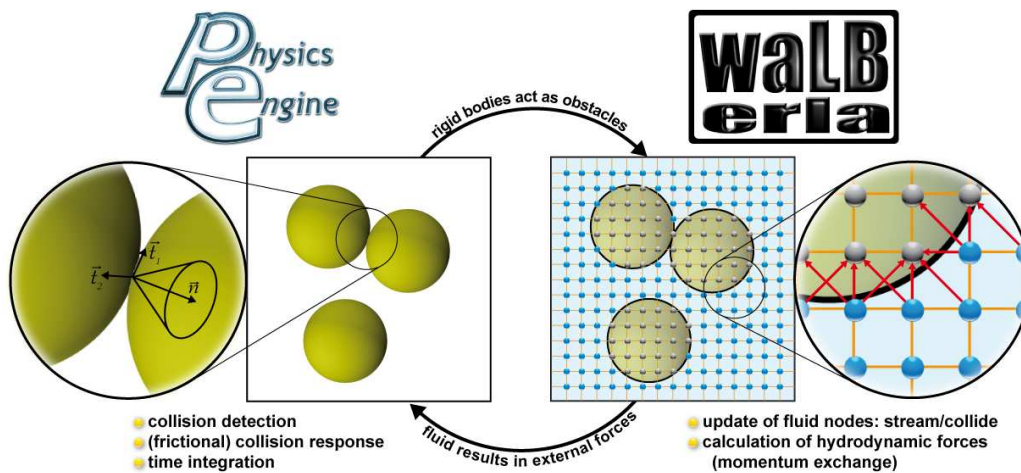
Figure 2.2: Illustration of the two-way coupling of the waLBerla fluid solver and the *pe* rigid body dynamics solver. Figure taken from publication **P6** [Pickl *et al.*, 2012].

The waLBerla and *pe* systems need to be coupled together such that in waLBerla the rigid bodies simulated by *pe* appear as solid movable boundaries around which the flow occurs whereas in *pe* the fluid flow simulated by waLBerla manifests itself as hydrodynamic forces which affect the motion of the rigid bodies (Fig. 2.3). This two-way coupling is achieved by the following process. At each time step the rigid bodies in the *pe* are mapped onto the lattice Boltzmann grid of waLBerla with (in our simulations) a staircase approximation. The fluid at the surface of each rigid body is then given the velocity of the local body surface, due to the assumed no-slip boundary condition. Then the identities of appropriate fluid and object cells, specified by respective flags, are interchanged and the streaming and collision steps are performed. Finally the total forces on each body are calculated and the body is moved accordingly. The body is then mapped again to the LBM grid in the next time step, commencing a new cycle of the coupling process. Descriptions of this method and its validation are provided in Binder *et al.* [2006] and Iglberger *et al.* [2008].

## 2.2.2   The LB3D system[*]

The LB3D code [Krüger *et al.*, 2013, 2014] combines the lattice-Boltzmann method (LBM) for the fluid, the finite element method (FEM) for the deformable bodies

---

[*]This section has been adapted from publication **P3** [Pande *et al.*, 2016a], with changes for consistency.
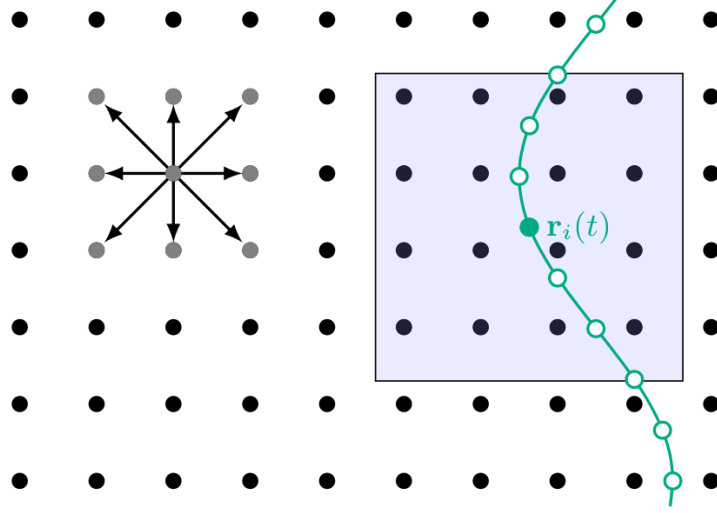
Figure 2.3: The fixed Eulerian and moving Lagrangian meshes in the LB3D code. Here $\mathbf{r}_i(t)$ is a membrane node, and the grey square region around it denotes the interpolation stencil which determines the lattice nodes which are included while interpolating the fluid velocities onto the membrane node, and then reflecting the membrane deformation forces onto the fluid. Figure taken from [Krüger *et al.*, 2013].

immersed in the fluids, and the immersed boundary method (IBM) for the coupling between the fluid and the bodies. The deformable surfaces of the bodies are represented by meshes which are generated by successively subdividing an initially coarse mesh which is in the shape of a regular icosahedron. These meshes have $n$ triangular faces each, with $n = 720$ for all the simulations performed with the LB3D code presented in this thesis. The deformable bodies contain fluid which has the same density and viscosity as the external fluid.

In LB3D we use a single time relaxation scheme, the popular Bhatnagar–Gross–Krook (BGK) model introduced in Bhatnagar *et al.* [1954], in which the collision operator $Q^*$ of Eq. (2.2) is given by

$$Q^* = -\frac{f_i^*(\mathbf{r}_i^*, t) - f_i^{\mathrm{eq}*}(\rho^*, \mathbf{v}^*)}{\tau},\tag{2.5}$$

where $\tau$ is again a time scale, here defining only one relaxation parameter in contrast to the TRT model.

For the fluid a fixed Eulerian grid is used, while the surface nodes of the particles immersed in the fluid are represented by a moving Lagrangian mesh, which must be coupled to the fluid lattice. This coupling is performed in two stages. In the first stage, the velocity of the fluid at each membrane node is interpolated

using an appropriate stencil from its velocity at the fluid lattice points–these velocities are themselves found within the LBM from the collision and streaming steps described in section 2.1–because of an assumed no-slip boundary condition between the membrane and the fluid. The membrane node in question is then advected using this velocity determined. In the second stage the deformations that are induced in the membrane due to the advection of its nodes in the first step are reflected onto the fluid, again with the interpolation stencil used in the first stage, through a reaction force which is calculated using a constitutive model for the membrane.

This constitutive model, for us, is based on the total energy of deformation of the $i^{\text{th}}$ body, which in all the simulations reported in this thesis is a quasi-spherical bead. The deformation energy is specified to be

$$W_i = W_i^{\text{S}} + W_i^{\text{B}} + W_i^{\text{A}} + W_i^{\text{V}}, \qquad (2.6)$$

where the superscripts $S$, $B$, $A$ and $V$ label the energy contributions due to strain, bending, surface area and volume, respectively. The strain energy is as given by the Skalak model [Skalak *et al.*, 1973], and has two associated stiffness moduli, the shear modulus $k_i^{\text{S}}$ and the area dilation modulus $k_i^{\alpha}$. The bending energy $W_i^{\text{B}}$ (with the associated bending modulus $k_i^{\text{B}}$) is significant in the presence of strong local curvatures. The global volume and surface area energies $W_i^{\text{A}}$ and $W_i^{\text{V}}$ (with corresponding area and volume moduli $k_i^{\text{A}}$ and $k_i^{\text{V}}$, respectively) impose restrictions on the change of bead surface area and volume, with these energies being the lowest if the volume and the surface area are at their equilibrium values. For more details on the different deformation energy parameters, see [Krüger *et al.*, 2011].

By the nature of the two simulation systems, the wALBERLA-*pe* pairing is well-suited for simulating the bead-spring swimmer when the beads are rigid, while the LB3D code is useful for swimmers with both rigid and deformable beads. In our investigations in this thesis, we shall use these systems accordingly.

*3*

# Verification and analysis of theoretical velocity calculation

The swimmer model that we have set up allows us to explore different aspects of low Reynolds number motion in a controlled manner. As we shall show, our theoretical results, combined with lattice-Boltzmann simulations which in each case back up the theory, help us to shed light on some important general features of microswimming which before our work went undiscovered or unexplained. Before we do so, we shall check how well the basic results predicted by our model, in terms of the swimming stroke and velocity, compare to the simulations. This study of the relative errors between the theory and the simulations will provide helpful pointers for more involved comparisons.

## 3.1 Basic comparison between theory and simulations *

For the sake of this comparison we run simulations using the wALBERLA-*pe* system with the beads in the swimmer rigid and far away from any boundaries. The simulation parameters are here provided in the lattice units. The fluid has a kinematic viscosity of $\nu = 1/3$ (which in the simulations also equals its dynamic viscosity $\mu$, since the density of the fluid $\rho$ is taken to be 1 in lattice Boltzmann simulations). The relaxation time is set to $\tau = 1.5$, and the spring stiffness to $k = 0.0347$. The radius of each sphere is $r = 4\Delta x$, where $\Delta x$ denotes one lattice cell length. The density of the fluid is $\rho_s = 1.492$, which makes the density of the swimmer body comparable to that of the surrounding fluid as is the case with

---

*This section has been adapted from publication **P5** [Pickl *et al.*, 2016], with changes for consistency.
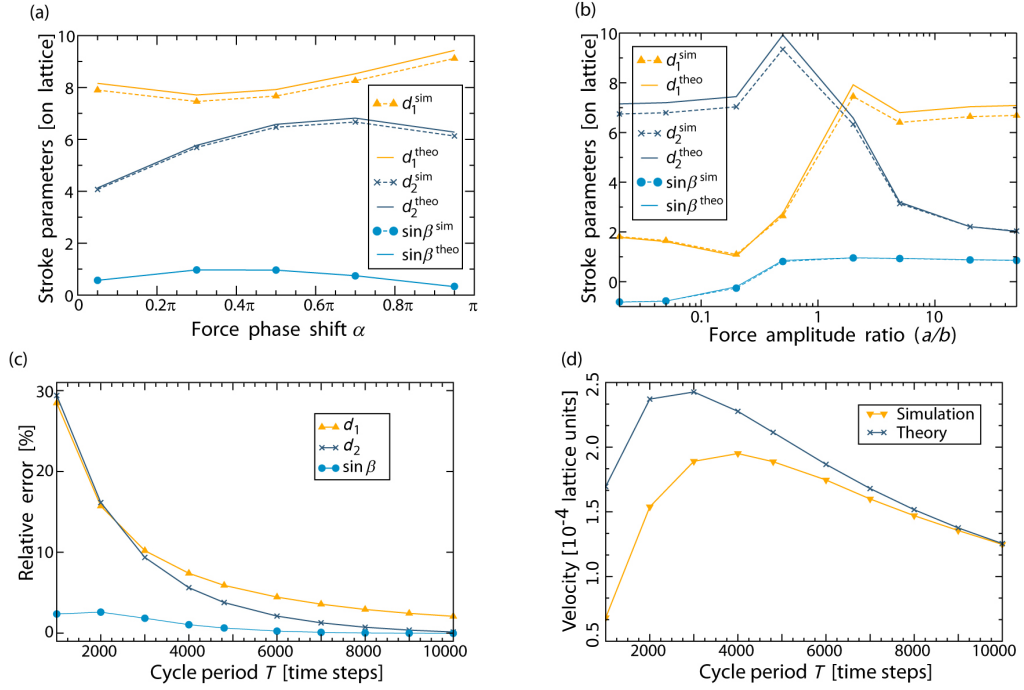
Figure 3.1: Dependence of the stroke parameters on (a) the force phase shift $\alpha$, (b) the force amplitude ratio $A/B$, and (c) the cycle period $T$; and (d) comparison of velocity from theory and simulations for different cycle periods. The superscripts 'sim' and 'theory' refer to simulations and theory, respectively. Figure taken from publication **P5** [Pickl *et al.*, 2016].

most micro-organisms. Each arm in the swimmer has a rest length of $l = 20\Delta x$. The simulations are carried out in a box of size $x \times y \times z = 1200 \times 800 \times 800 \, \Delta x^3$, and six full swimming cycles are performed in total to ensure that the steady state is reached.

Figs. 3.1 (a) and (b) show a comparison of the arm length amplitudes $d_1$ and $d_2$ and the stroke phase shift $\sin\beta$ from the theoretical expressions of Eqs. (1.15)-(1.17) and from simulations. In these plots the horizontal axis marks increasing values of the force phase shift $\alpha$ and the force amplitude ratio $A/B$, respectively, for a cycle period of 4800 time steps. The first observation we make is that for our swimmer, the oscillation amplitude of the leading arm, $d_2$, is larger than that of the trailing arm, $d_1$, for $B > A$. This is consistent with the formulae in Eqs. (1.15), from where it is clear that $d_2 > d_1$ if $\sin\alpha > 0$ and $B > A$. The errors are less than 6% in both Figs. 3.1 (a) and (b), showing that the ratio $\lambda/l = 0.2$ is sufficiently small for the theory to give accurate results. Note that this is similar

to the error estimate found in section 1.2.2 with regard to Fig. 1.3. Moreover, the errors become even smaller when the cycle period is increased (Fig. 3.1 (c)), since the accuracy of the force resolution in the simulations increases with the cycle period.

A similarly good agreement is found between theory and simulations when the respective swimmer velocities are compared (Fig. 3.1 (d)). As is the case with the stroke parameters, the relative errors go down as the cycle period increases (to 0.5% for a cycle period of 10000).

We stress the fact that the strict requirements of the theory, that of the beads in the swimmer being very far from each other and oscillating with very small amplitudes, are not fully satisfied in the simulations, owing to considerations of preserving a reasonable simulation time. The simulations additionally suffer from the unwanted influences of the boundaries which modify the flow fields such that they are inevitably different than they would be in an infinite expanse of fluid as the theory assumes. Lastly, the discretisation of space and time too affects the results–as can easily be seen by increasing the time step and the lattice cell size by a few orders of magnitude–and is another unavoidable feature of the simulations that the theory turns a blind eye to. The results presented in this section affirm, however, that in spite of all the potential sources of conflict between the idealised assumptions of the theory and the practical contingencies of the simulations, the two work well enough together, and their agreement can be systematically heightened by an appropriate choice of the different parameters (such as large enough cycle periods).

## 3.2 Influence of driving parameters: pusher/puller nature [†]

Having verified the basic success of the theory in describing the swimming motion, we now study some of the consequences of it. We first study the effects of the driving forces of Eq. (1.3) on the motion of a swimmer with rigid beads. From Eq. (1.11), it may be seen that the velocity magnitude $|\mathbf{v}_{\text{force}}|$ is the highest when the driving force phase difference $\alpha$ is $\pi/2$ if the driving force amplitudes $A$ and $B$ are related as $A \geq B$, and when $\alpha$ is $-\pi/2$ if $A < B$. If one increases both the force amplitudes by the same factor, there is a corresponding quadratic increase in the velocity.

Our model allows for an analytical prediction of the pusher or puller nature of the swimmer (see section 0.1.4 in the introductory chapter). We find that this

---

[†]This section has been adapted from publication **P1** [Pande and Smith, 2015], with changes for consistency.

nature depends upon the relation

$$\left(\frac{B}{A} - \frac{A}{B}\right)^{-1} \sin\alpha \gtrless \frac{2\pi\eta\omega\lambda k}{k^2 + 12\pi^2\eta^2\omega^2\lambda^2}. \tag{3.1}$$

When the left hand side of relation (3.1) is larger, then the swimmer moves in the direction of the bead with the higher force amplitude, and is consequently a puller. On the other hand, if the right hand side is larger, then the swimmer moves in the opposite direction, and is a pusher. This is borne out by the analysis of the obtained flow-fields. The above relation fails to hold when the velocity becomes very low; in this case, the nature of the swimmer is not clearly defined.
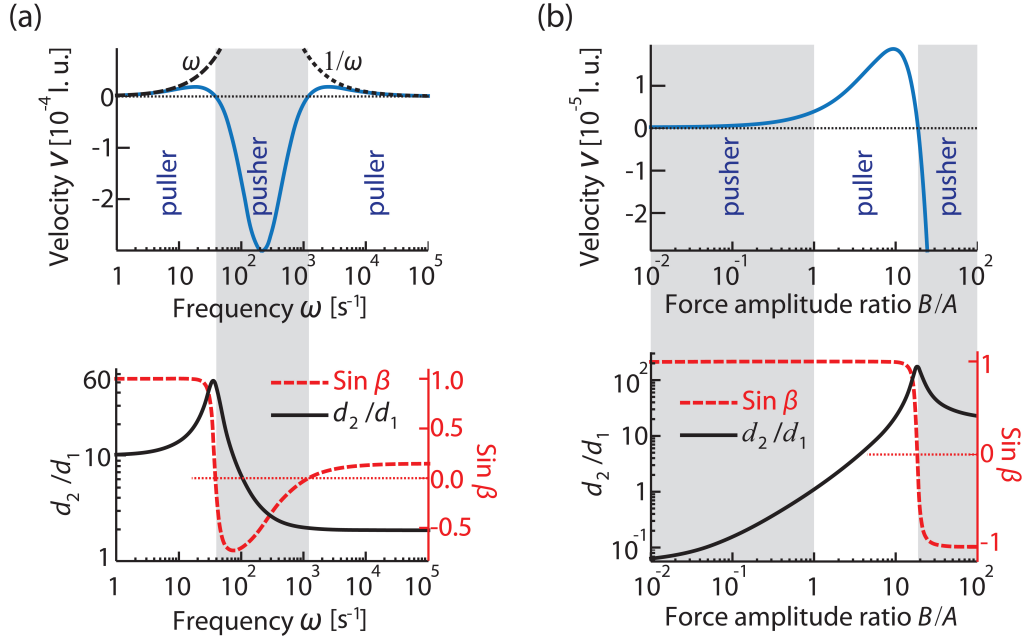


Figure 3.2: Velocity $\mathbf{v}_{\mathrm{force}}$, armlength ratio $d_2/d_1$ and stroke phase difference $\sin\beta$ of a swimmer as a function of (a) frequency $\omega$, and (b) force ratio $B/A$. Here $\alpha = \pi/2$. Note that $\mathbf{v}_{\mathrm{force}} \sim \omega$ for $\omega \to 0$ and $\mathbf{v}_{\mathrm{force}} \sim 1/\omega$ for $\omega \to \infty$, in contrast to the linear dependence of the swimming velocity on the driving frequency $\omega$ for all $\omega$, when the stroke is pre-set (see Eq. 1.2). Figure taken from publication **P1** [Pande and Smith, 2015].

Relation (3.1) says that the same swimmer following essentially similar strokes may be a pusher or a puller depending on the precise parameter values of the forces it faces. For instance, the nature of the swimmer can be changed by simply applying the driving at a different rate (Fig. 3.2(a)). Similarly, this nature may change on changing the magnitude of the forces. For the force amplitudes $A$ and $B$, if the

force phase difference $\alpha$ is positive (*i.e.* $\alpha \in [0, \pi]$), then the swimmer is a pusher if $A > B$ (Fig. 3.2(b)). If $B > A$, the swimmer is a puller at small $B$, and becomes a pusher at large $B$.

Fig. 3.2 also shows the dependence of the velocity magnitude on the force parameters. For a changing ratio of $B/A$, due to the quadratic nature of the velocity curve, the global maximum of the velocity magnitude is always in the pusher regime. For other parameter changes ($\omega$, $\alpha$, $k$, $\eta$), this does not necessarily hold true.

We find that as the force amplitude ratio $B/A$ varies with $\alpha$ fixed at $\pi/2$, the stroke amplitude ratio $d_2/d_1$ becomes one at a point when the swimmer transitions from a pusher to a puller (Fig. 3.2(b)). Moreover, the maximum in the $d_2/d_1$ curve coincides with the other transition from a puller to a pusher. Similarly, as the driving frequency $\omega$ varies with $A$ and $B$ held fixed, when the relative difference between the arm oscillation amplitudes $d_2$ and $d_1$ is the largest then again the swimmer has a transition point between being a puller and a pusher (Fig. 3.2(a)).

An especially significant effect that we observe on studying the dependence of the stroke on the force parameters is the near locking of the stroke phase shift $\beta$ for large parts of the parameter space. This is highlighted when the force amplitude ratio $B/A$ is varied (lower panel of Fig. 3.2(b)), when $\sin\beta$ automatically assumes the optimal values of $+1$ or $-1$. This suggests that the swimmer has the ability to automatically synchronise its two beating arms for much of the phase space so as to achieve efficient propulsion, and is reminiscent of the phase locking observed in *Chlamydomonas* flagella when elastic connections are included [Leptos *et al.*, 2013].

## 3.3 Effect of changing the fluid viscosity on swimming [‡]

We now employ our theory in studying the ways that the fluid viscosity can affect microswimming. This is a question which has been prominent in the field ever since it was discovered a few decades ago that many micro-organisms swim faster in more viscous fluids than in less viscous ones. The first such finding was presented in Shoesmith [1960], which reported the increased motility of *Pseudomonas viscosa*, *Bacillus brevis* and *Escherichia coli* for a small increase in the viscosity of the solution; larger increases led to the motility decreasing. Similarly, in Schneider and Doetsch [1974] it was reported that many flagellated bacteria showed an increase in the velocity when the solution viscosity rose to a charac-

---

[‡]This section has been adapted from publication **P2** [Pande *et al.*, 2016b], with changes for consistency.

teristic value, and a decrease thereafter. Many other studies [Kaiser and Doetsch, 1975, Klitorinos *et al.*, 1993, Ruby and Charon, 1998, Nakamura *et al.*, 2006] have corroborated this phenomenon of the swimming being enhanced with an increase in the fluid viscosity.

The difficulty in understanding the phenomenon lies not just in its running contrary to the intuitive expectation of a more viscous fluid providing greater resistance to motion, but also to the traditional theories of microbial motion in simple fluids all of which predict the velocity to go down with the viscosity [Chwang and Wu, 1971, Azuma, 1992, Ramia *et al.*, 1993]. Theoretical explanations that have been advanced in the literature have focussed on the non-Newtonian nature of the fluid and the structure of any polymers present therein, such as the possibility of the latter forming networks inside the fluid which facilitate swimmer propulsion [Berg and Turner, 1979, Magariyama and Kudo, 2002, Nakamura *et al.*, 2006, Leshansky, 2009]. These mechanisms clearly are important in contributing to the anomalous increase of swimmer velocity with fluid viscosity. However, they are limited in being concerned only with particular combinations of microswimmer and fluid, without attempting to explain the phenomenon in general. Another restrictive feature of these proposed mechanisms is their dependence on the non-Newtonian aspect of the fluid, and the implicit suggestion that it is essential for the phenomenon to occur.

With the help of our swimmer model, we are able to present evidence which contradicts this bit of established wisdom in the field. Specifically, our model shows that the increase in speed of microswimmers with the fluid viscosity occurs even in simple Newtonian fluids and is a consequence of the nature of microswimming itself, not necessarily of the structure of the fluid.

We show that there exist in general two viscosity regimes for mechanical microswimmers, in one of which the swimmer gets slower (which we call the 'conventional' regime) and in the other one faster (the 'aberrant' regime) when the viscosity of the surrounding fluid is increased. The conventional regime is easy to understand–for infinitely viscous fluid the motion must cease, therefore the high viscosity limit must lie in this regime. To understand the origin of the aberrant regime, one must consider the conflicting effects that viscous drag has on a mechanically-driven swimmer. Larger drag retards the motion by providing greater resistance to the swimmer as it moves through the fluid. At the same time, it also promotes the swimming by increasing the hydrodynamic interaction amongst the different motile elements of the swimmer. For high and low fluid viscosities, respectively, the motion-opposing and the motion-enhancing effects of the drag force dominate, leading consequently to the conventional and the aberrant regimes.

The springs in our model turn out to be important for the aberrant regime to be visible. This suggests that an elastic degree of freedom is essential for microswim-

mers to exhibit the aberrant behavior. Moreover, the stroke and hence the velocity must be small enough for the Reynolds number to be negligible (compared to 1) even at the small viscosities at which the aberrant regime is observed. Assuming these conditions, an explanation of the earlier-mentioned experiments is thus: the bacteria, driven by elastic shape changes, are in the aberrant regime for viscosity values accessible to the experiments, and increasing the viscosity sufficiently causes them to enter the conventional regime.

Note that the original Golestanian model does not see the velocity-viscosity regimes, since the approach they employ is stroke-based where the effect of the fluid becomes lost. The problem in that case becomes a purely geometric one, with no reference to the viscosity as it is a force parameter whose effect is hidden in the swimming stroke (see Eq. (9) in Golestanian and Ajdari [2008], where the velocity depends purely on the sphere radii, the arm-lengths and their rates of deformation). This recalls a similar non-dependence of the swimming velocity on the viscosity for Taylor's swimming sheet [Taylor, 1951] when the deformation of the sheet is prescribed, as discussed in section 0.2.2.

From Eq. (1.11), it can be seen that the velocity $\mathbf{v}_{\text{force}}$, being a non-monotonic function of the fluid viscosity $\eta$, leads directly to the existence of the conventional and the aberrant velocity-viscosity regimes. We study these regimes by changing only the viscosity $\eta$ and keeping all the other independent parameters in the problem fixed, including the driving forces. An alternative approach would be to vary the driving forces such that the efficiency of the compared swimmers is held constant. While this may be more relevant biologically, fixing the driving forces is easier, and the results for constant efficiencies would not differ in essence since the efficiencies of fast swimmers are generally higher than those of slow ones [Pande and Smith, 2015, Pickl *et al.*, 2012].

For the swimmer, when $(A - B)/\sin\alpha > 0$, then the velocity $\mathbf{v}_{\text{force}}$ as a function of $\eta$ has exactly one extremum (left panel in Fig. 3.3a), which divides the conventional regime, obtained for large viscosities and shown in white, and the aberrant regime, obtained for small viscosities and shown in green (light gray in grayscale print). The different curves correspond to increasing values of $A$, with $B$ held constant. For each curve, the swimmer lies in the conventional regime if

$$\eta > \frac{1}{2\sqrt{5 + 2\sqrt{13}}} \frac{k}{\pi\omega\lambda}. \tag{3.2}$$

The parameters in the factor on the right can be for convenience combined into a parameter $\psi$ which we define as
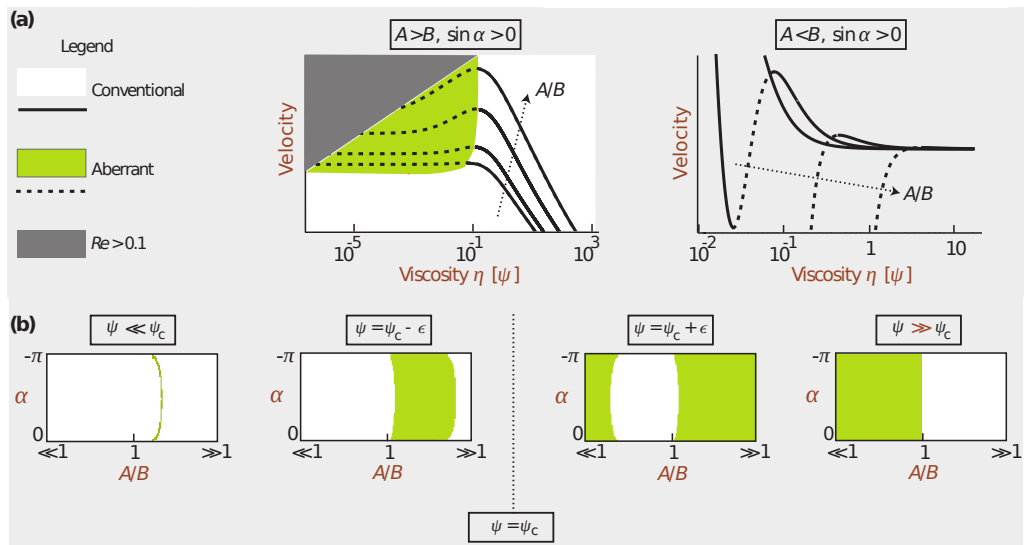
$$\psi = \frac{k}{\pi\omega\lambda} \tag{3.3}$$

Figure 3.3: (a) Velocity vs. viscosity curves with $\sin\alpha > 0$ and different force amplitude ratios ($A/B > 1$ in the left panel and $A/B < 1$ in the right panel). The values of the different parameters have been kept physically appropriate for microswimming. (b) Phase diagrams for different values of the forcing parameters $\alpha$, $A$ and $B$. The parameter $\psi$ is varied between the different plots while $\eta$ is kept fixed. Note that the phase diagrams do not depend on the particular value of $\eta$ used since the $\eta$ values where the velocity has extrema are proportional to $\psi$, meaning that the same phase diagrams are obtained if one changes the values of $\eta$ and $\psi$ by the same factors. Figure taken from publication **P2** [Pande *et al.*, 2016b].

and which we call the swimmer's 'elastic parameter' in order to distinguish it from the spring constant. The point of defining it is that firstly, it has dimensions of viscosity and thus acts as a natural scale to which the fluid viscosity can be compared as in Eq. (3.2), and secondly, this parameter turns out to be important in determining whether the swimmer's motion is in the conventional or the aberrant regime. Moreover, later in chapter 4 when we analyse closely the velocity of swimmers with deformable beads, essentially the same parameter will decide if the bead deformability aids or hinders the swimming.

The dark gray area marks the region where the swimmer Reynolds number $Re = |\mathbf{v}|l\rho/\eta$ becomes large enough for the assumption of Stokes flow to be violated. For strong enough forcing, the entire curve that is not within this dark region is in the conventional regime. This is because strong forcing results in sufficient agitation of the fluid for hydrodynamic interaction amongst the beads to be significant, and increasing the viscosity mainly increases the resistance to motion. In contrast, for weak forcing, the hydrodynamic interaction amongst the beads is weak and increasing the viscosity promotes this interaction. Hence the aberrant and the conventional regimes occur for low and high viscosities, respectively.

If $(A - B)/\sin\alpha < 0$, then the velocity can have several local extrema (right panel in Fig. 3.3a). If the force parameters satisfy the condition $B > A(1 + 6\sin^2\alpha + 2\sin\alpha\sqrt{3 + 9\sin^2\alpha})^{1/2}$, then a swimmer with a fixed elastic parameter becomes aberrant for an intermediate range of viscosities (dashed parts of curves in the right panel of Fig. 3.3a).

We find that it is the elasticity of a swimmer, quantified by the elastic parameter $\psi$, that controls the regime in which it lies. In Fig. 3.3b, we fix the viscosity $\eta$ and mark the conventional and the aberrant behaviour for different values of the driving force parameters $A$, $B$ and $\alpha$, and for increasing values of $\psi$, which are achieved by making the springs stiffer. At small $\psi$ values, the conventional regime is dominant (leftmost panel in Fig. 3.3b). For zero elasticity, in fact, the whole phase space is conventional, as is easily seen by putting $\psi = 0$ in Eq. 1.14. As the elastic parameter increases, the relative area of the aberrant regime too rises continuously (center left panel in Fig. 3.3b) as long as the inequality (3.2) is satisfied. At the critical value $\psi_c = 2\sqrt{5 + 2\sqrt{13}}\eta$, there is a discontinuous change in the nature of the regimes across most of the phase space, with the aberrant regime becoming dominant (center right panel in Fig. 3.3b). As $\psi$ increases further, the aberrant regime again decreases in area, until, in the limit of large $\psi$, the whole phase space becomes equally populated by the two regimes (rightmost panel in Fig. 3.3b). The dependence of the two regimes on $\psi$ reinforces the conclusion that it is the relative extent of the interaction between the motile elements of the swimmer which decides the regime of motion.
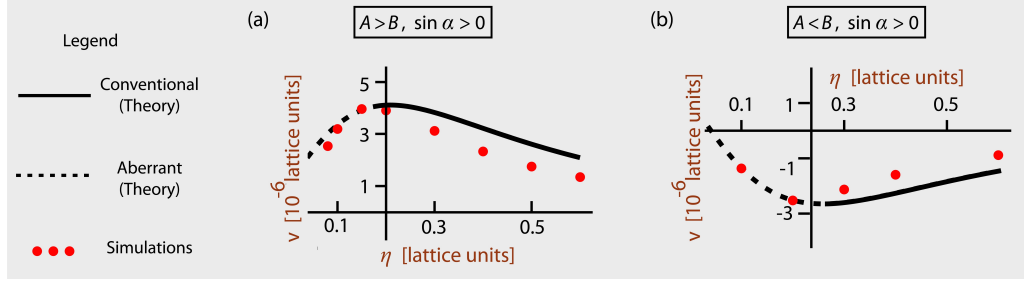
Figure 3.4: Comparison of velocity vs. viscosity curves from theory (solid curves) and simulations (red points), with $\sin \alpha > 0$ and (a) $A/B = 20$, and (b) $A/B = 0.04$. Figure taken from publication **P2** [Pande *et al.*, 2016b].

## Comparison with simulations

To confirm the existence of the two viscosity-dependent regimes that the theory predicts, we compare the theory to results obtained from simulations using the LB3D code (section 2.2.2). In these simulations the beads are identical rigid spheres of radius $5\Delta x$, where $\Delta x$ is the resolution of the lattice-Boltzmann fluid, and their surface is represented by 720 immersed boundary points. The equilibrium center-to-center distance between the spheres is $l = 36\Delta x$. The simulations are run for 30 cycles to let the undesired transients decay, with the period of each cycle being 5000 time steps. The elastic parameter is kept at $\psi = 1.621$ in lattice units. The system size is $200 \times 80 \times 78 \ \Delta x^3$ and periodic boundaries are employed.

We run two sets of simulations, to account for both the cases of $(A - B)/\sin \alpha \gtrless 0$. For this we fix $\alpha = \pi/2$, and the ratio $A/B$ of the driving force amplitudes in the two sets is kept at 20 and 0.04. These driving forces on each bead are distributed evenly across all of its immersed surface points, and are always kept small enough so that the resulting Reynolds number is smaller than 0.1 to ensure 'low *Re*' swimming [Pooley and Yeomans, 2008].

Figs. 3.4(a) and 3.4(b) show the average swimmer velocity $\mathbf{v}_{\text{force}}$ in the steady state as a function of the tested viscosity values $\eta$, for the two force amplitude ratios. In both the investigated cases we observe that the two predicted velocity-viscosity regimes are reproduced well (within experimental error). The fact that our swimmer's motion stems from nothing more than the regular oscillation of two elastic degrees of freedom, namely the two springs, means that the conclusions can be extended to other swimmers whose motion depends on the regular beating of components for which an elasticity may be defined, including both artificial swimmers as well as the flagellar and ciliary ones for which the aberrant regime was first observed.

# *4*

# Swimming with passive deformations

Apart from the direct influence of the fluid viscosity as investigated in the last chapter, the drag force on a swimmer depends on the sequence of shapes which it adopts while undergoing each swimming cycle. This sequence of shapes may be assumed either by some appendages on the body, such as cilia and flagella (see section 0.2.1 in the introductory chapter), or by the main swimmer body itself if it happens to be deformable.

In this chapter we employ our swimmer model in the service of studying the effect of *passive* shape changes of the main swimmer body on the velocity of propagation. While in the literature *active* deformations, by which we mean deformations of shape which drive the motion of the swimmer, have been investigated in some detail [Avron *et al.*, 2005, Ohta and Ohkuma, 2009, Hiraiwa *et al.*, 2011, Farutin *et al.*, 2013, Wu *et al.*, 2015], the use of passive deformations, which are the changes in shape of the swimmer's body as a response to the flow around it, is still unclear. Examples of swimmers with active and passive deformations of the main swimmer body are, respectively, those undergoing amoeboid and euglenoid (or metaboly) movement. As mentioned in section 0.2.1, both the mechanism and the purpose of metaboly are still unclear, and indeed it may not be a fully passive process. Nevertheless, our investigation into the effect of passive shape changes provides some insight into it. In our swimmer, these shape changes emerge when the beads are made deformable, a case for which we have in section 1.2.3 determined the velocity of the swimmer. We now combine this theoretical calculation with simulations of deformable bead swimmers using the LB3D code, as it is capable of simulating deformable membranes. The main result that we shall describe is that passive deformations can both promote and oppose the swimming, depending on the spring stiffness, the counterpart of which in a general mechanical microswimmer is the main elastic mechanism driving the motion.

## 4.1 Effect of body deformability*

We use the LB3D code (described in section 2.2.2) to run simulations of swimmers where we successively change the stiffness moduli of the beads. In these simulations, we elect to restrain the total volume of the beads but not their total area, setting the volume modulus $k_i^V$ and the area modulus $k_i^A$ (from section 2.2.2) to 1 and 0, respectively. The bending modulus $k_i^B$ turns out not to affect the simulation results much, due to the initial spherical shapes of the beads and the fact that they do not undergo very strong deformations. Specifically, we find that changing $k_i^B$ by 5 orders of magnitude changes the swimming velocity by less than 1 per cent. Accordingly, in all the simulations discussed in this section, we keep the value of the bending modulus fixed at $k_i^B = 10^{-3}$. In the different simulation sets, therefore, only the shear moduli $k_i^S$ and the area moduli $k_i^\alpha$ are changed, but always under the condition that $k_i^S = k_i^\alpha$ ($i = 1, 2, 3$), thereby ensuring that a bead membrane responds equally strongly to both deformation and dilation. For different beads in a swimmer, these two stiffness moduli may be different. In all the results discussed in this section, we refer only to a variation in $k_i^S$ in the simulations; that in $k_i^\alpha$ is implied.

The beads contain fluid which has the same density and viscosity as the external fluid. In the simulations, the kinematic viscosity $\nu$ of the fluids is kept at 0.2 in lattice units, which keeps the lattice-Boltzmann relaxation parameter $\tau$ at a value of 1.1 since the two quantities are related by the equation $\nu = (2\tau - 1)/6$. This value of $\tau$ is ideal since it is known in the literature that $\tau \simeq 1$ is good for both accuracy and efficiency of combined LBM-IBM simulations [Krüger *et al.*, 2011], and from Fig. 3.4 in section 3.3 we know that keeping $\nu = 0.2$ (implying $\tau = 1.1$) results in highly accurate swimmer simulations compared to theory when the beads of the swimmer are rigid.

The simulations show that decreasing the shear modulus $k_i^S$ (*i.e.* increasing the deformability) of the beads can both increase and decrease the swimming velocity, and we identify these two velocity responses with the 'deformability-enhanced' and the 'deformability-hindered' regimes of swimming, respectively. In Fig. 4.1 we present instances of the swimming velocity in both these regimes. The plots in the figure show the swimmer velocities as a function of $k_i^S$ for different driving force parameters, as found from simulations (black dashed-dotted curve) and as predicted by the two theoretical velocities, $\mathbf{v}_{\text{force}}$ for rigid beads (blue solid curve) and $\mathbf{v}_{\text{def}}$ for deformable beads (red dashed curve). In part (a) of Fig. 4.1, the force amplitudes $A$ and $B$ are related as $A = 20B$, and the phase difference between the two is $\alpha = \pi/2$. In this set, the shear moduli of all the beads in the swimmer

---

*This section has been adapted from publication **P3** [Pande *et al.*, 2016a], with changes for consistency.
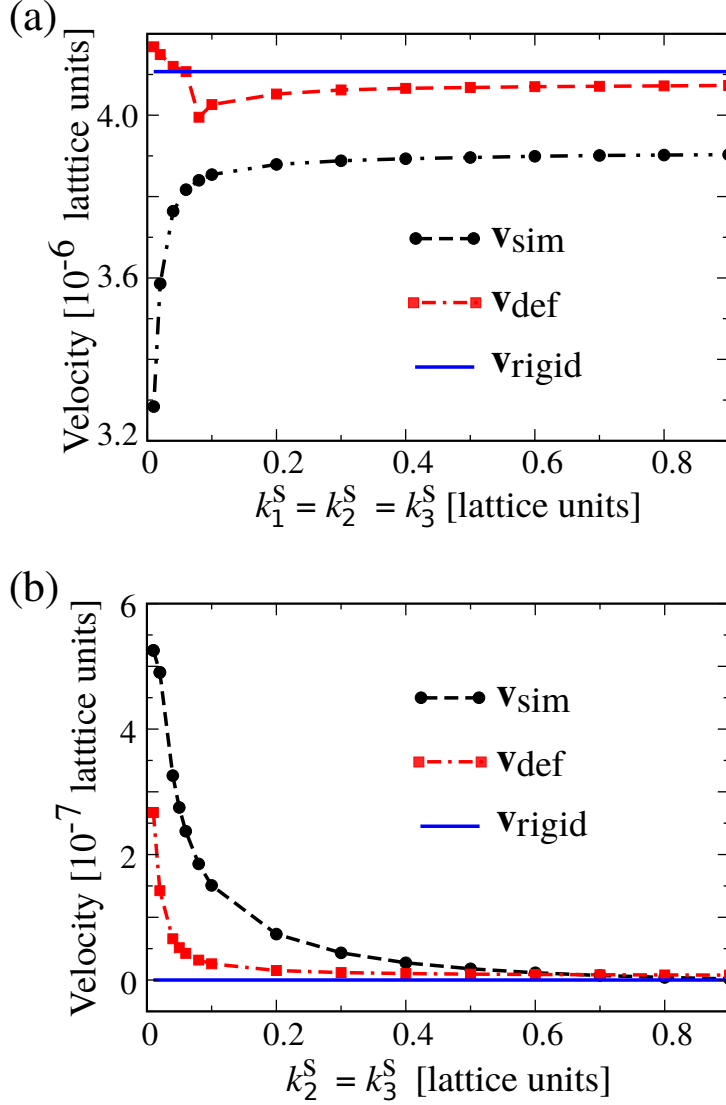
Figure 4.1: Comparison of swimmer velocity found from simulations and theoretical velocity expressions assuming rigid and deformable beads, for changing shear moduli $k_i^{\mathrm{S}}$ of the beads. In (a), the $k_i^{\mathrm{S}}$ values of all the beads are changed together, and the force ratio and the force phase difference respectively are $A/B = 20$ and $\alpha = \pi/2$. In (b), $k_1^{\mathrm{S}}$ is held constant at 1 while the $k_i^{\mathrm{S}}$ values for $i = 2, 3$ are changed together, and the force ratio and the force phase difference are respectively $A/B = 1$ and $\alpha = 0$. Note that the forcing is symmetric in (b), meaning that in the case of rigid beads ($k_2^{\mathrm{S}} = k_3^{\mathrm{S}} \gtrsim 0.8$) there is no swimming. Figure taken from publication **P3** [Pande *et al.*, 2016a].

are changed together and are always equal ($k_i^S = k_j^S \; \forall \; i, j$). It is seen that in the simulations the swimming velocity goes down when $k_i^S$ decreases. In part (b) of Fig. 4.1, the force amplitudes $A$ and $B$ are kept equal, and the phase difference between the two is 0. This is thus a case of symmetric driving, which for rigid beads results in no net swimming. To obtain swimming, we let one bead in the swimmer remain rigid ($k_1^S = 1.0$), while the shear moduli of the other two beads are varied together ($k_2^S = k_3^S$). In this case, as expected, the swimming velocity increases as $k_i^S (i = 2, 3)$ decreases. This is therefore a stark demonstration of the great advantage that body deformations, even when entirely passive, can present for swimming.

There are two important points to be made here. Firstly, the velocity expression $\mathbf{v}_{\text{def}}$ (from Eq. (1.41)) depends on a knowledge of the time-variation of the reduced friction coefficients $\lambda_i(t)$ (Eq. (1.36)), which is not available before the simulations are run. To find these from the simulations, we observe that for weak bead deformabilities, which are an assumpption in our theory, the initially spherical beads retain a convex shape throughout and can be approximated as ellipsoids. The $\lambda_i(t)$ values used in the above calculation can then be found by fitting the instantaneous shape of each bead in a simulation to a bounding ellipsoid and determining its three semi-axes $a_{\text{ell}}$, $b_{\text{ell}}$ and $c_{\text{ell}}$ by comparing the bead shape with an ellipsoid of the same inertia tensor [Krüger *et al.*, 2011]. Due to the axisymmetry of the problem, at each moment two of the semi-axes in a bead are equal, so that the ellipsoids are always spheroids (*i.e.* ellipsoids of revolution), although these spheroids can change from prolate to oblate and back within a swimming cycle. The effective friction coefficients of the beads at each instant are then determined using Perrin's formulas [Perrin, 1934, Pande and Smith, 2015]. As an example, Fig. 4.2 shows the three semi-axes $a_{\text{ell}}(t)$, $b_{\text{ell}}(t)$ and $c_{\text{ell}}(t)$ and the resulting effective friction coefficient $\lambda_1(t)$ (in solid blue) of one of the beads in a simulation from the set presented in Fig. 4.1 (a).

Secondly, we have in the above theoretical curves implicitly assumed that the hydrodynamics is not directly affected by the variation in the shapes of the bead surfaces, since our calculations in section 1.2.3 for the deformable bead swimmer and in section 1.2.1 for the rigid bead swimmer differed only in the time-varying nature of the effective friction coefficients $\lambda_i(t)$ in the former. The theory is therefore meaningful only if the shape variations are tiny, and *a posteriori* we find that this requires the shear moduli $k_i^S$ to be larger than about 0.1. In particular, for all the simulation sets analysed both the deformability-enhanced and deformability-hindered trends in swimming are accurately captured by the theory for $k_i^S > 0.1$ (and in the case of the set in Fig. 4.1 (b), for $k_2^S = k_3^S > 0.01$). It may be noted however that in all our calculations, the effects due to the deformability are only a small correction to the rigid bead swimming case, which is why the $\mathbf{v}_{\text{force}}$ and $\mathbf{v}_{\text{def}}$
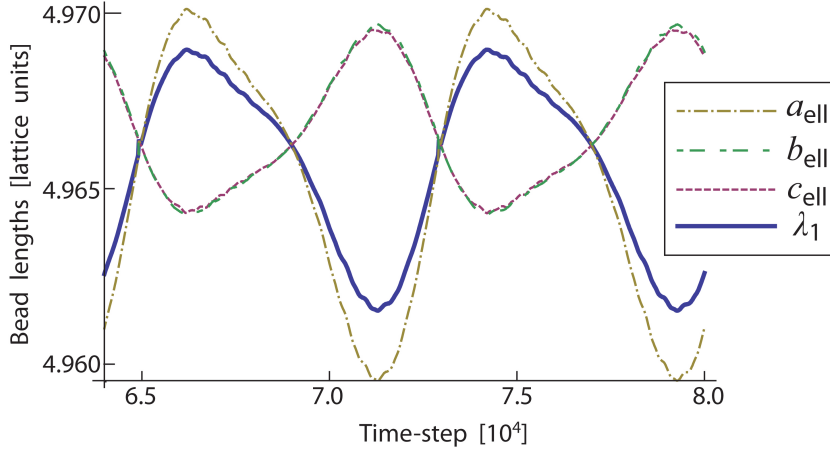
Figure 4.2: Different semi-axes of the bounding ellipsoid of bead 1, and the resultant effective friction coefficient $\lambda_1$, for a simulation with $k_1^S = k_2^S = k_3^S = 0.1$, $A/B = 20$ and $\alpha = \pi/2$. Figure taken from publication **P3** [Pande *et al.*, 2016a].

curves are close together in both the parts of Fig. 4.1.

## 4.2  Phase diagram for the effect of deformability[†]

The above comparison with simulations speaks to the accuracy of our theory in predicting the deformability-enhanced and the deformability-hindered regimes of motion of the swimmer, and we can now use the theory to find these regimes for parameters which are inaccessible to the simulations. It is simplest to identify these two regimes for the special case of identical beads deforming identically, *i.e.* with $a_i = a$ and $b_i^1 = b$, for $i = 1, 2, 3$. In this case, we slightly modify the definition of the elastic parameter $\psi$ of Eq. (3.3) to

$$\psi = \frac{k}{\pi \omega a},\tag{4.1}$$

where the rigid bead effective friction coefficient $\lambda$ (which equals the radius for a sphere) in Eq. (3.3) has been replaced by $a$, its mean value. In section 3.3 we showed that for a swimmer with rigid beads $\psi$ dictated the response of the swimming motion to an increase in the fluid viscosity. We find that (with the above modification in its definition) $\psi$ also determines the deformability-based regime in which the swimming occurs for a swimmer with deformable beads.

---

[†]This section has been adapted from publication **P3** [Pande *et al.*, 2016a], with changes for consistency.
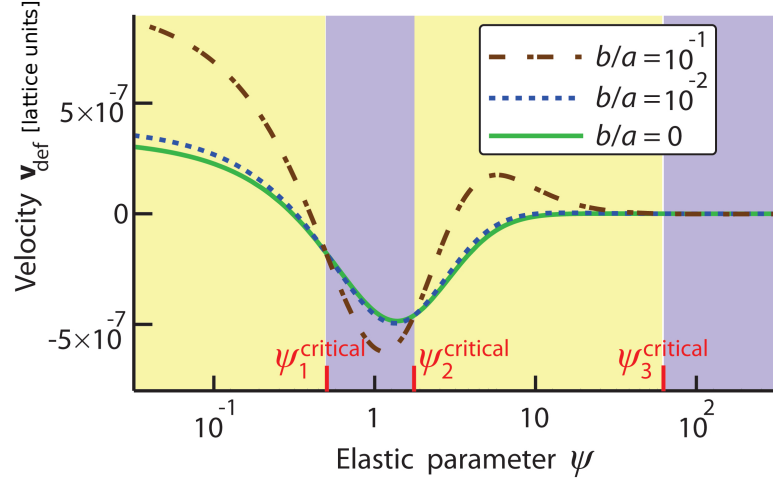
Figure 4.3: Velocity vs. effective elastic parameter for swimmers with deformable beads. The light yellow and violet colours mark the deformability-enhanced and deformability-hindered regions, respectively. The solid green curve is for a swimmer with rigid beads. Figure taken from publication **P3** [Pande *et al.*, 2016a].

In fact we find that there are up to three critical values of $\psi$, which we denote as $\psi_i^{\text{critical}}$ ($i = 1, 2, 3$), that separate regions where $d\mathbf{v}_{\text{def}}/db > 0$ and $d\mathbf{v}_{\text{def}}/db < 0$, inequalities which define the two deformability-based regimes. (Another way to write these inequalities is as $\sum_{i=1}^{3} \mathbf{m}_i \gtrless 0$, from Eq. (1.41).) Fig. 4.3 shows a case in which all three $\psi_i^{\text{critical}}$ values are physically relevant, *i.e.* they are real and positive. In the figure the yellow and the violet regions mark the 'deformability-hindered' and the 'deformability-enhanced' regions, respectively. Knowledge of $\psi$, therefore, is sufficient to determine how the swimmer velocity would change with a change in the bead deformability. The explicit expressions for $\psi_i^{\text{critical}}$ are not noted down here explicitly on account of their great length.

In Fig. 5.3 we present phase diagrams showing the relative population of the deformability-enhanced and -hindered regimes for different driving force amplitude ratios $A/B$ and phase shifts $\alpha$, for a few values of the swimmer elastic parameter $\psi$. In each diagram, all the simulation parameters apart from $A/B$ and $\alpha$ are kept constant. The diagrams show that for small values of $\psi$, the swimmer becomes slower with increasing bead deformability for a majority of the phase space. As the $\psi$ value increases, the swimmer becomes more likely to benefit from an increase in the bead deformabilities. This increase in the prevalence of the deformability-enhanced regime with rising $\psi$ can be understood when one considers that in the limit of infinite $\psi$, which corresponds to perfectly stiff springs, a swimmer with rigid beads cannot swim as it is just one contiguous, rigid body. In this case deformable beads are necessary to gain the requisite degrees of mechan-
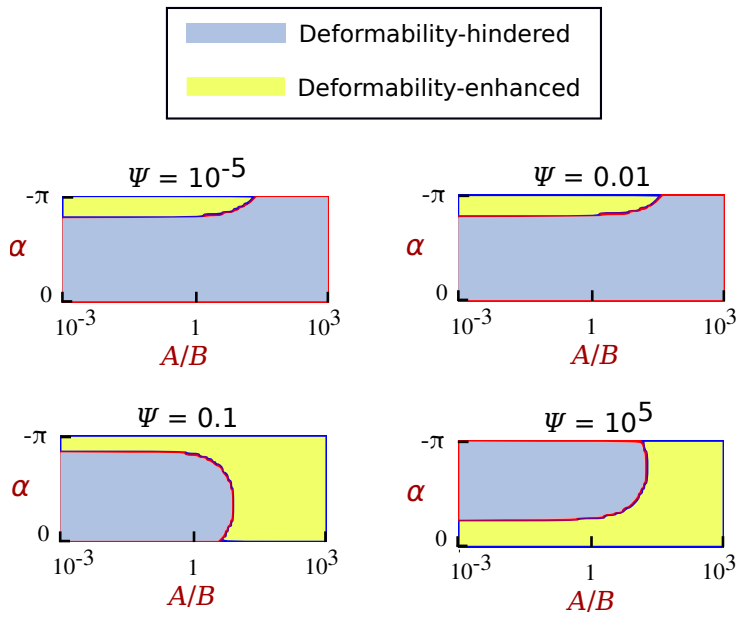
Figure 4.4: Phase diagrams for swimmers with deformable beads, for different values of the forcing parameters $\alpha$, $A$ and $B$, and with increasing values of the elastic parameter $\psi$. Figure taken from publication **P3** [Pande *et al.*, 2016a].

ical freedom which may lead to motion.

In our swimmer model, the elasticity parameter $\psi$ is just the scaled spring constant. From a broader perspective, this parameter measures the strength of the deformations of the entire swimmer that drive its motion, and for a general swimmer, the role of this parameter would be assumed by any other measure of the swimmer's elastic degree of freedom. Our analysis above would then suggest that the response of the body deformability on the swimming motion is controlled by the strength of a mechanical microswimmer's main elastic degree of freedom.

<div style="text-align: right">*5*</div>

# Effect of swimmer shape

In the last chapter we studied the effect of body deformations which occur in the swimmer due to the influence of the fluid and continuously cause the drag force faced by the swimmer to be modified. In this chapter we consider more permanent interactions between the swimmer shape and the fluid drag force, by comparing different mean body shapes for otherwise equal swimmers. In particular we wish to determine the optimal shapes for the three beads in our swimmer, given some constraints, which result in the fastest/most efficient motion. As may be expected in the world of microswimming, we find that the effect of the shape-induced drag can be capricious, leading to results such as the same beads forming the fastest *or* the slowest swimmer in a family, depending on the spring constant.
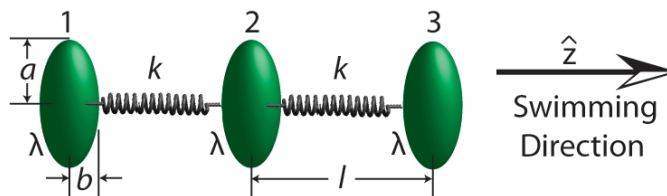


Figure 5.1: A bead-spring swimmer with identical rigid ellipsoidal beads, whose semi-axes are *a* and *b*. Figure taken from publication **P1** [Pande and Smith, 2015].

## 5.1 Ellipsoidal families of swimmers [*]

We constrain the three beads in the swimmer to be rigid, identical and ellipsoidal in shape, with the ellipsoid aspect ratio providing a simple parameter that may be varied to obtain different shapes. These ellipsoids are taken to be spheroids, i.e. formed by revolving an ellipse of semi-axes $a$ and $b$ around $a$, with the aspect ratio $e = a/b$ and their major axis either parallel or perpendicular to the springs (Fig. 5.1). (The semi-axis labels $a$ and $b$ are of course different from the parameters $a_i$ and $b_i^n$ for deformable beads introduced in Eq. (1.36). Since we are here only considering rigid beads, no confusion should arise.) We consider prolate ($e \geq 1$) and oblate ($e \leq 1$) ellipsoids separately, and require the ellipsoids within one family to have either a constant volume or a constant surface area. This last requirement allows us to make a meaningful comparison amongst similar shapes. It also anticipates one of the foreseen applications of bead-spring swimmers, which is their use as payload-carrying sites in future micro-carriers, where depending on whether the payload were placed on the surface of the beads or in their interior, they would be required to have a given volume or surface area. We therefore obtain four families of ellipsoids in the swimmers, namely prolates and oblates of a constant volume $V$ and a constant surface area $S$ (Table 5.1). For convenience, we introduce a radius $r_0$ such that $V = (4/3)\pi r_0^3$ and $S = 4\pi r_0^2$.

### Friction coefficients of ellipsoidal beads under constraints

General expressions for the friction coefficients of ellipsoids of revolution are available in the literature [Oberbeck, 1876, Perrin, 1934], from which we determine the reduced friction coefficients $\lambda$ for the above four families (Table 5.1). For three of these families–namely prolates of a constant volume and a constant surface area and oblates of a constant volume–the smallest reduced friction coefficient $\lambda_{\min}$ is attained for an ellipsoid oriented parallel to the direction of motion and with an aspect ratio close to one (Fig. 5.2(a) and Table 5.2). In the thin body limit ($e \to \infty$ for prolates and $e \to 0$ for oblates), $\lambda$ diverges as some body dimension becomes infinite. In contrast, for oblates of a constant surface area, both the smallest and the largest values of $\lambda$ are attained in the thin body limits ($e \to 0$), depending on the ellipsoid orientation (Fig. 5.2(c) and Table 5.2). This is because the limiting shape in this case is a finite two-sided circular disc with the area of each side being $S/2$, where $S = 4\pi r_0^2$ is the constant surface area. It is easy to

---

[*]All the sections in this chapter have been adapted from publication **P1** [Pande and Smith, 2015], with changes for consistency.

Table 5.1: The reduced friction coefficients $\lambda$ of prolate and oblate ellipsoids in different orientations and under constant volume or constant surface area constraints, in terms of the ellipsoidal aspect ratio $e$. $V$ and $S$ denote the volume and the surface area, respectively, of a sphere of radius $r_0$.

| Ellipsoid | Pre-factor $P$ | $\lambda_{\text{constant } V}$ | $\lambda_{\text{constant } S}$ |
|---|---|---|---|
|  | $\dfrac{(4/3)\left(e^2-1\right)}{\frac{\left(2e^2-1\right)}{\sqrt{e^2-1}}\log\left(e+\sqrt{e^2-1}\right)-e}$ | $P\times\dfrac{r_0}{e^{1/3}}$ | $P\times\dfrac{\sqrt{2}r_0}{\sqrt{1+\frac{e^2}{\sqrt{1-e^2}}\tanh^{-1}\left(\sqrt{1-e^2}\right)}}$ |
|  | $\dfrac{(8/3)\left(e^2-1\right)}{\frac{\left(2e^2-3\right)}{\sqrt{e^2-1}}\log\left(e+\sqrt{e^2-1}\right)+e}$ | $P\times\dfrac{r_0}{e^{1/3}}$ | $P\times\dfrac{\sqrt{2}r_0}{\sqrt{1+\frac{e^2}{\sqrt{1-e^2}}\tanh^{-1}\left(\sqrt{1-e^2}\right)}}$ |
|  | $\dfrac{(8/3)\left(1-e^2\right)}{\frac{\left(3-2e^2\right)}{\sqrt{1-e^2}}\tan^{-1}\left(\frac{\sqrt{1-e^2}}{e}\right)-e}$ | $P\times\dfrac{r_0}{e^{1/3}}$ | $P\times\dfrac{\sqrt{2}r_0}{\sqrt{1+\frac{e^2}{\sqrt{e^2-1}}\sin^{-1}\left(\frac{\sqrt{e^2-1}}{e}\right)}}$ |
|  | $\dfrac{(4/3)\left(1-e^2\right)}{\frac{\left(1-2e^2\right)}{\sqrt{1-e^2}}\tan^{-1}\left(\frac{\sqrt{1-e^2}}{e}\right)+e}$ | $P\times\dfrac{r_0}{e^{1/3}}$ | $P\times\dfrac{\sqrt{2}r_0}{\sqrt{1+\frac{e^2}{\sqrt{e^2-1}}\sin^{-1}\left(\frac{\sqrt{e^2-1}}{e}\right)}}$ |

Table 5.2: Critical values of $e_{\min}$ and their respective $\lambda_{\min}$, for prolate and oblate ellipsoids subject to a constant total volume ($V$) or surface area ($S$) constraint

| Shape | Constant volume $(V = (4/3)\pi r_0^3)$ | | Constant surface area $(S = 4\pi r_0^2)$ | |
|---|---|---|---|---|
| | $e_{\min}$ | $\lambda_{\min}$ | $e_{\min}$ | $\lambda_{\min}$ |
|  | 1.95 | $0.95r_0$ | 4.04 | $0.89r_0$ |
|  | 0.70 | $0.99r_0$ | 0.00 | $0.80r_0$ |

show that in this case the friction coefficients have boundary extrema given by

$$\lambda_{\min} = \frac{16\sqrt{2}r_0}{9\pi} \quad \text{(for } e \to 0\text{), and}$$

$$\lambda_{\max} = \frac{8\sqrt{2}r_0}{3\pi} \quad \text{(for } e \to \infty\text{).} \tag{5.1}$$

## 5.2 Optimisation of bead shape

For the above families, to determine the effect of bead shape upon the swimming, we analyse the equation

$$\frac{d\,|\mathbf{v}_{\text{force}}|}{de} = 0 = \frac{d\,|\mathbf{v}_{\text{force}}|}{d\lambda}\frac{d\lambda}{de}. \tag{5.2}$$

Using the chain rule, we have broken up the relation for the velocity extrema into

$$d\lambda/de = 0, \tag{5.3}$$

and

$$d\,|\mathbf{v}_{\text{force}}|\,/d\lambda = 0. \tag{5.4}$$

Looking at these two relations separately is instructive. Eq. (5.3) yields the aspect ratio $e_{\min}$ of the ellipsoid with the smallest reduced friction coefficient $\lambda_{\min}$ as determined earlier (Table 5.1). Since this condition relates only to the geometry of the beads and not to the forces acting on the swimmer, the velocity curve always has an extremum $\mathbf{v}_{\lambda_{\min}}$ at the aspect ratio $e_{\min}$. This value $\mathbf{v}_{\lambda_{\min}}$ is given by Eq. (1.14), with $\lambda$ replaced by $\lambda_{\min}$ for the appropriate case (Table 5.1).

In the following analysis, it turns out to be convenient to define a 'reduced spring constant' $\kappa$ of the swimmer, as

$$\kappa = \psi\lambda/\eta = k/(\pi\omega\eta), \tag{5.5}$$

where $\psi$ is the elastic parameter of the swimmer defined in Eq. (3.3). The advantage of defining $\kappa$ stems from the requirement in this analysis to preserve the effect of the shape, whose signature is carried by $\lambda$, explicitly in the velocity formulae. (This is the same reason why defining $\psi$ was useful when considering the effect of the fluid viscosity.) Despite the sobriquet 'reduced', $\kappa$ is not dimensionless but has the dimensions of length, and provides a scale to which the reduced friction coefficient, which too has the dimensions of length, may be compared. We find that the smallest reduced friction coefficient $\lambda_{\min}$ defines a global critical value $\kappa_c$
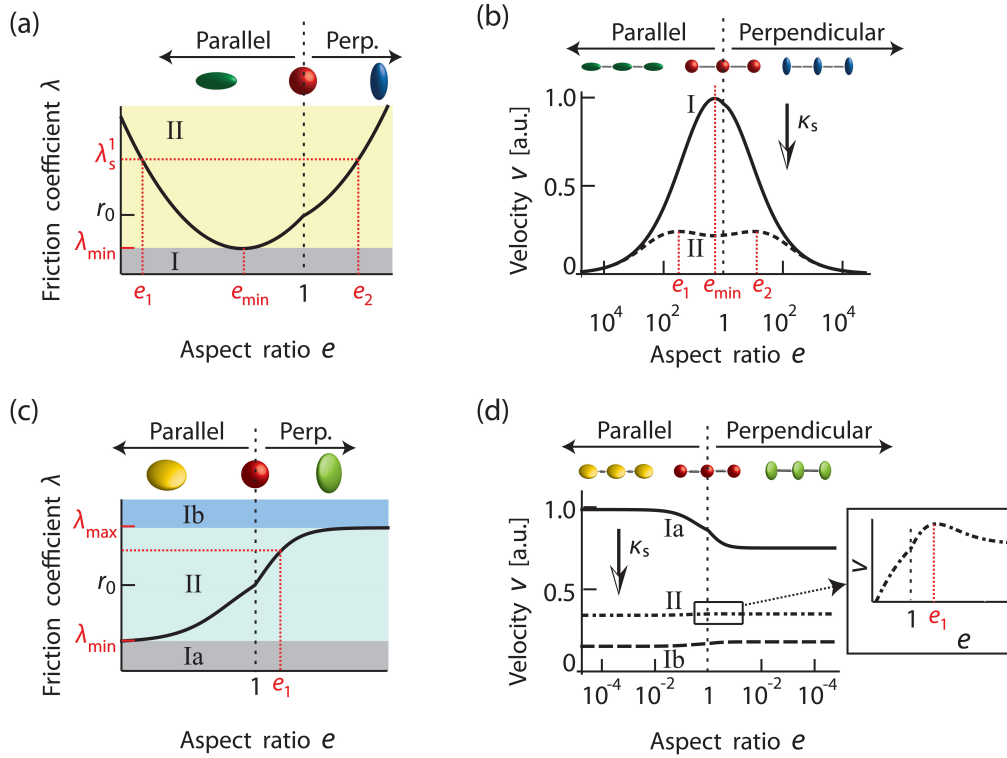
Figure 5.2: (a) Reduced friction coefficient $\lambda$ for prolate ellipsoids of a constant volume or surface area and oblate ellipsoids of a constant volume. (b) The corresponding velocity $\mathbf{v}_{\text{force}}$ curves, for either $A = B$ or $\alpha = \pi/2$ if $A \geq B$ (or $\alpha = -\pi/2$ if $A < B$). (c) $\lambda$ for oblate ellipsoids of a constant surface area. (d) The corresponding velocity $\mathbf{v}_{\text{force}}$ curves, for either $A = B$ or $\alpha = \pi/2$ if $A \geq B$ (or $\alpha = -\pi/2$ if $A < B$). In (a) and (b), 'I' and 'II' denote the drag-dominated and the interaction-dominated regimes, respectively, while in (c) and (d), 'Ia' and 'Ib' denote the drag-dominated regime and 'II' denotes the interaction-dominated one. Figure taken from publication **P1** [Pande and Smith, 2015].

of the reduced spring constant, given by

$$\kappa_{\mathrm{c}} = 2\sqrt{3}\lambda_{\min}. \tag{5.6}$$

As we shall see, depending on whether the reduced spring constant of the swimmer is larger or smaller than this critical value, the extremum $\mathbf{v}_{\lambda_{\min}}$ in the velocity-aspect ratio curve may be a maximum or a minimum.

Eq. (5.4) allows us to connect the optimal shapes to the different forces acting on the beads, since its solutions relate the reduced friction coefficient to the reduced spring constant, the driving frequency and the fluid viscosity. Let the springs in the swimmer have a reduced spring constant given by

$$\kappa = \kappa_{\mathrm{s}}. \tag{5.7}$$

Then, there is a shape with the reduced friction coefficient given by

$$\lambda_{\mathrm{s}}^{1} = \kappa_{\mathrm{s}} / (2\sqrt{3}), \tag{5.8}$$

such that $\lambda_{\mathrm{s}}^{1}$ is a solution to Eq. (5.4). This leads to the velocity extremum

$$\mathbf{v}_{\lambda_{\mathrm{s}}^{1}} = \frac{7\left(2\sqrt{3}AB\sin\alpha + A^2 - B^2\right)}{768\,\pi^2\eta^2 l^2\omega\kappa_{\mathrm{s}}}\hat{\mathbf{z}}. \tag{5.9}$$

If $\lambda_{\mathrm{s}}^{1}$ is the only solution to Eq. (5.4), then one can show (see the Appendix in section 5.5) that if $\kappa_{\mathrm{s}} < \kappa_{\mathrm{c}}$, the magnitude of the velocity has only one maximum obtained from the geometric condition which determines the most streamlined shape (solid curve, labelled 'I', in Fig. 5.2 (b)). We call this regime 'drag-dominated', as here the velocity is maximised upon minimising the drag. On the other hand, if $\kappa_{\mathrm{s}} > \kappa_{\mathrm{c}}$, then the velocity curve has two more extrema (one in the case of oblates of a constant surface area), which are degenerate and are attained for the ellipsoids whose reduced friction coefficient equals $\lambda_{\mathrm{s}}^{1}$ (dashed curve, labelled 'II', in Fig. 5.2(b)). In this case, the magnitude of these latter velocity extrema is globally the maximum. We label this regime as 'interaction-dominated', as here the velocity is maximised at an intermediate value of the drag, where the hydrodynamic interaction between the beads becomes important. In this regime, in fact, one sees the highly counter-intuitive effect of the most streamlined shape forming locally the *slowest* swimmer (as the dashed curve in Fig. 5.2(b) has a local minimum at $e_{\min}$).

The fact that these two regimes exist can be attributed to the two conflicting effects that drag has upon a swimmer: while on one hand it resists motion through the fluid, on the other hand it promotes the fluid's agitation, resulting in
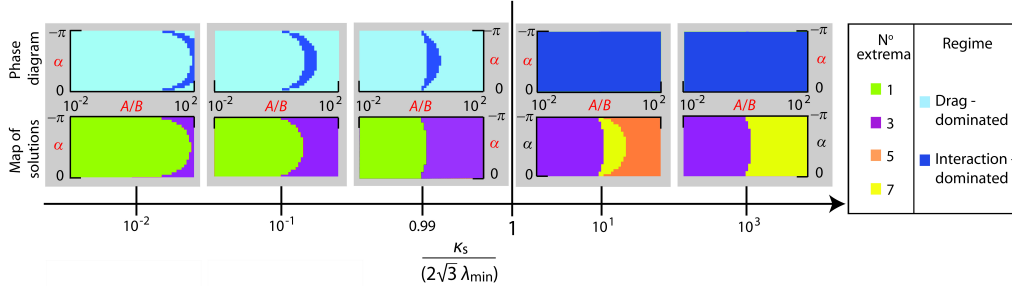
Figure 5.3: Phase diagrams and solution maps for the forcing parameters $A/B$ vs $\alpha$, for particular values of $\kappa_s$. If $\kappa_s/\lambda_{\min} < 2\sqrt{3}$, then for some parameters we have $\mathbf{v}_{\max} = \mathbf{v}_{\lambda_{\min}}$ (*i.e.* the drag-dominated regime), and if $\kappa_s/\lambda_{\min} > 2\sqrt{3}$ the whole phase space is interaction-dominated. Figure taken from publication **P1** [Pande and Smith, 2015].

hydrodynamic interaction among the beads and ultimately in swimming. In the interaction-dominated regime, where the spring constant (and consequently $\kappa_s$) is relatively high, most of the input work is consumed in deforming the springs, and so an increased drag is beneficial for a heightened hydrodynamic interaction among the bodies. Therefore, the swimmer with ellipsoids of a reduced friction coefficient $\lambda_{\min}$, which agitates the fluid the least, is locally the slowest. In contrast, in the drag-dominated regime, where the spring constant is low, most of the input work is transferred directly onto the agitation of the fluid, so having a high drag only slows the swimmer down.

## 5.3    Phase diagram for effect of shape

More generally, Eq. (5.4) can have several solutions for $\lambda$ depending on the force parameters $A$, $B$ and $\alpha$. Then the velocity–seen as a function of the ellipsoid's aspect ratio $e$ and its orientation–can have upto seven extrema (see the Appendix in section 5.5 for details). In this case, too, we can identify the drag-dominated and the interaction-dominated regimes, as the regimes respectively where the highest velocity magnitude is attained for the most stream-lined bead shapes and for the bead shapes where a higher drag causes a sufficiently positive hydrodynamic interaction to lead to an increase in the velocity. Fig. 5.3 shows phase diagrams identifying these two regimes (top graph in each panel), and solution maps showing the number of velocity extrema (bottom graph), as a function of the driving parameters and for different values of the reduced spring constant $\kappa_s$. Since the velocity magnitude is unchanged under the transformation $\{A \leftrightarrow B, \alpha \to -\alpha\}$, we restrict these diagrams to $-\pi \leq \alpha \leq 0$.
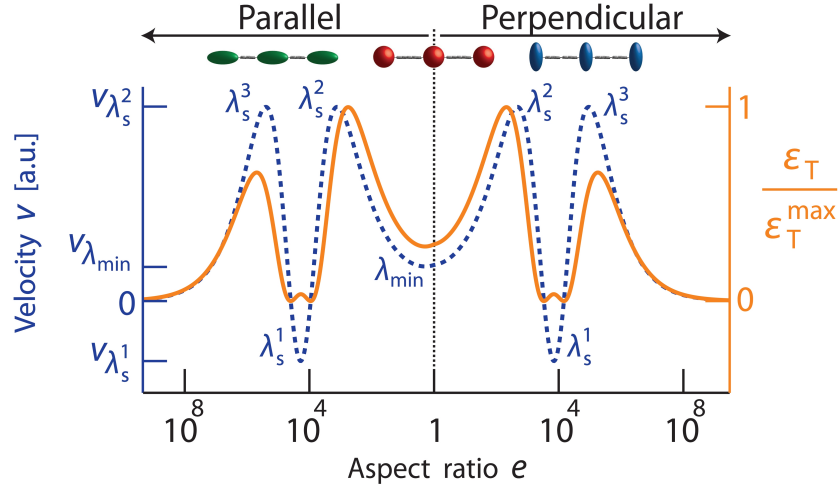
96



Figure 5.4: Velocity $\mathbf{v}_{\text{force}}$ (dashed blue curve) and transport efficiency $\epsilon_T$ (solid orange curve) of constant-volume prolate swimmers, with $B = 3A$ and $\alpha = \pi/4$. The $\lambda_v$ written near each velocity extremum ($\lambda_v = \lambda_s^i$ or $\lambda_{\min}$) specifies that the respective extremum is attained at $\lambda = \lambda_v$. For the definition of $\lambda_s^2$ and $\lambda_s^3$ and the corresponding velocity extrema, please see the Appendix in section 5.5. Figure taken from publication **P1** [Pande and Smith, 2015].

These diagrams show that, in general, as the reduced spring stiffness $\kappa_s$ increases, the swimmer goes from the drag-dominated regime to the interaction-dominated one. In particular, for $\kappa_s = 0$, the swimmer is always in the drag dominated regime (light blue in the phase diagrams), irrespective of the other parameters. There is only one velocity extremum (light green in the solution maps), at $\lambda = \lambda_{\min}$. As $\kappa_s$ increases, two more extrema, associated with $\lambda_s^2$ (see the Appendix in section 5.5), appear in the velocity curve for some values of the driving parameters (shown by purple in the solution maps), and parts of the corresponding phase diagrams enter the interaction-dominated regime (indicated by dark blue). This holds true as long as $\kappa_s < \kappa_c$. As soon as $\kappa_s$ becomes larger, upto four extrema, associated with $\lambda_s^1$ and $\lambda_s^3$ (see the Appendix in section 5.5), appear in the velocity-shape curve (shown by yellow and orange in the solution maps) depending on the force parameters, and the whole phase diagram enters the interaction-dominated regime.

## 5.4 Transport efficiency

To quantify the ability of swimmers to carry cargo, we define the transport efficiency $\epsilon_T$ as the ratio of the reduced transport energy $|\mathbf{v}_{\text{force}}|^2$ and the input power

$\frac{1}{T} \int_0^T \Sigma_{j=1}^3 \mathbf{F}_j(t) \cdot \mathbf{v}_j(t) \mathrm{d}t$, giving

$$\epsilon_\mathrm{T} = \left| \mathbf{v}_\mathrm{force} \frac{AB\left(\kappa_\mathrm{s}^2 + 12\lambda^2\right)\sin\alpha - 2\left(B^2 - A^2\right)\kappa_\mathrm{s}\lambda}{\left(A^2 + B^2\right)\left(\kappa_\mathrm{s}^2 + 12\lambda^2\right) - AB\left(\kappa_\mathrm{s}^2 - 12\lambda^2\right)\cos\alpha} \right|.$$

This definition favours fast swimmers, but penalises ones which require a high power input. It is also bounded as a function of $\omega$, $\kappa_\mathrm{s}$ and $\lambda$, thus ensuring that it does not diverge on, for example, increasing the time period. It is more suitable than the simple ratio of the current (which is proportional to $\mathbf{v}_\mathrm{force}$) to the input work (as in Felderhof [2006]), which is insensitive to changes in shape for fixed driving in the far-field approximation. Also, the Lighthill efficiency [Lighthill, 1952] is unsuitable because it penalises swimmers facing a high drag, and this is inapt for the interaction-dominated swimming regime.

In spite of the natural correlation between the transport velocity and efficiency, the most efficient swimmer is not necessarily the fastest one (Fig. 5.4). This is particularly important in the interaction dominated regime, where designs which propagate with the same speed can have significantly different efficiencies due to a different repartition of the input work on the fluid and the compression of the springs. For instance, in Fig. 5.4, $\epsilon_\mathrm{T}$ at $\lambda_\mathrm{s}^3$ is much less than at $\lambda_\mathrm{s}^2$, although $\mathbf{v}_{\lambda_\mathrm{s}^2} = \mathbf{v}_{\lambda_\mathrm{s}^3}$. In contrast, in the drag-dominated regime, the input work consumed by the elastic components is negligible, and so optimally-shaped swimmers are typically the most efficient.

## 5.5 Appendix[†]

Here we show the calculation of the critical value $\kappa_\mathrm{c}$ of the reduced spring constant and of the general extrema in the velocity–aspect ratio curve (which also takes the ellipsoid orientation into account, as in Fig. 5.2). First we consider the three special cases of (i) $A = B$, (ii) $\alpha = \pi/2$ with $A > B$, and (iii) $\alpha = -\pi/2$ with $A < B$. For these cases, it can be easily shown that $\lambda_\mathrm{s}^1$ (Eq. (5.8)) is the only solution to Eq. (5.4). Therefore, if the springs are so soft that $\kappa_\mathrm{s} < 2\sqrt{3}\lambda_\mathrm{min}$, then there can be no ellipsoid with the reduced friction coefficient radius $\lambda_\mathrm{s}^1$, since in that case $\lambda_\mathrm{s}^1 = \kappa_\mathrm{s}/(2\sqrt{3})$ would be smaller than $\lambda_\mathrm{min}$, which is impossible. On the other hand, if the springs are stiff enough so that $\kappa_\mathrm{s} > 2\sqrt{3}\lambda_\mathrm{min}$, then–for prolate ellipsoids of a constant volume, as in Fig. 5.2(a)–exactly two ellipsoids have the

---

[†]A much more detailed exposition of the number of velocity extrema and the corresponding velocity values for the different regions in the phase diagram of Fig. 5.3 is provided for the interested reader at the end of the thesis in Appendix A1. It is not essential for following the arguments in this chapter.

reduced friction coefficient $\lambda_s^1$ (with aspect ratios given by $e_1$ and $e_2$ in regime II, Fig. 5.2(a)). Therefore, $\kappa_c = 2\sqrt{3}\lambda_{min}$ acts as a critical value of $\kappa$.

The above discussion is identical for prolates of a constant surface area and for oblates of a constant volume. The case of oblates of a constant surface area is slightly different, since $e_{min} = 0$ and $\lambda_{max}$ is finite. In this case, if the springs are too soft, *i.e.* with $\kappa_s < 2\sqrt{3}\lambda_{min}$ or too stiff, with $\kappa_s > 2\sqrt{3}\lambda_{max}$, then there is no ellipsoid with the reduced friction coefficient $\lambda_s^1$. Moreover, since $e_{min}$ equals 0, the velocity curves are monotonic functions of the aspect ratio $e$. For soft springs, this function decreases with $e$ (regime Ia in Fig. 5.2), while for stiff springs it increases (regime Ib). If, however, the spring stiffness is intermediate, *i.e.* $2\sqrt{3}\lambda_{min} < \kappa_s < 2\sqrt{3}\lambda_{max}$, then there is one velocity maximum obtained from the condition in Eq. (5.4).

For a general choice of parameters, Eq. (5.4) provides two further pairs of solutions, namely $\{\lambda_s^2, \lambda_s^3\}$ (when the relation between the force amplitudes is $B < A$), and $\{\lambda_s^4, \lambda_s^5\}$ (when $A < B$). These solutions can be ordered as $\lambda_s^2 < \lambda_s^1 < \lambda_s^3$ and $\lambda_s^4 < \lambda_s^1 < \lambda_s^5$. A solution $\lambda_s^i$ of Eq. (5.4) for the reduced drag coefficient is physically relevant only if $\lambda_s^i \in \mathbb{R}$ and $\lambda_s^i \geq \lambda_{min}$. Each such physically relevant solution $\lambda_s^i$ provides two degenerate velocity extrema $\mathbf{v}_{\lambda_s^i}$. Furthermore, the degeneracy extends over the solution pairs, with $\mathbf{v}_{\lambda_s^2} = \mathbf{v}_{\lambda_s^3}$ and $\mathbf{v}_{\lambda_s^4} = \mathbf{v}_{\lambda_s^5}$. These extrema values are given by

$$|\mathbf{v}_{\lambda_s^i}| = \frac{7\left(F_>^2 - F_<^2 - \sqrt{F_>^4 + F_<^4 - 2F_>^2 F_<^2 \cos(2\alpha)}\right)}{384\,\pi^2\eta^2 l^2 \omega \kappa_s}, \qquad (5.10)$$

where $i = 2, ..., 5$ and $F_>$ and $F_<$ denote the larger and the smaller of the force amplitudes $A$ and $B$, respectively. Consequently, the velocity $\mathbf{v}_{force}$ as a function of the aspect ratio $e$ has, in addition to one extremum from $\lambda_{min}$, up to 3 pairs of extrema from $\lambda_s^i$.

# 6

# Effect of inertia on swimming

In this final part of the thesis, we consider the motion of microswimmers beyond the bounds of the Stokes regime, *i.e.* when effects of inertia are no longer negligible. As discussed in section 0.1, the assumption of Stokes flow simplifies the swimming problem a lot, as the inconvenient non-linear and time-dependent terms in the Navier-Stokes equation (Eq. (0.1)) disappear. This assumption results unavoidably in some non-physical effects, such as a direct proportionality of the swimming speed to the applied force and an instantaneous response of the fluid, up till infinity, to any disturbance within it. These effects can usually be ignored, firstly in the interest of the linearity of the resulting Stokes equation which is quite evidently crucial for analytic treatments of the swimming problem, and secondly because these effects turn out not to cause significant errors in the flow description. All of our calculations presented so far have been rooted in the linearity of the Stokes equation.

Inclusion of the inertial contributions to the flow is a very daunting task in general. To bring it within the realm of tractability, we restrict our attention to the lowest order effects of inertia on our swimmer. In other words, we study the swimming regime where inertial or non-Stokesian effects first emerge and impart quantitative, and possibly qualitative, differences to the motion when compared to that in purely Stokes flow. Our approach will be to follow as closely as possible our methods described thus far in this thesis, and modify them appropriately to take inertia into account. We will do this in two ways. Firstly, we will provide a heuristic scheme for identifying the non-Stokesian regime of motion by considering the relaxation of a swimmer from an initially stably-moving configuration. In the Stokesian approximation, this relaxation is instantaneous, and the degree of non-instantaneity in it will speak to the non-Stokesian aspect of the motion. We will show that the larger the mass of the swimmer, the slower does it have to be for the relaxation to display an inertial component. Secondly, we will perform a

full calculation of the swimming velocity of our bead spring swimmer model with non-negligible inertia, by including a mass acceleration term in the equations of motion governing the swimming. This shall confirm the finding that for larger swimmer masses the inertial or the non-Stokes regime begins at smaller swimming speeds (*i.e.* smaller driving forces). In both cases the theoretical predictions will be supported by LBM simulations.

## 6.1 Relaxation of inertial swimmers *

We wish to observe and identify non-inertial effects in our swimmer's motion by considering its relaxation in the fluid when all forces on it cease. For this purpose, we make the beads in the swimmer much heavier than the surrounding fluid, and let the swimming motion be much faster, with the expectation that both these contributions aid in violating the assumptions of Stokes flow. We therefore run simulations of swimmers with spherical beads using the waLBerla-*pe* framework, where the radius of each sphere is $6\Delta x$ and the rest length of each arm is $32\Delta x$. The cycle period is kept at 8000 time steps to aid simulation accuracy. The phase shift $\alpha$ is set to $0.5\pi$.

The simulations are run in four sets, with the mass of each sphere in the four sets being 20000, 30000, 40000 and 50000 lattice units, respectively. Note that these masses imply that the sphere densities are about 22 to 55 times larger than the density of the surrounding fluid, respectively, in the four sets, meaning that the beads are not neutrally buoyant. This is not a problem since gravity plays no role in our simulations.

Within each simulation set we increase the driving force amplitudes successively and check first the swimming veolcity of the swimmer in the steady state, and then its relaxation to zero velocity when the driving forces are suddenly switched off. The range of driving force amplitudes checked is slightly different in the different sets, because (as we shall show) the critical force amplitude values where non-inertial effects first become visible depend on the swimmer's mass. The force ranges chosen in each simulation set are those at which the Stokes regime, the non-Stokes regime, and an intermediate regime each become visible.

We find that for all the simulation sets, the Stokesian theory of section 1.2.1 gives the correct swimmer velocities in the steady state only for low driving force amplitudes, and diverges from the simulations as the forces increase. In each case, the velocities found from the simulations are higher than those predicted by the theory. As an example, Fig. 6.1 shows the velocity curves from the Stokesian theory and the simulations for a sphere mass of 40000 lattice units. This matches the expectation of a continuous transition from the Stokes regime to the non-Stokes

*This section has been adapted from publication **P4** [Pande* *et al.*, 2016], with changes for
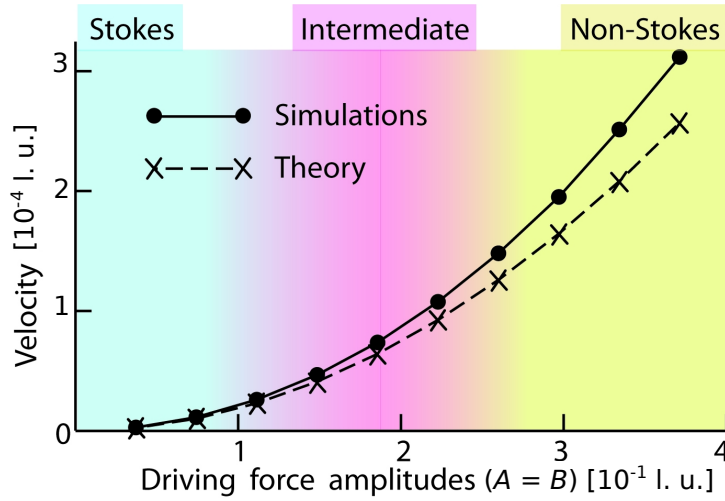
Figure 6.1: Velocity of a swimmer with inertia for different force amplitudes, from simulations and theory. Figure taken from publication **P4** [Pande* *et al.*, 2016].

one, which we have loosely marked as blue and yellow regions respectively in Fig. 6.1. In between lies an intermediate regime, marked in pink in Fig. 6.1, where the transition occurs. We now locate this transition more precisely.

## 6.1.1 Underdamped relaxation of the swimmer

Our bead-spring swimmer can be viewed as a system of connected harmonic oscillators, which are coupled through both the middle sphere and the surrounding fluid, as well as damped by the fluid. Since the drag force is dominant in Stokes flow, we postulate that the Stokes and the non-Stokes regimes are characterised by overdamping and underdamping, respectively, in the motion of this oscillator system. For an underdamped driven harmonic oscillator, the trajectory is given by

$$x(t) = x_0 e^{-\gamma t} \cos\left(\omega_r t - \alpha_r\right), \tag{6.1}$$

where $x_0$ is the maximum amplitude, $\gamma$ is the damping constant, and $\omega_r$ and $\alpha_r$ are constants of oscillation. For underdamped motion of a coupled system such as ours, and of any mechanical microswimmer in general, it is difficult to specify the different parameters in Eq. (6.1), yet the damping coefficient $\gamma$ may still be identified. To do this, consider the swimmer's relaxation from an initially steady state when the driving forces are switched off. In the steady state, the swimmer faces the Stokes drag force $F_{St} = -6\pi\eta r_{eff} u$ where $r_{eff}$ is its effective hydrodynamic
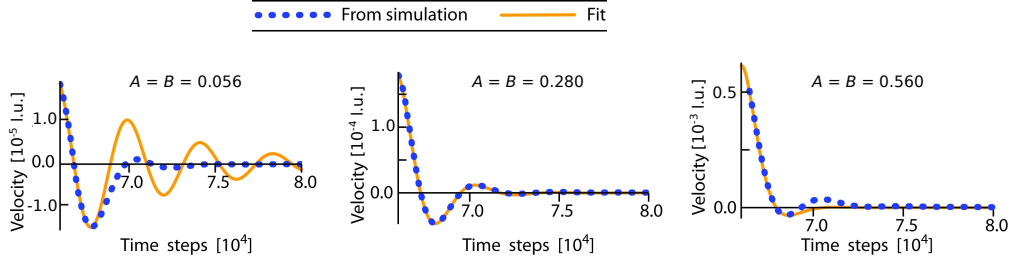
consistency.

Figure 6.2: Relaxation of a swimmer for different driving force amplitudes. Figure taken from publication **P4** [Pande* *et al.*, 2016].

radius. When the driving forces vanish, then the body stops instantly if inertial effects are discounted, but in the presence of inertia the body exhibits coasting, and its velocity decreases continuously as

$$F_{St} = m\mathrm{d}u/\mathrm{d}t = -6\pi\eta r_{eff}u.$$

$$\Rightarrow u = Ce^{-\gamma t}, \text{ with } \gamma = \frac{6\pi\eta r_{eff}}{m} \text{ and } C \text{ a constant.} \tag{6.2}$$

Due to the use of the Stokes drag force $F_{St}$ in obtaining $\gamma$, Eq. (6.1) with said $\gamma$ describes the relaxation only in the intermediate regime between the Stokes and the non-Stokes ones. Therefore, by fitting the relaxation curve of the swimmer with Eq. (6.1), the intermediate regime can be identified. This can then also be used to determine the swimmer's effective hydrodynamic radius $r_{eff}$, by using Eq. (6.2) to find $r_{eff}$ once $\gamma$ has been identified from the fit to Eq. (6.1). This procedure can be used for other mechanical microswimmers such as in Purcell [1977], Avron *et al.* [2005] which can be viewed as oscillators.

## 6.1.2   Identification of intermediate regime

We now check the relaxation curves obtained from the simulations of our swimmers when the driving forces are turned off after the steady state has been reached. We find that Eq. (6.1) at times underestimates and at times overestimates the damping seen from the simulations. As illustration, Fig. 6.2 shows the relaxation obtained from simulation (blue dotted curve) and the fit to this curve using Eq. (6.1) (orange solid curve) for three different force amplitude values for the simulation set with sphere mass = 40000 lattice units. In each case, the fit parameters are chosen such that they minimise the error to the simulation curve in the initial part of the relaxation, *i.e.* from the initial point on the left to the first local minimum. It may be seen that the middle simulation, with a force amplitude of 0.28 lattice units, shows near-perfect agreement with the theoretically predicted
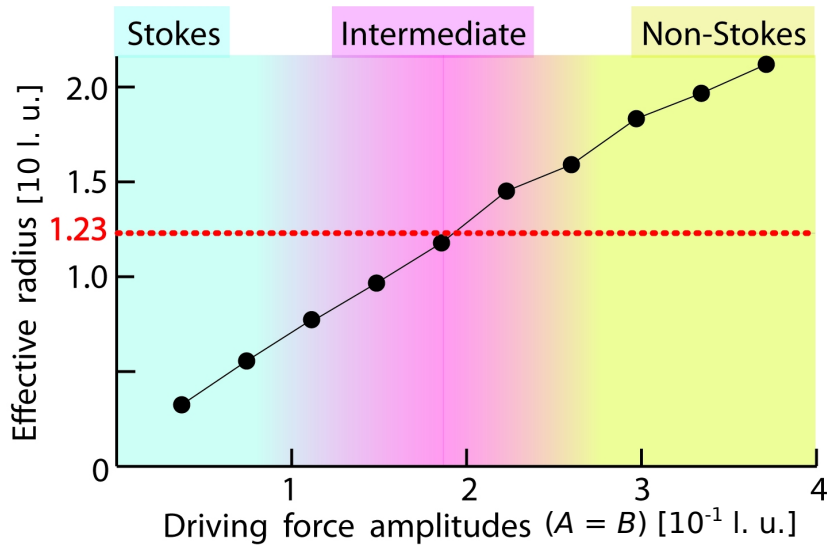
Figure 6.3: Effective radius of a swimmer for different force amplitudes, as determined by relaxation after force cut-off. Only the simulations in the intermedite regime are expected to reproduce the theoretically predicted value of 12.3 lattice units (marked by a dashed red line). Figure taken from publication **P4** [Pande* *et al.*, 2016].

relaxation curve based on Eq. (6.1). In contrast, in the plot on the left, with a force amplitude of 0.056 lattice units, the swimmer's damping is underestimated by the fitting curve, while in the plot on the right with a force amplitude of 0.56 lattice units, the fitting curve from Eq. (6.1) overestimates the damping.

The different extents of agreement between the simulations and the theoretical fitting curves for different force amplitudes are understandable, since the theoretical fit is only expected to work well in the regime which shows characteristics of both Stokesian and non-Stokesian motion (due respectively to Eq. (6.2) which depends on the Stokes drag law and Eq. (6.1) which assumes underdamped motion which is a non-Stokesian effect). This means that the relaxation from the simulation should match the theory the most perfectly in the intermediate regime. Such a reasoning shows the three simulations plotted in Fig.6.2 to lie, from left to right, in the Stokes, intermediate, and non-Stokes regimes, respectively.

There is another way to check such a determination of the three regimes. In chapter 1, section 1.2.4, we found a theoretical expression for the effective radius $r_{\text{eff}}$ of our swimmer. In all the simulations that we are here considering, we have $\lambda_i = 6\Delta x$ and $l_i = 32\Delta x$, which gives a theoretically expected $r_{\text{eff}}$ value of $r_{\text{eff}} = 12.3\Delta x$. The corresponding values for each simulation can be found by combining Eqs. (6.1) and (6.2). Focussing first on the case of sphere mass
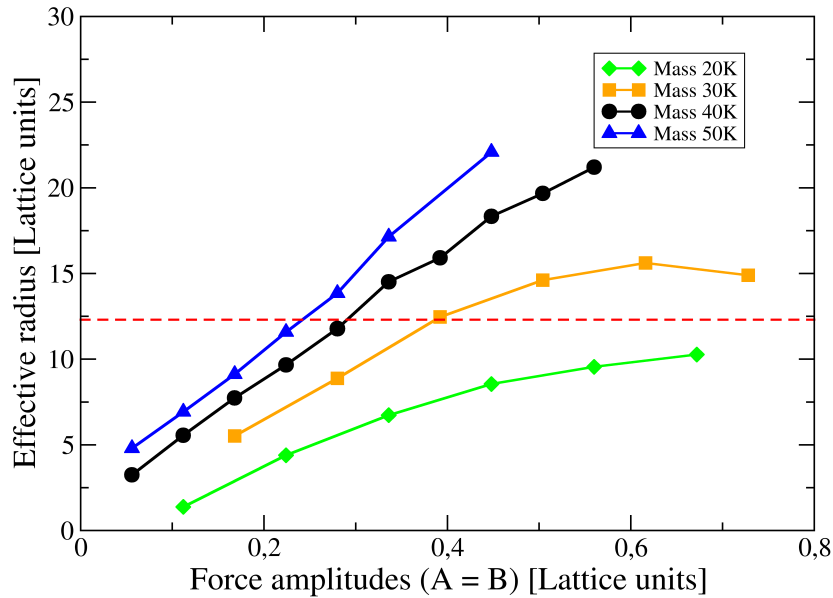
Figure 6.4: Effective radius of a swimmer for different force amplitudes and different mass values, as determined by relaxation after force cut-off. Figure taken from publication **P4** [Pande* *et al.*, 2016].

= 40000, we plot the $r_{\text{eff}}$ value obtained from each simulation in Fig. 6.3, with the black circles. The theoretical value of $12.3\Delta x$ is marked with the horizontal dashed red line. It is clear that there is an excellent agreement between the theoretical and the simulation values, for a force amplitude of 0.28 lattice units, *i.e.* precisely the force amplitude which we identified as marking the intermediate regime on the basis of the accuracy of the underdamped oscillator description of the swimmer's relaxation. In general, the $r_{\text{eff}}$ value found from simulations increases monotonically as the driving forces increase, because the parameter $\gamma$ found from Eqs. (6.1) and (6.2) initially underestimates and then overestimates the actual damping in the simulations. This is a good check of our reasoning to identify the intermediate regime.

We now consider similar curves obtained from all four sets of simulations. Fig. 6.4 shows that in each case, the $r_{\text{eff}}$ values given by the simulations increase monotonically. (The only exceptions to this are the simulations with the very highest force amplitude values probed–see for instance the orange curve for sphere mass = 30000 lattice units–but that is a relic of the spheres almost colliding with each other at these high driving force values.) Moreover, as the sphere mass increases, the curves shift to the left, and so do the respective force ranges marking the intermediate regime. In each case, the simulations where Eq. (6.1) best fits the swimmer relaxation are the same ones where the $r_{\text{eff}}$ curves are closest to the

theoretical value, marked by the horizontal red dashed line in Fig. 6.4. What this means is that as the mass of the swimmer increases, the non-inertial effects, which first make their presence felt in the intermediate regime, become visible at smaller driving force amplitudes, *i.e.* for smaller swimming strokes. This is understandable, since in the Reynolds number it is the product of the velocity and the density which comes together, and increasing either sufficiently breaks the bounds of the Stokes flow assumption. Note that to find the true Reynolds number of a swimmer which is not neutrally buoyant, one should replace the density of the fluid in the definition of the Reynolds number (Eq. (0.4)) by that of the swimmer itself.

# 6.2    Theory for inertial swimming [†]

Having phenomenologically studied in the previous section the motion of our swimmer when inertial effects start becoming visible, we now present a basic theoretical treatment of the situation. The calculations are based on our theory for a swimmer with rigid beads swimming in Stokes flow (section 1.2.1), and non-Stokesian effects are included in the model by adding a mass acceleration term to the governing equations of motion in Eq. (1.9). As we shall show, the theory provides results which are in good agreement with the simulations of the swimmer with non-negligible mass, and also confirms the three regimes and their characteristics discussed in the previous section.

## 6.2.1    Calculation of velocity for a swimmer with inertia

We wish to calculate to the lowest non-negligible order the inertia-induced effect on the motion of our bead-spring swimmer. To begin with, we adopt the same model as in section 1.2.1, with the sinusoidal driving forces specified by Eq. (1.3), and the equation of motion for the $i^{\text{th}}$ bead given by Eq. (1.9). The latter equation can on rearrangement be written as

$$\mathbf{F}_i^{\text{d}}(t) + \mathbf{F}_i^{\text{s}}(t) = \sum_{j=1}^{3} Q_{ij}(t)\mathbf{v}_j(t), \tag{6.3}$$

where $\mathbf{F}_i^{\text{d}}(t)$ and $\mathbf{F}_i^{\text{s}}(t)$ are respectively the driving and the spring force on the $i^{\text{th}}$ bead, and the introduced variables $Q_{ij}(t)$ are functions of the differences $\mathbf{R}_j(t) - \mathbf{R}_k(t)$ $(j,k = 1,2,3)$ of the bead positions. The left hand side in Eq. (6.3) is the

[†]The calculations presented in this section were carried out by Oleg Trosman under the supervision of the author [Trosman, 2016]. Note also that this section has been adapted from publication **P4** [Pande* *et al.*, 2016], with changes for consistency.

sum of the forces on the $i^{\text{th}}$ bead not counting the force applied by the fluid, and in the Stokesian description this sum is exactly balanced by the hydrodynamic force of the fluid which opposes the motion of each bead. This is manifestly not the case in the non-Stokes regime, and we postulate that in the latter regime the effect of the applied forces (the driving and the spring forces) on each bead is to accelerate the bead, in addition to neutralising the opposing force provided by the fluid which is given by the right hand side of Eq. (6.3). In other words,

$$\mathbf{F}_i^{\text{d}}(t) + \mathbf{F}_i^{\text{s}}(t) = \sum_{j=1}^{3} Q_{ij}(t)\mathbf{v}_j^{\text{mass}}(t) + m_i \dot{\mathbf{v}}_i^{\text{mass}}(t), \tag{6.4}$$

where $m_i$ is the mass of the $i^{\text{th}}$ bead and the velocity of the $i^{\text{th}}$ bead is now written as $\mathbf{v}_i^{\text{mass}}(t)$, in order to highlight its mass-dependence.

Since the sum of the driving and the spring forces over the entire swimmer is still zero, the above equation yields

$$\sum_{i=1}^{3}\sum_{j=1}^{3} Q_{ij}(t)\mathbf{v}_j^{\text{mass}}(t) + \sum_{i=1}^{3} m_i \dot{\mathbf{v}}_i^{\text{mass}}(t) = 0. \tag{6.5}$$

Eq. (6.5) represents a set of coupled homogenous ordinary differential equations for the velocities $\mathbf{v}_i^{\text{mass}}(t)$ of the three beads, which can be solved if a suitable form for the deformations of the lengths of the two arms of the swimmer is given, a specification which allows one to treat the coefficients $Q_{ij}(t)$ as known functions of time. It may be noted that this approach is stroke-based, unlike our force-based approach for the Stokes regime case in chapter 1. The form for the armlength deformations that we assume is sinusoidal, given by

$$\mathbf{R}_2(t) - \mathbf{R}_1(t) = L_1(t)\hat{\mathbf{z}} = (l_1 + d_1\cos(\omega t + \delta_1))\,\hat{\mathbf{z}}, \text{ and}$$
$$\mathbf{R}_3(t) - \mathbf{R}_2(t) = L_2(t)\hat{\mathbf{z}} = (l_2 + d_2\cos(\omega t + \delta_2))\,\hat{\mathbf{z}}. \tag{6.6}$$

Here $\omega$ is the frequency of the swimming cycles (which equals the frequency of the driving forces). The above form for the arm length deformations is the same as that adopted by the arms of the swimmer in the non-inertial (Stokesian) case, where it emerges as a response to the sinusoidal driving forces, and also identical to the form assumed in Golestanian and Ajdari [2008] in the stroke-based formulation of the swimmer model in the non-inertial case (Eq. (1.1)). In the inertial case the armlengths may be expected to have a dependence on the masses $m_i$, but comparison with the armlength trajectories obtained in simulations suggests that the functions in Eq. (6.6) describe the armlengths well even in the inertial swimming case if the three beads are identical.

The above equations can be solved fully for unequal masses $m_i$, but here we present the result only for the case $m_i = m$ for the sake of brevity. Using the set of equations (6.6) to specify the coefficients $Q_{ij}(t)$, Eqs. (6.5) can be decoupled to

$$\dot{v}_i^{\text{mass}}(t) + \beta(t)v_i^{\text{mass}}(t) + \gamma_i(t) = 0, \tag{6.7}$$

where $v_i^{\text{mass}}(t)$ denotes the magnitude of $\mathbf{v}_i^{\text{mass}}(t)$, and the coefficients $\beta(t)$ and $\gamma_i(t)$ are given by

$$\beta(t) = \frac{1}{3m} \sum_{i=1}^{3} \sum_{j=1}^{3} Q_{ij}(t), \text{ and} \tag{6.8}$$

$$\begin{bmatrix} \gamma_1(t) \\ \gamma_2(t) \\ \gamma_3(t) \end{bmatrix} = \frac{1}{3m} \begin{bmatrix} \dot{L}_1(t) \sum_{j=1}^{3} Q_{2j}(t) + (\dot{L}_1(t) + \dot{L}_2(t)) \sum_{j=1}^{3} Q_{3j}(t) + m\left(2\ddot{L}_1(t) + \ddot{L}_2(t)\right) \\ -\dot{L}_1(t) \sum_{j=1}^{3} Q_{1j}(t) + \dot{L}_2(t) \sum_{j=1}^{3} Q_{3j}(t) + m\left(-\ddot{L}_1(t) + \ddot{L}_2(t)\right) \\ -(\dot{L}_1(t) + \dot{L}_2(t)) \sum_{j=1}^{3} Q_{1j}(t) - \dot{L}_2(t) \sum_{j=1}^{3} Q_{2j}(t) - m\left(\ddot{L}_1(t) + 2\ddot{L}_2(t)\right) \end{bmatrix}. \tag{6.9}$$

The equations (6.7)-(6.9) are closed by requiring the motion to be periodic in the steady state, *i.e.*

$$v_i^{\text{mass}}(t) = v_i^{\text{mass}}(t + 2\pi/\omega). \tag{6.10}$$

In terms of the velocities of the individual beads, the velocity $\mathbf{v}^{\text{mass}}$ of the whole swimmer is

$$\mathbf{v}^{\text{mass}} = v^{\text{mass}}\hat{\mathbf{z}} = \frac{\omega}{6\pi} \int_0^{2\pi/\omega} \sum_{i=1}^{3} \mathbf{v}_i^{\text{mass}}(t)\mathrm{d}t, \tag{6.11}$$

where the averaging of the bead velocities has been done over the three beads and over one swimming cycle.

Eqs. (6.7)-(6.11) are solved for $\mathbf{v}^{\text{mass}}$ by the integrating factor method, and the final closed-form expression comes out to be

$$v^{\text{mass}} = \frac{\omega}{6\pi} \int_0^{2\pi/\omega} \sum_{i=1}^{3} \frac{1}{I(t)} \left[ -\int_0^t \gamma_i(t')I(t')\mathrm{d}t' + \frac{\frac{1}{I(2\pi/\omega)} - \int_0^{2\pi/\omega} \gamma_i(t')I(t')\mathrm{d}t'}{1 - \frac{1}{I(2\pi/\omega)}} \right] \mathrm{d}t, \tag{6.12}$$

where the function

$$I(t) = \exp\left(\int_0^t \beta(s)\mathrm{d}s\right) \tag{6.13}$$

has been introduced for ease of expression.

## 6.2.2 Comparison with simulations

We check the results of our calculation for the same four sets of simulations (for sphere masses 20000, 30000, 40000 and 50000 on the lattice) discussed in section 6.1. Fig. 6.5 displays the velocity of the swimmer for each mass value as a function of the driving forces. The different velocity curves shown are the one obtained from the simulations (labelled as $\mathbf{v}_{\text{simulation}}$ and marked with orange triangles), the one given by $\mathbf{v}^{\text{mass}}$ using the theory of section 6.2.1 (marked with blue circles), and the one given by $\mathbf{v}_{\text{stroke}}$ in Eq. (1.2) which does not consider the effect of inertia (marked with green squares).

An immediate observation is that the $\mathbf{v}^{\text{mass}}$ curves match much better with the $\mathbf{v}_{\text{simulation}}$ ones than the $\mathbf{v}_{\text{stroke}}$ curves do. The higher the mass the better is the agreement between the $\mathbf{v}_{\text{simulation}}$ curves and the theoretical $\mathbf{v}^{\text{mass}}$ curves. This shows that at least in the parameter ranges that we have explored, our velocity calculation for swimming with inertia works well.

A second result is that the $\mathbf{v}^{\text{mass}}$ curves initially overestimate the simulation velocities and then, beyond some force amplitude value dependent on the mass value, begin to underestimate them. This is most clearly seen in parts (a) and (b) of Fig. 6.5, for masses 20000 and 30000 on the lattice, but is also the case for the other two mass values. To show this more clearly, we plot in Fig. 6.6 the relative errors between the $\mathbf{v}_{\text{simulation}}$ and the $\mathbf{v}^{\text{mass}}$ curves for the different sphere masses as functions of the driving force amplitudes. Here one sees clearly that the relative errors, never very large ($\lesssim 15\%$), are initially negative and then become positive for each mass value except for mass 50000, in which case they are small enough ($< 5\%$) to be within the error bounds of the LBM. Moreover, the errors get progressively smaller as the mass of the spheres increases.

To sum up, the observations above and in section 6.1 lead to the following conclusions:

1. The Stokesian approaches for predicting the swimmer's motion work well for low driving forces (or equivalently, for small swimming strokes).

2. As the driving forces/strokes get large, the swimming begins to diverge from the Stokesian predictions.
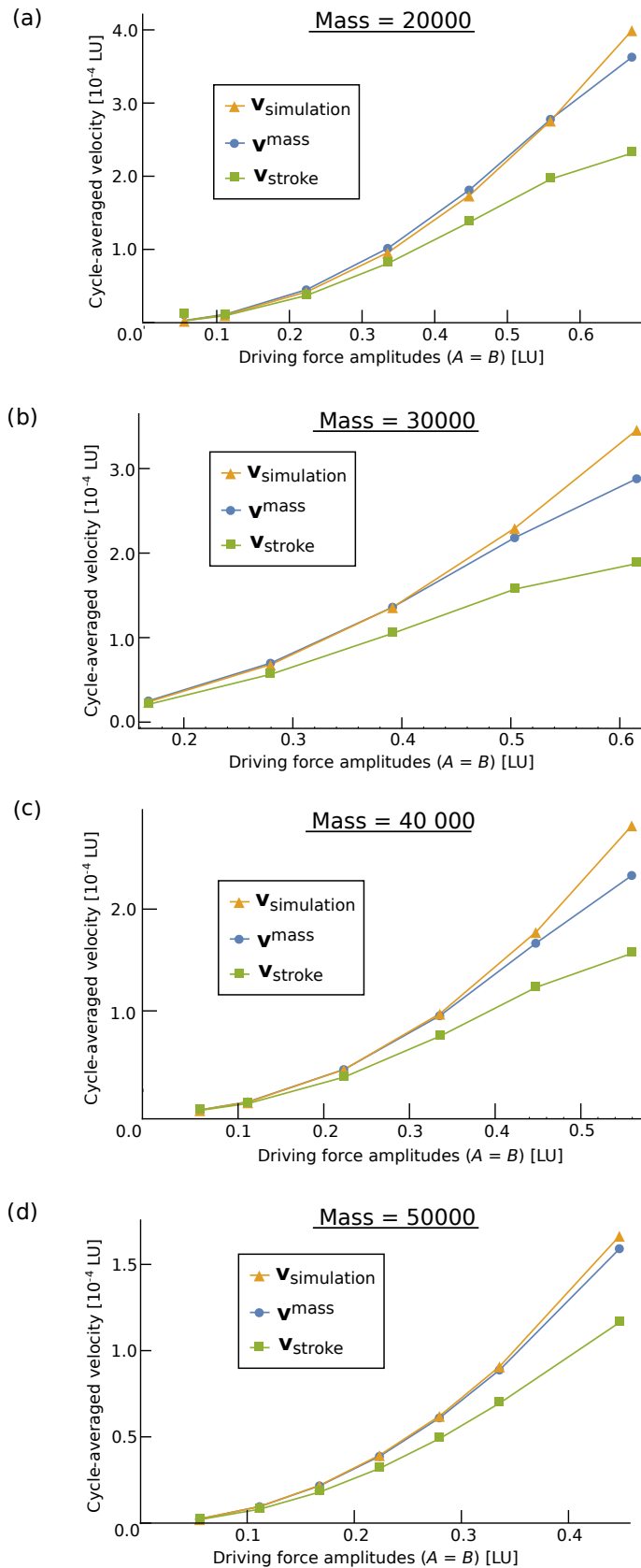
Figure 6.5: Comparison of velocity expressions from simulations ($\mathbf{v}_{\text{simulation}}$) and from theories which do ($\mathbf{v}^{\text{mass}}$) and do not ($\mathbf{v}_{\text{stroke}}$) include the effect of inertia, for different mass values. Figure taken from publication **P4** [Pande* *et al.*, 2016].
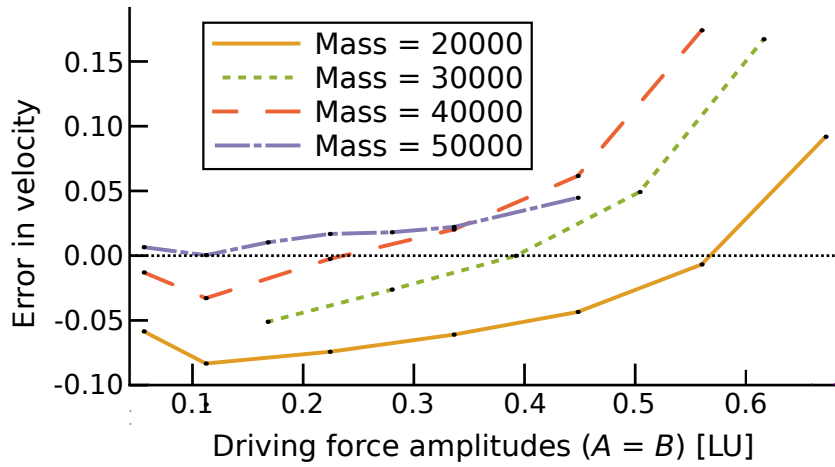
Figure 6.6: Relative error between $\mathbf{v}_{\text{simulation}}$ and $\mathbf{v}^{\text{mass}}$ for different mass values. Figure taken from publication **P4** [Pande* *et al.*, 2016].

3. Combining the Stokesian approach with non-Stokesian elements–such as an underdamped relaxation of the swimmer or a mass acceleration term in the equations of motion–leads to accurate description of the swimmer's motion in a narrow, intermediate regime between the Stokes and non-Stokes regimes. To the left of this regime (in a velocity vs. driving force plot), the combined approach overestimates the swimmer velocity, and to the right of the regime it underestimates the velocity, which is consistent with the identification of the left and right regions as the Stokesian and non-Stokesian regimes, respectively.

4. As the mass of the swimmer increases, the intermediate regime becomes visible at smaller driving forces (or swimming strokes).

It may be observed that there is a small difference between the values of the driving force amplitudes in Figs.6.4 and 6.6 at which, respectively, the $r_{\text{eff}}$ curves equal the theoretical value and the errors between the $\mathbf{v}_{\text{simulation}}$ and $\mathbf{v}^{\text{mass}}$ curves become zero. This is to be expected since the methods of sections 6.1 and 6.2 are quite different, with the one based on the force-free relaxation of the swimmer, and the other on the force-induced swimming. Nevertheless, the fact that both the methods lead to the above listed conclusions points to the validity of the general approach in trying to identify inertial features in the motion.

# 7

# Conclusions and outlook

In this thesis we have endeavoured to explain some fundamental properties of mechanical microswimmers through analytical study and accompanying lattice Boltzmann simulations of the bead-spring swimmer model. We have shown that a force-based study of the swimmer, with its starting point the driving forces acting on the swimmer, enables the identification of some features of motion which are lost in a stroke-based study, such as the specification of the swimmer's pusher or puller nature and the onset of synchronicity in the deformation of the two arms.

In addition, we have discovered a number of interesting influences on microswimming which have before our work gone unknown. For instance, we have explained how microswimmers, moving in low Reynolds number flow, can swim faster in a simple Newtonian fluid when the viscosity of the fluid is increased. This happens when the driving forces are small enough and there is an elastic component to the motion. This provides one possible explanation of many experiments reported in the literature in which some bacteria swim quicker in more viscous fluids.

We have also described the effect that passive shape changes of the swimmer, in response to the fluid flow, can have on the velocity, by assuming the effective radii of the three beads in the swimmer to vary weakly in time. We have shown how a frequency decomposition of the effective radii indicates that only the driving frequency mode contributes to the swimming in the limit of small deformations, and in this limit the swimming velocity may rise or fall with the bead deformability depending on the swimmer's elasticity.

In the same vein, we have studied the effect of the mean swimmer shape by a consideration of ellipsoidal beads of varying aspect ratios in the swimmer. In this case again, a given shape can form the slowest or the quickest swimmer depending on the stiffness of the springs. This is because different spring constants cause different apportioning of the driving energy between the movement of the beads

and the deformation of the springs, and this causes either the reduction in the drag faced by each bead or the hydrodynamic interaction amongst the beads to be the dominant effect enhancing the speed.

In addition to the above results, which were all found for a swimmer in the Stokes regime, we have explored the onset of non-Stokesian inertial effects in microswimming, by combining simulations of increasingly heavier and faster swimmers with a theory which solves the equations of motion after supplementing them with mass acceleration terms which are absent in purely Stokesian flow. We have shown that the results of the theory are in good agreement with those obtained from the simulations, and improve significantly upon the predictions of the non-inertial theory when the driving forces become large. The simulations as well as the theory show that the smooth transition between the Stokes and the non-Stokes regimes is marked by an intermediate regime, where the inertial theory works best, and which can be accurately identified for a general mechanical microswimmer by equating its relaxation with that of an underdamped harmonic oscillator. Another observation we make is that, given two otherwise identical swimmers, the intermediate regime for the heavier swimmer occurs at smaller driving forces (or smaller swimming speeds) than for the lighter one. This happpens because (swimmer) density and velocity appear together in the Reynolds number (which determines the importance of the inertial component to the flow with respect to the viscous component), and increasing either of the two sufficiently causes the inertial component to become significant.

## 7.1 Future directions

While we have been able to use our model to shed light on many known and unknown features of microswimming, a lot more can (and yearns to) be done. Here we suggest some possible extensions of our work.

### 7.1.1 Effect of inertia from first principles

In our investigation of inertial effects on microswimming (chapter 6), our method was stroke-based, since we assumed a sinusoidal form for the variation of the arm lengths with time. Comparison with simulations showed that this assumption was justified for the parameter ranges we explored. This approach nevertheless faces the same limitations as other stroke-based analyses, namely that the effects of the fluid and other force influences are lost. To overcome this, a natural extension of our work would be to employ the force-centric approach that we have adopted for the bead-spring swimmer in the Stokes regime (chapter 1, section 1.2.1) in service of the non-Stokesian swimmer. For this one would again begin with Eq. (6.5)

as the main equations of motion, and instead of using Eqs. (6.6) to specify the swimming stroke, one would assume that the bead positions in the steady state were given by an equation akin to Eq. (1.10), with the different functions no longer sinusoidal but informed by the functional forms of the armlengths obtained from the stroke-based approach in chapter 6. The main difficulty here would be caused by the non-sinusoidal forms of the functions describing the bead positions, and the fact that the system of differential equations in the bead positions would now be of order two. We expect our perturbation-based approach to nevertheless lead to analytical solution in appropriate parameter ranges, and numerically the system would certainly be tractable.

### 7.1.2   Effect of deformability from first principles

Similar to the case with inertia, in our calculation of the way that the swimming speeds are affected by passive deformations in the swimmer, we took recourse to a partly geometry-based method, where the shape deformations were taken from the simulations and gave rise to the variations in the bead effective radii, assumed to be known (section 1.2.3). An extension of our study would be to find the effect of bead deformability from first principles, without needing the input from the simulations. This is a challenging problem since the coupling between the deformable membranes and the fluid–a feedback mechanism wherein the deformation in a membrane and the fluid flow around it both affect each other–has to be fully resolved, a step we evaded by assuming the membrane shapes to be given. In spite of its inherent difficulty, the deformation of flexible capsules and membranes under various kinds of flow has been a highly-researched area of study [Barthès-Biesel, 1980, Li *et al.*, 1988, Chang and Olbricht, 1993, Misbah, 2006, Abkarian *et al.*, 2007], and an approach which may prove particularly fruitful is the decomposition of the membrane deformation into spherical harmonics via a spectral method *à la* [Kessler *et al.*, 2008]. While an analytical solution of the resulting equations would likely be difficult, a numerical solution should be possible, which would enhance the predictive power of the study.

### 7.1.3   Study of deformable cargo carriers

An intriguing and potentially useful extension of our work would lie in combining the above two problems by studying the motion of a swimmer with deformable beads when inertial effects are important. Such a swimmer could be of use in designing vesicular or membranous bead carriers, the fluid inside some of which could act as cargo and possibly be of a significantly different density and viscosity than the surrounding fluid.
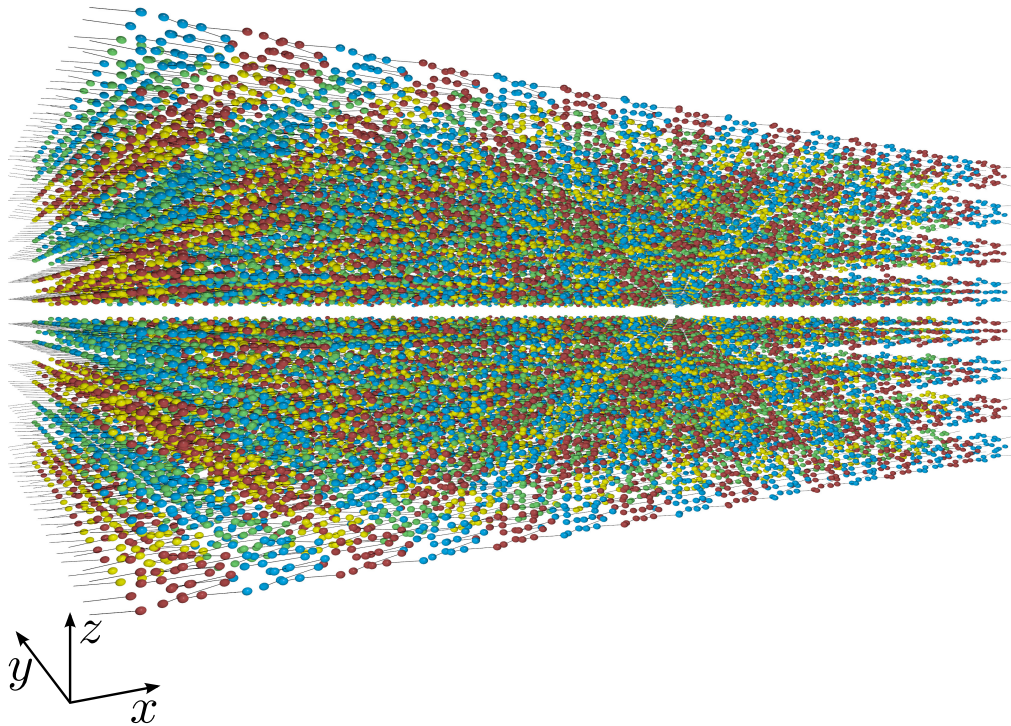
Figure 7.1: A cluster of 11520 bead-spring swimmers, arranged initially on a lattice, after 123 swimming cycles have passed. The display of the springs is suppressed for clarity. Contiguous colours mark beads being simulated on one simulation core. Figure taken from [Pickl, 2016].

### 7.1.4 Swimmer swarms

Study of microswimmer swarms is a fascinating and active field of research, which seeks to explain the various complex long-range dynamic patterns that appear in large populations of microswimmers and which cannot be explained on the level of the individual organisms within the swarm (for a review see Copeland and Weibel [2009]). Some examples of such patterns are plumes [Pedley *et al.*, 1988, Ghorai and Hill, 1999], vortices [Riedel *et al.*, 2005], bands [Guell *et al.*, 1988, Carlile and Dudeney, 1993], and other arrangements [Drescher *et al.*, 2009]. In spite of a lot of research in the field, realistic yet detailed simulations which fully model the individual constituents in a swarm are rare, and the usual approach is to replace the individual active swimmers with effective force fields. While such coarse-grained studies have been very useful, a fully detailed representation of the individual swimmers is certain to yield important insight into the collective effects.

The fully-resolved nature of both our wALBERLA-*pe* and LB3D swimmer simu-
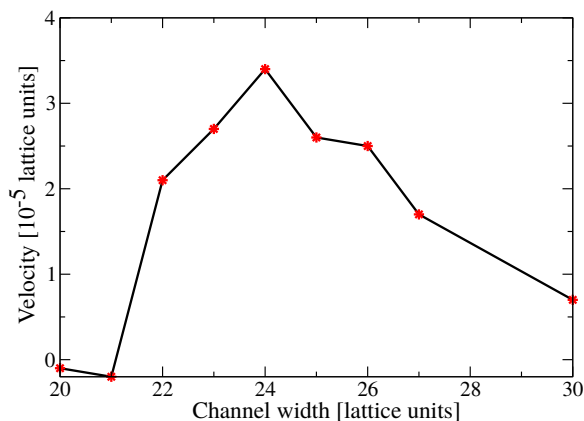
Figure 7.2: The cycle-averaged velocity of a bead-spring swimmer in cuboidal channels of different widths. The thickness of the swimmer, which is the same as the diameter of the spherical beads, is 10 lattice units.

lations, in which we explicitly simulate all the particles in the fluid and treat all the forces at different points on the particle surfaces, makes such realistic modelling of swarms possible. We have in previous work begun to investigate the large-scale effects that emerge in clusters of tens of thousands of bead-spring swimmers in different configurations [Pickl *et al.*, 2016]. We have reported a steady and an unsteady configuration, depending on the uniformity of the lattice on which the swimmers are initially arranged (Fig. 7.1). The unsteady configuration results in the rotation of swimmers in addition to translation, with different swimmers rotating differently depending on their positions within the cluster. This preliminary work needs to be followed upon to characterise the full spectrum of features that swarms are expected to exhibit in their motion.

## 7.1.5   Swimming near boundaries and in constrictions

Another important field of study barely touched upon in this thesis but which would act as a natural extension of it is microswimming near boundaries and in channels. Microswimmers are very often surrounded by or in the presence of confining surfaces and various kinds of flotsam, and it has long been known that their motion in these conditions differs from swimming in the bulk of a fluid. For instance, the accumulation of bull sperm cells near a surface *in vitro* was discussed in Rothschild [1963], and many other instances of similar behaviour by biological swimmers are known [Bernstein and Head, 1984, Winet *et al.*, 1984,
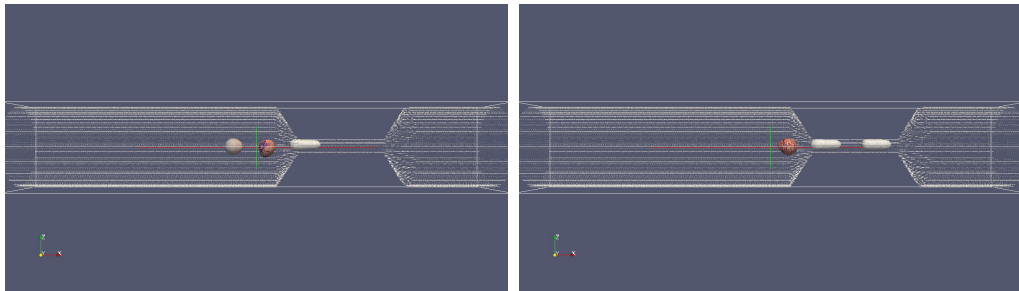
Figure 7.3: Two snapshots of a swimmer with deformable beads passing through a constriction.

Fauci and Mcdonald, 1995, Cosson *et al.*, 2003, Woolley, 2003, Berke *et al.*, 2008, Kantsler *et al.*, 2013]. Various other ways in which surfaces affect swimmer movement have also been discussed in the literature, such as a change in swimming speeds [Reynolds, 1965, Katz, 1974, Katz *et al.*, 1975], rotation and different aligning patterns of pushers and pullers [Berke *et al.*, 2008, Spagnolie and Lauga, 2012], and change in swimming trajectories such as in the case of *E. coli* [Frymier *et al.*, 1995, Vigeant and Ford, 1997, Lauga *et al.*, 2006]. Study of each of these phenomena and more would be enhanced by a detailed swimmer model such as ours and could benefit from the results presented in this thesis. For instance, it is known that the viscous force on a swimmer increases as it approaches a surface, and allied to our results from chapter 3 on the effect of viscosity increase, one may expect the swimmer to show an extremum in the velocity as a function of the distance to the boundary. Indeed, preliminary investigations with simulations suggest just such a behaviour (Fig.7.2).

An allied case is the ability of a swimmer to swim through constrictions of different sizes. In the literature it has been reported that for passive particles, surface deformability can aid them in travelling through narrow channels which prohibit the passage of more rigid bodies [Kusters *et al.*, 2014]. It would be useful to extend this to active swimmers like ours, to study the additional possible benefits of phenomena such as metaboly (Fig. 7.3).

### 7.1.6   Swimming with noise

In all the results presented in this thesis, any diffusive components in the motion of the swimmer were ignored (in other words, the Péclet number, which measures the relative importance of advection and diffusion in determining the transport, was taken to be infinite). While the model has been useful in elucidating many aspects of microswimming–a claim, it is hoped, this thesis sustains–the real world is a lot more chaotic, especially at the micro-scales, and a worthwhile and im-

portant direction of investigation would be the study of our simple model when noise terms are included in the equations of motion. Such an analysis, while challenging and no doubt necessitating appropriate simplifications, would enhance the predictive power of the model *vis-à-vis* real-world swimming of micro-organisms and artificial machines.

### 7.1.7 Comparison with experiments

Last but not the least, while our work has focussed on clarifying the principles underlying microswimming, its worth would be heightened were experimental prototypes designed after the model to be built, tested and, hopefully, gainfully employed in technological applications. As all theoreticians are only too aware of in their disconsolate hearts, the proof of the pudding really does lie in the eating.

## 7.2 Concluding remarks

The field of microswimming is at present a very fertile, very fast-moving one, with new research emerging daily that sheds valuable light on the behaviour of the smallest of our fellow-denizens of Nature, who have until recently guarded their secrets zealously. In this respect, Purcell's famous 1977 lecture [Purcell, 1977], which we have had occasion to mention a few times in this thesis, is a wonderfully representative one, as it captures, even today, the continuing advances in the field, the long way there is to go yet before we can claim to understand the workings of the micro-world, and, most importantly, the excitement of the journey. We hope that our work, partaking of some of this same excitement, has succeeded in illumining a step of the way, and that others will find it fruitful to continue on the path.

118

# A1
# Appendix: Analysis of phase diagram for effect of shape

Here we give a detailed proof of the number of velocity extrema and the drag- or interaction-dominated nature of the swimming as a function of the force amplitude ratio $A/B$ and the force phase difference $\alpha$, for different values of the reduced spring constant $\kappa$ as in Fig. 5.3. As a reminder, the swimming is said to be drag-dominated if the highest velocity over all the swimmers composed of ellipsoids in a given family (prolates or oblates of a constant volume or surface area) is obtained when the drag coefficient of the ellipsoid is at a minimum, *i.e.* for $\mathrm{d}\lambda/\mathrm{d}e = 0$, where $e$ is the aspect ratio of the ellipsoids. If this is not the case, then the maximum velocity magnitude is obtained due to the condition $\mathrm{d}v_{\mathrm{force}}/\mathrm{d}\lambda = 0$ (where $v_{\mathrm{force}}$ is the magnitude of $\mathbf{v}_{\mathrm{force}}$ from Eq. (1.14)) which relates the optimal shape to the different forces acting on the beads, and the swimmer is then in the interaction-dominated regime.
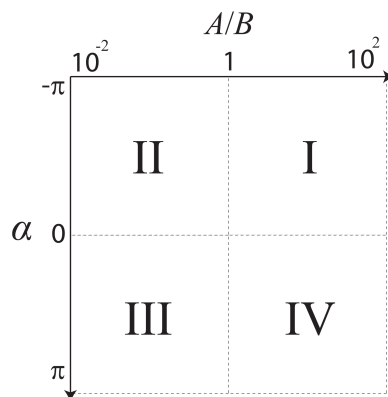


Figure A1.1: Division of phase space into quadrants.

We divide the phase space into four regions as marked on Fig. A1.1. Since the system is invariant under the transformation $\{A \rightarrow B, B \rightarrow A, \alpha \rightarrow -\alpha, \hat{\mathbf{z}} \rightarrow -\hat{\mathbf{z}}\}$, it is clear that the quadrants marked I and III in the phase diagram are analogous, as are those marked II and IV. Therefore, to describe them analytically, we need only focus our attention on, say, quadrants I and IV, where we have $A \geq B$.

We begin by providing a short summary of the number of velocity extrema and the highest velocity obtained over all the ellipsoids in a family for a swimmer at any given point of the phase space (i.e. with given force parameters $A$, $B$ and $\alpha$). Throughout our discussion in this appendix we will employ the following notation:

$$\gamma \equiv \frac{\kappa}{\lambda_{\min}},$$

$$c_i \equiv \frac{\lambda_i}{\kappa}, \text{ where } \lambda_i \ (i = 1 \text{ to } 6) \text{ are obtained from the condition } \frac{\mathrm{d}v_{\text{force}}}{\mathrm{d}\lambda} = 0,$$

$$M \equiv -\sin\alpha, \text{ and}$$

$$N \equiv \frac{A^2 - B^2}{2AB}. \tag{A1.1}$$

Quadrant I is summarised in Table A1, while quadrant IV can be described easily as:

$$\text{if } \gamma < 2\sqrt{3}, \ 1 \text{ extremum, and } v_{\max} = |v_{\lambda_{\min}}|,$$

$$\text{if } 2\sqrt{3} < \gamma, \ 3 \text{ extrema, and } v_{\max} = |v_{\lambda_1}|. \tag{A1.2}$$

Now we describe the different regions in both quadrants I and IV in detail. One extremum of the velocity is obtained through the geometric condition

$$\mathrm{d}\lambda/\mathrm{d}e = 0. \tag{A1.3}$$

Here we would like to determine all the other extrema, obtained through the condition

$$\frac{\mathrm{d}v_{\text{force}}}{\mathrm{d}\lambda} = 0. \tag{A1.4}$$

Table A1.1: Summary of Quadrant I

| $M/N$ | $\gamma$ | # extrema | $v_{\max}$ |
|---|---|---|---|
| $M/N \in \left(\sqrt{3}, \infty\right)$ | $\gamma \in \left(0, 2\sqrt{3}\right)$ | 1 | $\lvert v_{\lambda_{\min}} \rvert$ |
| $M/N \in \left(\sqrt{3}, \infty\right)$ | $\gamma \in \left(2\sqrt{3}, \infty\right)$ | 3 | $\lvert v_{\lambda_1} \rvert$ |
| $M/N \in \left(0, \sqrt{3}\right)$ | $\gamma \in \left(0, 1/c_4\right)$ | 1 | $\lvert v_{\lambda_{\min}} \rvert$ |
| $M/N \in \left(4\sqrt{2} - 3\sqrt{3}, \sqrt{3}\right)$ | $\gamma \in \left(1/c_4, 2\sqrt{3}\right)$ | 3 | $\lvert v_{\lambda_3} \rvert$ |
| $M/N \in \left(0, 4\sqrt{2} - 3\sqrt{3}\right)$ | $\gamma \in \left(\dfrac{1}{c_4}, \dfrac{2\left(N - \sqrt{N^2 - 3M^2}\right)}{M}\right)$ | 3 | $\lvert v_{\lambda_3} \rvert$ |
| $M/N \in \left(0, 4\sqrt{2} - 3\sqrt{3}\right)$ | $\gamma \in \left(\dfrac{2\left(N - \sqrt{N^2 - 3M^2}\right)}{M}, 2\sqrt{3}\right)$ | 3 | $\lvert v_{\lambda_{\min}} \rvert$ |
| $M/N \in \left(4\sqrt{2} - 3\sqrt{3}, \sqrt{3}\right)$ | $\gamma \in \left(2\sqrt{3}, 1/c_3\right)$ | 5 | $\lvert v_{\lambda_3} \rvert$ |
| $M/N \in \left(0, 4\sqrt{2} - 3\sqrt{3}\right)$ | $\gamma \in \left(2\sqrt{3}, 1/c_3\right)$ | 5 | $\lvert v_{\lambda_1} \rvert$ |
| $M/N \in \left(4\sqrt{2} - 3\sqrt{3}, \sqrt{3}\right)$ | $\gamma \in \left(1/c_3, \infty\right)$ | 7 | $\lvert v_{\lambda_3} \rvert$ |
| $M/N \in \left(0, 4\sqrt{2} - 3\sqrt{3}\right)$ | $\gamma \in \left(1/c_3, \infty\right)$ | 7 | $\lvert v_{\lambda_1} \rvert$ |

This gives the following 6 solutions for $\lambda$.

$$\lambda_{1,2} = \pm\kappa\frac{1}{2\sqrt{3}}$$

$$\equiv c_{1,2}\kappa,$$

$$\lambda_{3,4} = \kappa\frac{-1}{12AB}\left\{\frac{\left(A^2 - B^2 + \sqrt{A^4 + B^4 - 2A^2B^2\cos(2\alpha)}\right)}{\sin\alpha}\right.$$

$$\left.\pm\sqrt{\frac{2\left(A^4 + B^4 + 2A^2B^2\cos(2\alpha) - 4A^2B^2 + \left(A^2 - B^2\right)\sqrt{A^4 + B^4 - 2A^2B^2\cos(2\alpha)}\right)}{\sin^2\alpha}}\right\}$$

$$\equiv c_{3,4}\kappa,$$

$$\lambda_{5,6} = \frac{-\kappa}{12AB}\left\{\frac{\left(A^2 - B^2 - \sqrt{A^4 + B^4 - 2A^2B^2\cos(2\alpha)}\right)}{\sin\alpha}\right.$$

$$\left.\pm\sqrt{\frac{2\left(A^4 + B^4 + 2A^2B^2\cos(2\alpha) - 4A^2B^2 - \left(A^2 - B^2\right)\sqrt{A^4 + B^4 - 2A^2B^2\cos(2\alpha)}\right)}{\sin^2\alpha}}\right\}$$

$$\equiv c_{5,6}\kappa. \tag{A1.5}$$

Here we have defined $c_i$ ($i = 1, 2, ..., 6$) as $\lambda_i/\kappa$, and they are functions only of the forcing parameters $A$, $B$ and $\alpha$.

To simplify notation, we write these solutions in terms of the dimensionless variables $M$ and $N$ defined by

$$M = -\sin\alpha$$
$$N = \frac{A^2 - B^2}{2AB}. \tag{A1.6}$$

The $c_i$'s in Eq. (A1.5) are then

$$c_{1,2} = \pm \frac{1}{2\sqrt{3}},$$

$$c_{3,4} = \frac{1}{6} \left[ \frac{N + \sqrt{N^2 + M^2}}{M} \mp \sqrt{\frac{2\left(N^2 - M^2 + N\sqrt{N^2 + M^2}\right)}{M^2}} \right],$$

$$c_{5,6} = \frac{1}{6} \left[ \frac{N - \sqrt{N^2 + M^2}}{M} \mp \sqrt{\frac{2\left(N^2 - M^2 - N\sqrt{N^2 + M^2}\right)}{M^2}} \right], \qquad \text{(A1.7)}$$

from which the $\lambda_i$'s can of course be immediately obtained.

The $\lambda$ solutions lead to the following expressions for the velocity extrema,

$$v_{\lambda_{1,2}} = \frac{7AB\left(N \mp \sqrt{3}M\right)}{384\pi^2\eta^2\omega l^3\kappa},$$

$$v_{\lambda_3} = v_{\lambda_4} = \frac{7AB\left(N - \sqrt{N^2 + M^2}\right)}{192\pi^2\eta^2\omega l^3\kappa},$$

$$v_{\lambda_5} = v_{\lambda_6} = \frac{7AB\left(N + \sqrt{N^2 + M^2}\right)}{192\pi^2\eta^2\omega l^3\kappa}. \qquad \text{(A1.8)}$$

Since $\lambda_3$ and $\lambda_4$ result in the same velocity, and so do $\lambda_5$ and $\lambda_6$, one can, *a priori*, only have five distinct velocity extrema values, including the extremum obtained from the geometric condition $d\lambda/de = 0$. This latter can be expressed as

$$v_{\lambda_{\min}} = \frac{7AB\gamma\left[4\gamma N - \left(\gamma^2 + 12\right)M\right]}{24\pi^2\eta^2\omega l^3\kappa\left(\gamma^4 + 40\gamma^2 + 144\right)}, \qquad \text{(A1.9)}$$

where the quantity $\gamma = \kappa/\lambda_{\min}$ has been introduced in order to keep the subsequent treatment independent of the particular value of $\lambda_{\min}$.

From Eq. (A1.5), $\lambda_2(< 0)$ is clearly a disallowed root, which renders $v_{\lambda_2}$ too invalid. Now we will show that for $B \geq A$, $\lambda_3$ and $\lambda_4$ are disallowed, while for $A \geq B$, $\lambda_5$ and $\lambda_6$ are disallowed. This will imply that for any $B/A$ ratio, there are at most only two non-degenerate velocity extrema values obtained from $dv_{\text{force}}/d\lambda = 0$, in addition to $v_{\lambda_{\min}}$ obtained from $d\lambda/de = 0$.

So assume $B \geq A$. This means $N \leq 0$. We will show that then $N^2 - M^2 + N\sqrt{N^2 + M^2} < 0$, implying that $\lambda_{3,4} \notin \mathbb{R}$.

Suppose that $N^2 - M^2 + N\sqrt{N^2 + M^2} \geq 0$.

$$\Rightarrow N^2 \geq M^2 - N\sqrt{N^2 + M^2} \geq 0 \quad (\because N \leq 0).$$
$$\Rightarrow N^4 \geq M^4 + N^2\left(N^2 + M^2\right) + 2M^2(-N)\sqrt{N^2 + M^2}.$$
$$\Rightarrow 0 \geq M^4 + N^2 M^2 + 2M^2(-N)\sqrt{N^2 + M^2}.$$

This is impossible unless $N = M = 0$, which is of course a disallowed case. Therefore we have reached a contradiction, and our proof is done. In an exactly analogous manner, one can show that if $A \geq B$, then $\lambda_{5,6} \notin \mathbb{R}$.

Therefore, if $A \geq B$, then the only possible velocity extrema values are $v_{\lambda_{\min}}$, $v_{\lambda_1}$ and $v_{\lambda_3}$, whereas if $B \geq A$, then the only possible velocity extrema values are $v_{\lambda_{\min}}$, $v_{\lambda_1}$ and $v_{\lambda_5}$.

## A1.1  Quadrant I ($A \geq B, -\pi \leq \alpha \leq 0$)

Here $A \geq B$ and $-\pi \leq \alpha \leq 0$, meaning that $0 \leq N$ and $0 \leq M \leq 1$. We showed above that in this case, $\lambda_5$ and $\lambda_6$ are invalid solutions to Eq. (A1.4). We will show that if $M > \sqrt{3}N$, then $\lambda_3$ and $\lambda_4$ are invalid too.

So let $N < \dfrac{M}{\sqrt{3}}$.

$$\Rightarrow N^2 - M^2 < \frac{-2M^2}{3} \text{ and } N^2 + M^2 < \frac{4M^2}{3}$$
$$\Rightarrow N^2 - M^2 + N\sqrt{N^2 + M^2} < \frac{-2M^2}{3} + \frac{2M^2}{3} = 0.$$
$$\Rightarrow c_{3,4} \notin \mathbb{R}. \tag{A1.10}$$

Therefore, for $M > \sqrt{3}N$, the only possible $\lambda$ solution to Eq. (A1.4) is $\lambda_1$, and, consequently, the only possible velocity extrema values are $v_{\lambda_{\min}}$ and $v_{\lambda_1}$.

### A1.1.1  $M > \sqrt{3}N$

We will describe the number of velocity extrema and the global velocity maximum for the different possible values of $\gamma = \kappa/\lambda_{\min}$.

$\gamma < 2\sqrt{3}$

In this case, the only velocity extremum is obtained at $\lambda = \lambda_{\min}$, so we have $v_{\max} = |v_{\lambda_{\min}}|$.

$\gamma > 2\sqrt{3}$

In this case, there are three velocity extrema, two of them obtained for $\lambda = \lambda_1$ and one for $\lambda = \lambda_{\min}$. To determine the global velocity maximum, we will compare $|v_{\lambda_{\min}}|$ and $|v_{\lambda_1}|$. Since $N \geq 0$ and $M \geq 0$, it is clear from the expressions in (A1.8) that both $v_{\lambda_{\min}}$ and $v_{\lambda_1}$ are negative.

Suppose $|v_{\lambda_{\min}}| > |v_{\lambda_1}|. \Rightarrow v_{\lambda_1} > v_{\lambda_{\min}}$.

$$\Rightarrow \frac{7AB\left(N - \sqrt{3}M\right)}{384\pi^2\eta^2\omega l^3\kappa} > \frac{7AB\gamma\left[4\gamma N - \left(\gamma^2 + 12\right)M\right]}{24\pi^2\eta^2\omega l^3\kappa\left(\gamma^4 + 40\gamma^2 + 144\right)}.$$

$$\Rightarrow \left(N - \sqrt{3}M\right)\gamma^4 + 16M\gamma^3 + \left(-24N - 40\sqrt{3}M\right)\gamma^2$$
$$+ 192M\gamma + 144\left(N - \sqrt{3}M\right) \qquad\qquad > 0.$$
$$\Rightarrow \left(N - \sqrt{3}M\right)\left(\gamma - 2\sqrt{3}\right)^2\left(\gamma - \gamma_1\right)\left(\gamma - \gamma_2\right) > 0, \qquad (A1.11)$$

where

$$\gamma_{1,2} = \frac{2\left(M + \sqrt{3}N \pm \sqrt{8M\left(\sqrt{3}N - M\right)}\right)}{\sqrt{3}M - N}. \qquad (A1.12)$$

$$\Rightarrow \left(\gamma - \gamma_1\right)\left(\gamma - \gamma_2\right) < 0, \quad \left(\text{since } \left(N - \sqrt{3}M\right) < 0\right) \qquad (A1.13)$$

The expression under the square root sign in $\gamma_{1,2}$ is clearly negative, meaning $\gamma_{1,2} \notin \mathbb{R}$. Consequently, the relation (A1.11) is satisfied for no $\gamma$, and we arrive at a contradiction. This means that,

$$\text{for } \gamma > 2\sqrt{3} \text{ (with } M > \sqrt{3}N\text{), we have } v_{\max} = |v_{\lambda_1}|. \qquad (A1.14)$$

Now we let $M < \sqrt{3}N$.

## A1.1.2   $M < \sqrt{3}N$

In this case, the first thing to check is whether $\lambda_{3,4}$ are valid solutions to Eq. (A1.4) or not. Clearly, now, $c_{3,4} \in \mathbb{R}$, and $c_4 > c_3$. So for both $\lambda_3$ and $\lambda_4$ to be valid solutions, we need to have $c_3 > 0$.

Suppose that $c_3 < 0$.

$$\Rightarrow (0 <) \frac{N + \sqrt{N^2 + M^2}}{M} < \sqrt{\frac{2\left(N^2 - M^2 + N\sqrt{N^2 + M^2}\right)}{M^2}}.$$

$$\Rightarrow N^2 + N^2 + M^2 + 2N\sqrt{N^2 + M^2} < 2\left(N^2 - M^2 + N\sqrt{N^2 + M^2}\right).$$

$$\Rightarrow 3M^2 < 0. \tag{A1.15}$$

So we reach a contradiction, and consequently, in this case, $c_{3,4} > 0$.

Having established the existence of $c_3$ and $c_4$, one can now show (or check explicitly via *Mathematica*) that

$$\lambda_4 \geq \lambda_1 \geq \lambda_3$$

$$\Rightarrow \frac{1}{c_3} \geq 2\sqrt{3} \geq \frac{1}{c_4}. \tag{A1.16}$$

We determine the number of velocity extrema as well as the global velocity maximum for the different possible values of $\kappa$, or, equivalently, $\gamma$.

$$\gamma < \frac{1}{c_4}$$

In this case $\kappa$ is so small that $c_4\kappa < \lambda_{\min}$, meaning that Eq. (A1.4) has no solution for $\lambda$. Therefore, the only velocity extremum is obtained at $\lambda_{\min}$, and consequently $v_{\max} = |v_{\lambda_{\min}}|$.

$$\frac{1}{c_4} < \gamma < 2\sqrt{3}$$

In this case, there are three velocity extrema, two of them obtained for $\lambda = \lambda_4$ and one for $\lambda = \lambda_{\min}$. The different velocity extrema values in this case are $v_{\lambda_{\min}}$ and $v_{\lambda_3}$. We would like to determine the global maximum velocity, for which we will compare $|v_{\lambda_{\min}}|$ and $|v_{\lambda_3}|$.

From Eq. (A1.8), clearly $v_{\lambda_3} < 0$, therefore $|v_{\lambda_3}| = -v_{\lambda_3}$. Suppose now that $|v_{\lambda_{\min}}| = v_{\lambda_{\min}}$. This means

$$v_{\lambda_{\min}} > 0.$$

$$\Rightarrow 4\gamma N - \left(\gamma^2 + 12\right)M > 0. \tag{A1.17}$$

The discriminant of the left hand side is negative if $N^2 < 3M^2$. Therefore,

$$-\text{if } M > \frac{N}{\sqrt{3}}, \text{ then } v_{\lambda_{\min}} < 0 \text{ for all possible } \gamma, \text{ and} \qquad \text{(A1.18)}$$

$$-\text{if } 0 < M < \frac{N}{\sqrt{3}}, \text{ then}$$

$$v_{\lambda_{\min}} > 0, \text{ for } \gamma \in \left( \frac{2\left(N - \sqrt{N^2 - 3M^2}\right)}{M}, \frac{2\left(N + \sqrt{N^2 - 3M^2}\right)}{M} \right)$$

$$v_{\lambda_{\min}} < 0, \text{ otherwise.} \qquad \text{(A1.19)}$$

So first let $M > \frac{N}{\sqrt{3}}$. Then, $|v_{\lambda_{\min}}| = -v_{\lambda_{\min}}$. Suppose in this case that $|v_{\lambda_{\min}}| > |v_{\lambda_3}|$.

$$\Rightarrow \frac{7AB\left(N - \sqrt{N^2 + M^2}\right)}{192\pi^2\eta^2\omega l^3\kappa} > \frac{7AB\gamma\left[4\gamma N - \left(\gamma^2 + 12\right)M\right]}{24\pi^2\eta^2\omega l^3\kappa\left(\gamma^4 + 40\gamma^2 + 144\right)}.$$

$$\Rightarrow \left(N - \sqrt{N^2 + M^2}\right)\gamma^4 + 8M\gamma^3 + \left(8N - 40\sqrt{N^2 + M^2}\right)\gamma^2$$
$$+ 96M\gamma + 144\left(N - \sqrt{N^2 + M^2}\right) \qquad\qquad > 0. \quad \text{(A1.20)}$$

Using *Mathematica*, one can check that this relation holds for no value of $\gamma > 0$, if $N > 0$ and $M > 0$. So we reach a contradiction, meaning that

$$\text{for } M > \frac{N}{\sqrt{3}}, \; v_{\max} = |v_{\lambda_3}|. \qquad \text{(A1.21)}$$

Now suppose that $M < \frac{N}{\sqrt{3}}$. Since in this case $v_{\lambda_{\min}}$ can be positive or negative, assume first that $\gamma$ is such that $v_{\lambda_{\min}} < 0$.

In this case, suppose that $|v_{\lambda_{\min}}| > |v_{\lambda_3}|$. $\Rightarrow v_{\lambda_3} > v_{\lambda_{\min}}$.

$$\Rightarrow \frac{7AB\left(N - \sqrt{N^2 + M^2}\right)}{192\pi^2\eta^2\omega l^3\kappa} > \frac{7AB\gamma\left[4\gamma N - \left(\gamma^2 + 12\right)M\right]}{24\pi^2\eta^2\omega l^3\kappa\left(\gamma^4 + 40\gamma^2 + 144\right)}.$$
$$\text{(A1.22)}$$

From this, we get the same inequality as in relation (A1.20), and so again there is no solution for any $\gamma > 0$ if $N > 0$ and $M > 0$. Therefore for $M < \frac{N}{\sqrt{3}}$, if $\gamma$ is

such that $v_{\lambda_{\min}} < 0$, we have $|v_{\lambda_3}| \geq |v_{\lambda_{\min}}|$.

Now assume that $\gamma$ is such that $v_{\lambda_{\min}} > 0$. And, in this case, suppose that $|v_{\lambda_{\min}}| > |v_{\lambda_3}|. \Rightarrow v_{\lambda_{\min}} > -v_{\lambda_3}$.

$$\Rightarrow \frac{7AB\gamma\left[4\gamma N - \left(\gamma^2 + 12\right)M\right]}{24\pi^2\eta^2\omega l^3\kappa\left(\gamma^4 + 40\gamma^2 + 144\right)} > \frac{-7AB\left(N - \sqrt{N^2 + M^2}\right)}{192\pi^2\eta^2\omega l^3\kappa}.$$

$$\Rightarrow \left(\sqrt{N^2 + M^2} - N\right)\gamma^4 + 8M\gamma^3 + \left(40\sqrt{N^2 + M^2} - 72N\right)\gamma^2$$
$$+ 96M\gamma + 144\left(\sqrt{N^2 + M^2} - N\right) \qquad\qquad < 0. \quad \text{(A1.23)}$$

It is possible to factorize the left hand side of the inequality in relation (A1.23) as $\left(\sqrt{N^2 + M^2} - N\right)(\gamma - \gamma_1)(\gamma - \gamma_2)(\gamma - \gamma_3)(\gamma - \gamma_4)$. (The $\gamma_i$'s here are rather large and unwieldy expressions and are thus not listed here.) Therefore, we have

$$\left(\sqrt{N^2 + M^2} - N\right)(\gamma - \gamma_1)(\gamma - \gamma_2)(\gamma - \gamma_3)(\gamma - \gamma_4) < 0. \qquad \text{(A1.24)}$$

It can be shown (or checked using *Mathematica*) that for $0 < M < N\sqrt{3}$, we have $\gamma_1 < 0$ and $\gamma_2 < 0$. Moreover, for $M > \left(4\sqrt{2} - 3\sqrt{3}\right)N$, $\gamma_3 \notin \mathbb{R}$ and $\gamma_4 \notin \mathbb{R}$. Also it ought to be borne in mind that relation (A1.23) is obtained under the assumption $v_{\lambda_{\min}} > 0$, which means that any $\gamma$ solution to it must also satisfy, from relation (A1.19),

$$\gamma \in \left(\frac{2\left(N - \sqrt{N^2 - 3M^2}\right)}{M}, \frac{2\left(N + \sqrt{N^2 - 3M^2}\right)}{M}\right). \qquad \text{(A1.25)}$$

It can be shown that $\dfrac{2\left(N - \sqrt{N^2 - 3M^2}\right)}{M} \leq 2\sqrt{3}$ and $\dfrac{2\left(N + \sqrt{N^2 - 3M^2}\right)}{M} \geq 2\sqrt{3}$, for $M < \dfrac{N}{\sqrt{3}}$. Therefore, the $\gamma$ range above reduces to

$$\gamma \in \left(\frac{2\left(N - \sqrt{N^2 - 3M^2}\right)}{M}, 2\sqrt{3}\right). \qquad \text{(A1.26)}$$

From all these considerations, one finds that for $M < \dfrac{N}{\sqrt{3}}$,

$$-\text{if } 0 < M < \left(4\sqrt{2} - 3\sqrt{3}\right)N \text{ and } \gamma \in \left(\frac{2\left(N - \sqrt{N^2 - 3M^2}\right)}{M}, 2\sqrt{3}\right],$$

then $v_{\text{max}} = |v_{\lambda_{\text{min}}}|$,

$-$otherwise $v_{\text{max}} = |v_{\lambda_3}|$. (A1.27)

$$2\sqrt{3} < \gamma < \frac{1}{c_3}$$

In this case, there are five velocity extrema, two of them obtained for $\lambda = \lambda_4$, two for $\lambda = \lambda_1$ and one for $\lambda = \lambda_{\text{min}}$. These different values for $\lambda$ yield respectively $v_{\lambda_3}$, $v_{\lambda_1}$ and $v_{\lambda_{\text{min}}}$ as the corresponding velocity extrema. As before, we would like to determine the largest of these velocity extrema for different forcing parameters.

We begin with comparing $|v_{\lambda_3}|$ and $|v_{\lambda_{\text{min}}}|$.

Much of the comparison is identical to that in section A1.1.2. For instance, it can be shown that, as before,

$$\text{for } M > \frac{N}{\sqrt{3}}, \text{ we have } |v_{\lambda_3}| \geq |v_{\lambda_{\text{min}}}|. \tag{A1.28}$$

For the case $0 < M < \dfrac{N}{\sqrt{3}}$, we find, analogously (but not identically) to (A1.27), that

$$-\text{if } 0 < M < \left(4\sqrt{2} - 3\sqrt{3}\right)N \text{ and } \gamma \in \left(2\sqrt{3}, \frac{2\left(N + \sqrt{N^2 - 3M^2}\right)}{M}\right),$$

then $|v_{\lambda_{\text{min}}}| > |v_{\lambda_3}|$,

$-$otherwise $|v_{\lambda_3}| \geq |v_{\lambda_{\text{min}}}|$. (A1.29)

Next we compare $|v_{\lambda_1}|$ and $|v_{\lambda_{\text{min}}}|$. Since we are only interested in the global velocity maximum and know that for $M > \left(4\sqrt{2} - 3\sqrt{3}\right)N$, we have $|v_{\lambda_3}| \geq |v_{\lambda_{\text{min}}}|$, we need only concern ourselves with the relative order of $|v_{\lambda_1}|$ and $|v_{\lambda_{\text{min}}}|$ for $M < \left(4\sqrt{2} - 3\sqrt{3}\right)N$.

So let $M < \left(4\sqrt{2} - 3\sqrt{3}\right)N$. This means $v_{\lambda_1} > 0$, but the sign of $v_{\lambda_{\text{min}}}$ depends on $\gamma$.

Assume first that $\gamma$ is such that $v_{\lambda_{\text{min}}} > 0$. In this case, suppose that $|v_{\lambda_{\text{min}}}| >$

$|v_{\lambda_1}|.$

$$\Rightarrow \frac{7AB\gamma\left[4\gamma N - \left(\gamma^2 + 12\right)M\right]}{24\pi^2\eta^2\omega l^3\kappa\left(\gamma^4 + 40\gamma^2 + 144\right)} > \frac{7AB\left(N - \sqrt{3}M\right)}{384\pi^2\eta^2\omega l^3\kappa}.$$

$$\Rightarrow \left(N - \sqrt{3}M\right)\gamma^4 + 16M\gamma^3 + \left(-24N - 40\sqrt{3}M\right)\gamma^2 + 192M\gamma + 144\left(N - \sqrt{3}M\right) < 0.$$

$$\Rightarrow \left(N - \sqrt{3}M\right)\left(\gamma - 2\sqrt{3}\right)^2\left(\gamma - \gamma_1\right)\left(\gamma - \gamma_2\right) < 0, \tag{A1.30}$$

where

$$\gamma_{1,2} = \frac{2\left(M + \sqrt{3}N \pm \sqrt{8M\left(\sqrt{3}N - M\right)}\right)}{\sqrt{3}M - N}. \tag{A1.31}$$

It can be shown that $\gamma_{1,2} < 0$, which renders inequality (A1.30) non-satisfiable for $\gamma > 0$. So we reach a contradiction, and therefore in this case $|v_{\lambda_1}| \geq |v_{\lambda_{\min}}|$.

Now assume that $\gamma$ is such that $v_{\lambda_{\min}} < 0$, and again suppose that $|v_{\lambda_{\min}}| > |v_{\lambda_1}|$.

$$\Rightarrow \frac{-7AB\gamma\left[4\gamma N - \left(\gamma^2 + 12\right)M\right]}{24\pi^2\eta^2\omega l^3\kappa\left(\gamma^4 + 40\gamma^2 + 144\right)} > \frac{7AB\left(N - \sqrt{3}M\right)}{384\pi^2\eta^2\omega l^3\kappa}.$$

$$\Rightarrow \left(N - \sqrt{3}M\right)\gamma^4 - 16M\gamma^3 + \left(104N - 40\sqrt{3}M\right)\gamma^2 - 192M\gamma + 144\left(N - \sqrt{3}M\right) \qquad < 0. \tag{A1.32}$$

Checking this inequality using *Mathematica*, one finds that it has no solution for $0 < M < \left(4\sqrt{2} - 3\sqrt{3}\right)N$. Therefore we reach a contradiction again, and so again, $|v_{\lambda_1}| \geq |v_{\lambda_{\min}}|$.

The above analysis of the relative order of the different velocity extrema shows that for any given value of $M$, $N$ and $\gamma$, $|v_{\lambda_{\min}}|$ is smaller than at least one of $|v_{\lambda_1}|$ and $|v_{\lambda_3}|$. So, to determine the global velocity maximum, we finally need to only compare the magnitudes of $v_{\lambda_1}$ and $v_{\lambda_3}$, as the larger of the two quantities will give the global $v_{\max}$.

Now as we know, $v_{\lambda_3} < 0$, always, while $v_{\lambda_1} < (>)0$ for $M > (<)\dfrac{N}{\sqrt{3}}$.

So first consider the case $M > \dfrac{N}{\sqrt{3}}$, and suppose that, then, $|v_{\lambda_1}| > |v_{\lambda_3}|$.

$$\Rightarrow \frac{7AB\left(N - \sqrt{N^2 + M^2}\right)}{192\pi^2\eta^2\omega l^3\kappa} > \frac{7AB\left(N - \sqrt{3}M\right)}{384\pi^2\eta^2\omega l^3\kappa}.$$

$$\Rightarrow N + \sqrt{3}M > 2\sqrt{N^2 + M^2} > 0.$$
$$\Rightarrow N^2 + 3M^2 + 2\sqrt{3}MN > 4N^2 + 4M^2.$$
$$\Rightarrow \left(M - \sqrt{3}N\right)^2 < 0. \tag{A1.33}$$

This is a contradiction, therefore

$$\text{for } M > \frac{N}{\sqrt{3}}, \text{ we have } |v_{\lambda_3}| \geq |v_{\lambda_1}|. \tag{A1.34}$$

Now consider the case $M < \dfrac{N}{\sqrt{3}}$, and again suppose that $|v_{\lambda_1}| > |v_{\lambda_3}|$.

$$\Rightarrow \frac{7AB\left(N - \sqrt{3}M\right)}{384\pi^2\eta^2\omega l^3\kappa} > \frac{-7AB\left(N - \sqrt{N^2 + M^2}\right)}{192\pi^2\eta^2\omega l^3\kappa}.$$

$$\Rightarrow 3N - \sqrt{3}M > 2\sqrt{N^2 + M^2} > 0.$$
$$\Rightarrow M^2 + \left(6\sqrt{3}N\right)M - 5N^2 < 0.$$
$$\Rightarrow M \in \left(0, \left(4\sqrt{2} - 3\sqrt{3}\right)N\right). \tag{A1.35}$$

Therefore, finally, we find that

$$-\text{if } 0 < M < \left(4\sqrt{2} - 3\sqrt{3}\right)N, \text{ then } v_{\max} = |v_{\lambda_1}|,$$
$$-\text{if } \left(4\sqrt{2} - 3\sqrt{3}\right)N < M, \text{ then } v_{\max} = |v_{\lambda_3}|. \tag{A1.36}$$

$$\frac{1}{c_3} < \gamma$$

In this case there are seven velocity extrema, two of them obtained for $\lambda = \lambda_4$, two for $\lambda = \lambda_1$, two for $\lambda = \lambda_3$ and one for $\lambda = \lambda_{\min}$. These yield $v_{\lambda_3}$ (from $\lambda_4$ and $\lambda_3$), $v_{\lambda_1}$ (from $\lambda_1$) and $v_{\lambda_{\min}}$ (from $\lambda_{\min}$) as the velocity extrema values. The relative order of the magnitudes of these velocity extrema is exactly the same as in section A1.1.2 above.

So with that, we have finished the description of quadrant I.

## A1.2   Quadrant IV ($A \geq B, 0 \leq \alpha \leq \pi$)

Here $A \geq B$ and $0 \leq \alpha \leq \pi$, meaning that $0 \leq N$ and $-1 \leq M \leq 0$. We recall that for $A \geq B$, $\lambda_5$ and $\lambda_6$ are invalid solutions to Eq. (A1.4). We will show now that here $\lambda_3$ and $\lambda_4$ too are invalid.

From (A1.7),

$$c_3 = \frac{1}{6}\left[\frac{N + \sqrt{N^2 + M^2}}{M} - \sqrt{\frac{2\left(N^2 - M^2 + N\sqrt{N^2 + M^2}\right)}{M^2}}\right]$$

$$\Rightarrow c_3 < 0, \text{ for } N > 0 \text{ and } M < 0. \tag{A1.37}$$

So $\lambda_3$ is an invalid solution to Eq. (A1.4).

Now assume that $c_4 > 0$.

$$\Rightarrow \sqrt{\frac{2\left(N^2 - M^2 + N\sqrt{N^2 + M^2}\right)}{M^2}} > \frac{N + \sqrt{N^2 + M^2}}{(-M)}. \tag{A1.38}$$

Since both sides are positive, we can square them without changing the inequality. Doing that, though, finally yields

$$3M^2 < 0, \tag{A1.39}$$

which is a contradiction. Therefore, $c_4 \leq 0$, and $\lambda_4$ is shown to be invalid too. So the only possible $\lambda$-solution to Eq. (A1.4) is $\lambda_1 (= \kappa/\sqrt{3})$, and, consequently, the only possible velocity extrema values are $v_{\lambda_{\min}}$ and $v_{\lambda_1}$. As before, we will describe the number of velocity extrema and the global velocity maximum for the different possible values of $\gamma = \kappa/\lambda_{\min}$.

### $\gamma < 2\sqrt{3}$

In this case, the only velocity extremum is obtained at $\lambda = \lambda_{\min}$, so we have $v_{\max} = |v_{\lambda_{\min}}|$.

### $\gamma > 2\sqrt{3}$

In this case, there are three velocity extrema, two of them obtained for $\lambda = \lambda_1$ and one for $\lambda = \lambda_{\min}$. To determine the global velocity maximum, we will compare

$|v_{\lambda_{\min}}|$ and $|v_{\lambda_1}|$. Since $N \geq 0$ and $M \leq 0$, it is clear from the expressions in (A1.8) that both $v_{\lambda_{\min}}$ and $v_{\lambda_1}$ are positive.

Suppose $|v_{\lambda_{\min}}| > |v_{\lambda_1}|$.

$$\Rightarrow \frac{7AB\gamma\left[4\gamma N - \left(\gamma^2 + 12\right)M\right]}{24\pi^2\eta^2\omega l^3\kappa\left(\gamma^4 + 40\gamma^2 + 144\right)} > \frac{7AB\left(N - \sqrt{3}M\right)}{384\pi^2\eta^2\omega l^3\kappa}.$$

$$\Rightarrow \left(N - \sqrt{3}M\right)\gamma^4 + 16M\gamma^3 + \left(-24N - 40\sqrt{3}M\right)\gamma^2$$
$$+ 192M\gamma + 144\left(N - \sqrt{3}M\right) \qquad\qquad < 0.$$

$$\Rightarrow \left(N - \sqrt{3}M\right)\left(\gamma - 2\sqrt{3}\right)^2\left(\gamma - \gamma_1\right)\left(\gamma - \gamma_2\right) < 0, \qquad\qquad \text{(A1.40)}$$

where

$$\gamma_{1,2} = \frac{2\left(M + \sqrt{3}N \pm \sqrt{8M\left(\sqrt{3}N - M\right)}\right)}{\sqrt{3}M - N}. \qquad\qquad \text{(A1.41)}$$

The expression under the square root sign in $\gamma_{1,2}$ is clearly negative, meaning $\gamma_{1,2} \notin \mathbb{R}$. Consequently, the relation (A1.40) is satisfied for no $\gamma$, and we arrive at a contradiction. This means that,

$$\text{for } \gamma > 2\sqrt{3}, \text{ we have } v_{\max} = |v_{\lambda_1}|. \qquad\qquad \text{(A1.42)}$$

This concludes our proof.

134

# List of Figures

# Part III

# Bibliography

# Bibliography

M. Abkarian, M. Faivre, and A. Viallat. Swinging of red blood cells under shear flow. *Phys. Rev. Lett.*, 98:188302, 2007.

J. L. Aguirre and T. J. Murphy. Brownian motion of *N* interacting particles. II. Hydrodynamical evaluation of the diffusion tensor matrix. *J. Chem. Phys.*, 59: 1833, 1973.

C. K. Aidun and J. R. Clausen. Lattice-Boltzmann method for complex flows. *Annu. Rev. Fluid Mech.*, 42:439, 2010.

G. P. Alexander, C. M. Pooley, and J. M. Yeomans. Scattering of low-Reynolds-number swimmers. *Phys. Rev. E*, 78:045302(R), 2008.

F. Alouges, A. DeSimone, and A. Lefebvre. Optimal strokes for low Reynolds number swimmers: An example. *J. Nonlinear Sci.*, 18:277, 2008.

F. Alouges, A. DeSimone, and A. Lefebvre. Optimal strokes for axisymmetric microswimmers. *Eur. Phys. J. E*, 28:279, 2009.

L. Alvarez, B. M.. Friedrich, G. Gompper, and U. B. Kaupp. The computational sperm cell. *Trends Cell Biol.*, 24:198, 2014.

J. P. Armitage and R. M. Macnab. Unidirectional, intermittent rotation of the flagellum of *Rhodobacter sphaeroides*. *J. Bacteriol.*, 169:514, 1987.

J. P. Armitage and R. Schmitt. Bacterial chemotaxis: *Rhodobacter sphaeroides* and *Sinorhizobium meliloti*–variations on a theme? *Microbiology*, 143:3671, 1997.

M. Arroyo, L. Heltai, D. Millán, and A. DeSimone. Reverse engineering the euglenoid movement. *Proc. Natl. Acad. Sci. USA*, 109:17874, 2012.

J. E. Avron, O. Gat, and O. Kenneth. Optimal swimming at low Reynolds numbers. *Phys. Rev. Lett.*, 93(18):186001, 2004.

J. E. Avron, O. Kenneth, and D. H. Oaknin. Pushmepullyou: an efficient microswimmer. *New J. Phys.*, 7:234, 2005.

A. Azuma. *The Biokinetics of Flying and Swimming*. Springer-Verlag, Tokyo, 1992.

L. Baraban, D. Makarov, R. Streubel, I. Mönch, D. Grimm, S. Sanchez, and O. G. Schmidt. Catalytic janus motors on microuidic chip: Deterministic motion for targeted cargo delivery. *ACS Nano*, 6:3383, 2012.

D. Barthès-Biesel. Motion of a spherical microcapsule freely suspended in a linear shear flow. *J. Fluid Mech.*, 100:831, 1980.

L. E. Becker, S. A. Koehler, and H. A. Stone. On self-propulsion of micromachines at low Reynolds number: Purcell's three-link swimmer. *J. Fluid Mech.*, 490:15, 2003.

R. Benzi, S. Succi, and M. Vergassola. The lattice Boltzmann equation theory and applications. *Phys. Rep.*, 222:45, 1992.

H. C. Berg. How spirochetes may swim. *J. Theo. Biol.*, 56:269, 1976.

H. C. Berg. *E. Coli in Motion*. Springer (New York), 2004.

H. C. Berg and L. Turner. Movement of microorganisms in viscous environments. *Nature*, 278:349, 1979.

A. P. Berke, L. Turner, H. C. Berg, and E. Lauga. Hydrodynamic attraction of swimming microorganisms by surfaces. *Phys. Rev. Lett.*, 101:038102, 2008.

H. Winet G. S. Bernstein and J. Head. Observations on the response of human spermatozoa to gravity, boundaries and fluid shear. *J. Reprod. Fertil.*, 70:511, 1984.

B. Bet, G. Boosten, M. Dijkstra, and R. van Roij. Efficient shapes for microswimming: from three-body swimmers to helical flagella. *arXiv:1603.02629 [cond-mat.soft]*, 2016.

P. L. Bhatnagar, E. P. Gross, and M. Krook. A model for collision processes in gases. I. Small amplitude processes in charged and neutral one-component systems. *Phys. Rev.*, 94:511, 1954.

J. F. Biddle, J. S. Lipp, M. A. Lever, K. G. Lloyd, K. B. Sørensen, R. Anderson, H. F. Fredricks, M. Elvert, T. J. Kelly, D. P. Schrag, M. L. Sogin, J. E. Brenchley, A. Teske, C. H. House, and K.-U. Hinrichs. Heterotrophic Archaea dominate sedimentary subsurface ecosystems off Peru. *Proc. Natl. Acad. Sci. USA*, 103: 3846, 2006.

C. Binder, C. Feichtinger, H.J. Schmid, N. Thürey, W. Peukert, and U. Rüde. Simulation of the hydrodynamic drag of aggregated particles. *J. Colloid Interface Sci.*, 301:155, 2006.

J. R. Blake. A spherical envelope approach to ciliary propulsion. *J. Fluid Mech.*, 46:199, 1971.

J. R. Blake and M. A. Sleigh. Mechanics of ciliary locomotion. *Biol. Rev. Camb. Phil. Soc.*, 49:85, 1974.

S. Bleil, D. W. M. Marr, and C. Bechinger. Field-mediated self-assembly and actuation of highly parallel microfluidic devices. *Appl. Phys. Lett.*, 88:263515, 2006.

J. Branscomb and A. Alexeev. Designing ciliated surfaces that regulate deposition of solid particles. *Soft Matter*, 6:4066, 2010.

M. Braun and F. Cichos. Optically controlled thermophoretic trapping of single nano-objects. *ACS Nano*, 7:11200, 2013.

D. Bray. *Cell Movements*. Garland (New York), 2000.

C. Brennen and H. Winet. Fluid mechanics of propulsion by cilia and flagella. *Annu. Rev. Fluid Mech.*, 9:339, 1977.

I. Buttinoni, G. Volpe, F. Kümmel, G. Volpe, and C. Bechinger. Active Brownian motion tunable by light. *J. Phys.: Condens. Matter*, 24:284129, 2012.

C. R. Calladine. Construction of bacterial flagella. *Nature*, 255:121, 1975.

C. R. Calladine, B. F. Luisi, and J. V. Pratap. A 'mechanistic' explanation of the multiple helical forms adopted by bacterial flagellar filaments. *J. Mol. Biol.*, 425:914, 2013.

M. J. Carlile and A. W. L. Dudeney. Zonation in migrating magnetococci. *J. Gen. Microbiol.*, 139:1671, 1993.

J. Carlson, A. Jaffe, and A. Wiles, editors. *The Millennium Prize Problems*. Providence, RI: American Mathematical Society and Clay Mathematics Institute, 2006.

K. S. Chang and W. L. Olbricht. Experimental studies of the deformation and breakup of a synthetic capsule in steady and unsteady simple shear-flow. *J. Fluid Mech.*, 250:609, 1993.

S. Chapman. On the law of distribution of molecular velocities, and on the theory of viscosity and thermal conduction, in a non-uniform simple monatomic gas. *Philos. Trans. R. Soc. London*, 216:279, 1916.

C. Chapman-Andresen. Studies on the heavy spherical (refractive) bodies of freshwater Amoebae. I. Morphology and regeneration of HSBS in *Chaos carolinense*. *Carlsberg Res. Commun.*, 41:191, 1976.

N. W. Charon, G. R. Daughtry, R. S. McCuskey, and G. N. Franz. Microcinematographic analysis of tethered *Leptospira illini*. *J. Bacteriol.*, 160:1067, 1984.

S. Chattopadhyay, R. Moldovan, C. Yeung, and X. L. Wu. Swimming efficiency of bacterium *Escherichia coli*. *Proc. Natl. Acad. Sci. USA*, 103:13712, 2006.

H. Chen, S. Chen, and W. H. Matthaeus. Recovery of the NavierStokes equations using a lattice-gas Boltzmann method. *Phys. Rev. A*, 45:R5339, 1992.

S. Chen and G. D. Doolen. Lattice Boltzmann method for fluid flows. *Annu. Rev. Fluid Mech.*, 30:329, 1998.

S. Childress. *Mechanics of swimming and flying*. Cambridge University Press, 1981.

A. T. Chwang and T. Y. Wu. A note on the helical movement of micro-organisms. *Proc. R. Soc. Lond. B*, 178:327, 1971.

P. Collignon. Resistant *Escherichia coli*–we are what we eat. *Clin. Infect. Dis.*, 49:202, 2009.

M. F. Copeland and D. B. Weibel. Bacterial swarming: a model system for studying dynamic self-assembly. *Soft Matter*, 5:1174, 2009.

J. Cosson, P. Huitorel, and C. Gagnon. How spermatozoa come to be confined to surfaces. *Cell Motil. Cytoskel.*, 54:56, 2003.

J. W. Costerton, P. S. Stewart, and E. P. Greenberg. Bacterial biofilms: A common cause of persistent infections. *Science*, 284:1318, 1999.

H. Craighead. Future lab-on-a-chip technologies for interrogating individual molecules. *Nature*, 442:387, 2006.

N. C. Darnton and H. C. Berg. Force-extension measurements on bacterial flagella: triggering polymorphic transformations. *J. Bacteriol.*, 92:2230, 2007.

N. C. Darnton, L. Turner, S. Rojevsky, and H. C. Berg. On torque and tumbling in swimming *Escherichia coli*. *J. Bacteriol.*, 189:1756, 2007.

P. de Buyl and R. Kapral. Phoretic self-propulsion: a mesoscopic description of reaction dynamics that powers motion. *Nanoscale*, 5:1337, 2013.

J. K. G. Dhont. *An Introduction to Dynamics of Colloids*. Elsevier Science B.V., 1996.

W. R. DiLuzio, L. Turner, M. Mayer, P. Garstecki, D. B. Weibel, H. C. Berg, and G. M. Whitesides. *Escherichia coli* swim on the right-hand side. *Nature*, 435: 1271, 2005.

M. Doi and S. F. Edwards. *The Theory of Polymer Dynamics*. Oxford University Press, U.S.A., 1988.

K. Drescher, K. C. Leptos, I. Tuval, T. Ishikawa, T. J. Pedley, , and R. E. Goldstein. Dancing *Volvox*: hydrodynamic bound states of swimming algae. *Phys. Rev. Lett.*, 102:168101, 2009.

K. Drescher, R. E. Goldstein, N. Michel, M. Polin, and I. Tuval. Direct measurement of the flow field around swimming microorganisms. *Phys. Rev. Lett.*, 105: 168101, 2010.

R. Dreyfus, J. Baudry, M. L. Roper, M. Fermigier, H. A. Stone, and J. Bibette. Microscopic artificial swimmers. *Nature*, 437:862, 2005.

D. J. Earl, C. M. Pooley, J. F. Ryder, I. Bredberg, and J. M. Yeomans. Modeling microscopic swimmers at low Reynolds number. *J. Chem. Phys.*, 126:064703, 2007.

M. Eisenbach and L. C. Giojalas. Sperm guidance in mammals: an unpaved road to the egg. *Nat. Rev. Mol. Cell. Biol.*, 7:276, 2006.

J. El-Ali, P. K. Sorger, and K. F. Jensen. Cells on chips. *Nature*, 442:403, 2006.

J. Elgeti and G. Gompper. Emergence of metachronal waves in cilia arrays. *Proc. Natl. Acad. Sci. USA*, 110:4470, 2013.

J. Elgeti, R. G. Winkler, and G. Gompper. Physics of microswimmers–single particle motion and collective behavior: a review. *Rep. Prog. Phys.*, 78:056601, 2015.

D. Enskog. *Kinetische Theorie der Vorgänge in mässig verdünnten Gasen*. PhD thesis, Uppsala, Sweden, 1917.

A. A. Evans, S. E. Spagnolie, and E. Lauga. Stokesian jellyfish: viscous locomotion of bilayer vesicles. *Soft Matter*, 6:1737, 2010.

A. Farutin, S. Rafaï, D. K. Dysthe, A. Duperray, P. Peyla, and C. Misbah. Amoeboid swimming: A generic self-propulsion of cells in fluids by means of membrane deformations. *Phys. Rev. Lett.*, 111:228102, 2013.

L. J. Fauci and A. Mcdonald. Sperm motility in the presence of boundaries. *Bull. Math. Biol.*, 57:679, 1995.

H. Faxén. Der Widerstand gegen die Bewegung einer starren Kugel in einer zähen Flüssigkeit, die zwischen zwei parallelen ebenen wänden eingeschlossen ist. *Ann. Phys. (Berlin)*, 373:89, 1922.

C. Feichtinger, S. Donath, H. Köstler, J. Götz, and U. Rüde. WaLBerla: HPC software design for computational engineering simulations. *J. Comput. Sci.*, 2: 105, 2011.

B. U. Felderhof. The swimming of animalcules. *Phys. Fluids*, 18:063101, 2006.

H. S. Fisher, L. Giomi, H. E. Hoekstra, and L. Mahadevan. The dynamics of sperm cooperation in a competitive environment. *Proc. R. Soc. B*, 281:20140296, 2014.

S. Fournier-Bidoz, A. C. Arsenault, I. Manners, and G. A. Ozin. Synthetic self-propelled nanorotors. *Chem. Commun.*, 441:3, 2005.

B. M. Friedrich and F. Jülicher. Chemotaxis of sperm cells. *Proc. Natl. Acad. Sci. USA*, 104:13256, 2007.

B. M. Friedrich and F. Jülicher. Flagellar synchronization independent of hydrodynamic interactions. *Phys. Rev. Lett.*, 109:138102, 2012.

B. M. Friedrich, I. H. Riedel-Kruse, J. Howard, and F. Jülicher. High-precision tracking of sperm swimming fine structure provides strong test of resistive force theory. *J. Exp. Biol.*, 213:1226, 2010.

U. Frisch, B. Hasslacher, and Y. Pomeau. Lattice-gas automata for the Navier-Stokes equations. *Phys. Rev. Lett.*, 56:1505, 1986.

U. Frisch, D. d'Humières, B. Hasslacher, P. Lallemand, Y. Pomeau, and J.-P. Rivet. Lattice gas hydrodynamics in two and three dimensions. *Complex System*, 1:649, 1987.

P. D. Frymier, R. M. Ford, H. C. Berg, and P. T. Cummings. Three-dimensional tracking of motile bacteria near a solid planar surface. *Proc. Natl. Acad. Sci. USA*, 92:6195, 1995.

L. Gervais, N. de Rooij, and E. Delamarche. Microfluidic chips for point-of-care immunodiagnostics. *Adv. Mater.*, 23:H151, 2011.

S. Ghorai and N. A. Hill. Development and stability of gyrotactic plumes in bioconvection. *J. Fluid Mech.*, 400:1, 1999.

I. Ginzburg, F. Verhaeghe, and D. dHumières. Two-relaxation-time lattice Boltzmann scheme: about parametrization, velocity, pressure and mixed boundary conditions. *Commun. Comput. Phys.*, 3:427, 2008.

S. Goldstein and N. Charon. Multiple-exposure photographic analysis of a motile spirochete. *Proc. Natl. Acad. Sci. USA*, 87:4895, 1990.

R. Golestanian. Three-sphere low-reynolds-number swimmer with a cargo container. *Eur. Phys. J. E*, 25:1, 2008.

R. Golestanian and A. Ajdari. Analytic results for the three-sphere swimmer at low Reynolds number. *Phys. Rev. E*, 77:036308, 2008.

R. Golestanian, T. B. Liverpool, and A. Ajdari. Propulsion of a molecular machine by asymmetric distribution of reaction products. *Phys. Rev. Lett.*, 94:220801, 2005.

J. Götz, K. Iglberger, M. Stürmer, and U. Rüde. Direct numerical simulation of particulate flows on 294912 processor cores. In *2010 ACM/IEEE International Conference for High Performance Computing, Networking, Storage and Analysis*, page 1. IEEE, 2010.

B. A. Grzybowsk, H. A. Stone, and G. M. Whitesides. Dynamic self-assembly of magnetized, millimetre-sized objects rotating at a liquid-air interface. *Nature*, 405:1033, 2000.

D. C. Guell, H. Brenner, R. B. Frankel, and H. Hartman. Hydrodynamic forces and band formation in swimming magnetotactic bacteria. *J. Theor. Biol.*, 135: 525, 1988.

J. Happel and H. Brenner. *Low Reynolds Number Hydrodynamics*. Prentice-Hall Inc., 1965.

J. Hardy, O. de Pazzis, and Y. Pomeau. Molecular dynamics of a classical lattice gas: transport properties and time correlation functions. *Phys. Rev. A*, 13:1949, 1976.

M. Hatsumi and K.-I. Wakahama. The sperm length and the testis length in *Drosophila nasuta* subgroup. *Japan J. Genet.*, 61:241, 1986.

F. J. Higuera and J. Jimenez. Boltzmann approach to lattice gas simulations. *Europhys. Lett.*, 9:663, 1989.

T. Hiraiwa, K. Shitara, and T. Ohta. Dynamics of a deformable self-propelled particle in three dimensions. *Soft Matter*, 7:3083, 2011.

J. R. Howse, R. A. L. Jones, A. J. Ryan, T. Gough, R. Vafabakhsh, and R. Golestanian. Self-motile colloidal particles: from directed propulsion to random walk. *Phys. Rev. Lett.*, 99:048102, 2007.

S. Hudault, J. Guignot, and A. L. Servin. *Escherichia coli* strains colonising the gastrointestinal tract protect germfree mice against *Salmonella typhimurium* infection. *Gut*, 49:47, 2001.

Y. Hyon, T. Powers, R. Stocker, and H. Fu. The wiggling trajectories of bacteria. *J. Fluid Mech.*, 705:58, 2012.

K. Iglberger. *Software Design of a Massively Parallel Rigid Body Framework*. PhD thesis, Computer Science Department, University Erlangen-Nürnberg, 2010.

K. Iglberger, N. Thürey, and U. Rüde. Simulation of moving particles in 3d with the lattice Boltzmann method. *Comput. Math. Appl.*, 55:1461, 2008.

K. Ishimoto and E. A. Gaffney. Squirmer dynamics near a boundary. *Phys. Rev. E*, 88:062702, 2013.

JianFeng and S. K. Cho. Mini and micro propulsion for medical swimmers. *Micromachines*, 5:97, 2014.

H. R. Jiang, N. Yoshinaga, and M. Sano. Active motion of Janus particle by self-thermophoresis in defocused laser beam. *Phys. Rev. Lett.*, 105:268302, 2010.

G. E. Kaiser and R. N. Doetsch. Enhanced translational motion of *Leptospira* in viscous environments. *Nature*, 255:656, 1975.

J. Kallmeyer, R. Pockalny, R. R. Adhikari, D. C. Smith, and S. DHondt. Global distribution of microbial abundance and biomass in subseafloor sediment. *Proc. Natl. Acad. Sci. USA*, 109:16213, 2012.

V. Kantsler, J. Dunkel, M. Polin, and R. E. Goldstein. Ciliary contact interactions dominate surface scattering of swimming eukaryotes. *Proc. Natl. Acad. Sci. USA*, 110:1187, 2013.

D. F. Katz. Propulsion of microorganisms near solid boundaries. *J. Fluid Mech.*, 64:33, 1974.

D. F. Katz, J. R. Blake, and S. L. Paverifontana. Movement of slender bodies near plane boundaries at low Reynolds number. *J. Fluid Mech.*, 72:529, 1975.

B. U. Kaupp, N. D. Kashikar, and I. Weyand. Mechanisms of sperm chemotaxis. *Annu. Rev. Physiol.*, 70:93, 2008.

A. Kawska, K. Carvalho, J. Manzi, R. Boujemaa-Paterski, L. Blanchoin, J. L. Martiel, and C. Sykes. How actin network dynamics control the onset of actin-based motility. *Proc. Natl. Acad. Sci. USA*, 109:14440, 2012.

A. Keissner and C. Brücker. Directional fluid transport along artificial ciliary surfaces with base-layer actuation of counter-rotating orbital beating patterns. *Soft Matter*, 8:5342, 2012.

S. Kessler, R. Finken, and U. Seifert. Swinging and tumbling of elastic capsules in shear flow. *J. Fluid Mech.*, 605:207, 2008.

Y. W. Kim and R. R. Netz. Pumping fluids with periodically beating grafted elastic filaments. *Phys. Rev. Lett.*, 96:158101, 2006.

A. Klitorinos, P. Noble, R. Siboo, and E. C. S. Chan. Viscosity-dependent locomotion of oral spirochetes. *Oral Microbiol. Immunol.*, 8:242, 1993.

J. M. V. A. Koelman. A simple lattice Boltzmann scheme for NavierStokes fluid flow. *Europhys. Lett.*, 15:603, 1991.

C. Körner, T. Pohl, U. Rüde, N. Thürey, and T. Zeiser. Parallel lattice Boltzmann methods for CFD applications. In A.M. Bruaset and A. Tveito, editors, *Numerical Solution of Partial Differential Equations on Parallel Computers*, volume 51 of *LNCSE*, chapter 5, page 439. Springer, 2005.

S. Koyasu and Y. Shirakihara. *Caulobacter crescentus* flagellar filament has a right-handed helical form. *J. Mol. Biol.*, 173:125, 1984.

M. Kreutz, T. Stoeck, and W. Foissner. Morphological and molecular characterization of *Paramecium* (*Viridoparamecium* nov. subgen.) *chlorelligerum* Kahl 1935 (Ciliophora). *J. Eukaryot. Microbiol.*, 59:548, 2012.

T. Krüger, F. Varnik, and D. Raabe. Efficient and accurate simulations of deformable particles immersed in a fluid using a combined immersed boundary lattice Boltzmann finite element method. *Comput. Math. Appl.*, 61:3485, 2011.

T. Krüger, S. Frijters, F. Günther, B. Kaoui, , and J. Harting. Numerical simulations of complex fluid-fluid interface dynamics. *Eur. Phys. J. Special Topics*, 222:177, 2013.

T. Krüger, B. Kaoui, and J. Harting. Interplay of inertia and deformability on rheological properties of a suspension of capsules. *J. Fluid Mech.*, 751:725, 2014.

R. Kusters, T. van der Heijden, B. Kaoui, J. Harting, and C. Storm. Forced transport of deformable containers through narrow constrictions. *Phys. Rev. E*, 90:033006, 2014.

E. Lauga and D. Bartolo. No many-scallop theorem: collective locomotion of reciprocal swimmers. *Phys. Rev. E*, 78:030901, 2008.

E. Lauga and T. R. Powers. The hydrodynamics of swimming microorganisms. *Rep. Prog. Phys.*, 72:096601, 2009.

E. Lauga, W. R. DiLuzio, G. M. Whitesides, and H. A. Stone. Swimming in circles: motion of bacteria near solid boundaries. *Biophys. J.*, 90:400, 2006.

M. Leoni, J. Kotar, B. Bassetti, P. Cicuta, and M. C. Lagomarsino. A basic swimmer at low Reynolds number. *Soft Matter*, 5:472, 2009.

K. C. Leptos, K. Y. Wan, M. Polin, I. Tuval, A. I. Pesci, and R. E. Goldstein. Antiphase synchronization in a flagellar-dominance mutant of *Chlamydomonas*. *Phys. Rev. Lett.*, 111:158101, 2013.

A. M. Leshansky. Enhanced low-Reynolds-number propulsion in heterogeneous viscous environments. *Phys. Rev. E*, 80:051911, 2009.

A. M. Leshansky, O. Kenneth, O. Gat, and J. E. Avron. A frictionless microswimmer. *New J. Phys.*, 9:145, 2007.

X. Z. Li, D. Barthès-Biesel, and A. Helmy. Large deformations and burst of a capsule freely suspended in an elongational flow. *J. Fluid Mech.*, 187:179, 1988.

M. J. Lighthill. On the squirming motion of nearly spherical deformable bodies through liquids at very small Reynolds numbers. *Comm. Pure Appl. Math.*, 5: 109, 1952.

J. S. Lipp, Y. Morono, F. Inagaki, and K.-U. Hinrichs. Significant contribution of Archaea to extant biomass in marine subsurface sediments. *Nature*, 454:991, 2008.

L.-S. Luo. The lattice-gas and lattice Boltzmann methods: past, present, and future. In J.-H. Wu and Z.-J. Zhu, editors, *Proceedings of the International Conference on Applied Computational Fluid Dynamics, Beijing, China*, page 52, 2000.

H. Machemer. Ciliary activity and origin of metachrony in paramecium: effects of increased viscosity. *J. Exp. Biol.*, 57:239, 1972.

R. M. Macnab. Bacterial flagella rotating in bundles: a study in helical geometry. *Proc. Natl. Acad. Sci. USA*, 74:221, 1977.

Y. Magariyama and S. Kudo. A mathematical explanation of an increase in bacterial swimming speed with viscosity in linear-polymer solutions. *Biophys. J.*, 83:733, 2002.

H. Masoud and A. Alexeev. Harnessing synthetic cilia to regulate motion of microparticles. *Soft Matter*, 7:8702, 2011.

G. R. McNamara and G. Zanetti. Use of the Boltzmann equation to simulate lattice-gas automata. *Phys. Rev. Lett.*, 61:2332, 1988.

S. S. Merchant, J. Kropat, B. Liu, J. Shaw, and J. Warakanont. TAG, you're it! *Chlamydomonas* as a reference organism for understanding algal triacylglycerol accumulation. *Curr. Opin. Biotech.*, 23:352, 2012.

C. Misbah. Vacillating breathing and tumbling of vesicles under shear flow. *Phys. Rev. Lett.*, 96:28104, 2006.

G. E. Murphy, E. G. Matson, J. R. Leadbetter, H. C. Berg, and G. J. Jensen. Novel ultrastructures of *Treponema primitia* and their implications for motility. *Mol. Microbiol.*, 67:1184, 2008.

A. Najafi and R. Golestanian. Simple swimmer at low Reynolds number: Three linked spheres. *Phys. Rev. E*, 69:062901, 2004.

A. Najafi and R. Golestanian. Coherent hydrodynamic coupling for stochastic swimmers. *Europhys. Lett.*, 90:68003, 2010.

S. Nakamura, Y. Adachi, T. Goto, and Y. Magariyama. Improvement in motion efficiency of the spirochete *Brachyspira pilosicoli* in viscous environments. *Biophys. J.*, 90:3019, 2006.

B. J. Nelson, I. K. Kaliakatsos, and J. J. Abbott. Microrobots for minimally invasive medicine. *Annu. Rev. Biomed. Eng.*, 12:55, 2010.

A. Oberbeck. Über stationare Flüssigkeitsbewegungen mit Berücksichtigung der inneren Reibung. *J. reine angew. Math.*, 81:62, 1876.

F. Y. Ogrin, P. G. Petrov, and C. P. Winlove. Ferromagnetic microswimmers. *Phys. Rev. Lett.*, 100:218102, 2008.

T. Ohta and T. Ohkuma. Deformable self-propelled particles. *Phys. Rev. Lett.*, 102:154101, 2009.

K. I. Okamoto and Y. Nakaoka. Reconstitution of metachronal waves in ciliated cortical sheets of *Paramecium*. II. Asymmetry of the ciliary movements. *J. Exp. Biol.*, 192:73, 1994.

C. W. Oseen. *Neuere Methoden und Ergebnisse in der Hydrodynamik*. Leipzig: Akademische Verlagsgesellschaft, 1927.

N. Osterman and A. Vilfan. Finding the ciliary beating pattern with optimal efficiency. *Proc. Natl. Acad. Sci. USA*, 108:15727, 2011.

J. Pande and A.-S. Smith. Forces and shapes as determinants of micro-swimming: effect on synchronisation and the utilisation of drag. *Soft Matter*, 11:2364, 2015.

J. Pande, L. Merchant, T. Krüger, J. Harting, and A.-S. Smith. Effect of body deformability on microswimming (under review). 2016a.

J. Pande, L. Merchant, T. Krüger, J. Harting, and A.-S. Smith. Setting the pace of microswimmers: when increasing viscosity speeds up self-propulsion (under review). 2016b.

J. Pande*, K. Pickl*, O. Trosman, U. Rüde, and A.-S. Smith. Microswimming with inertia (under review). 2016.

D. Patra, S. Sengupta, W. Duan, H. Zhang, R. Pavlick, and A. Sen. Intelligent, self-powered, drug delivery systems. *Nanoscale*, 5:1273, 2013.

T. J. Pedley, N. A. Hill, and J. O. Kessler. The growth of bioconvection patterns in a uniform suspension of gyrotactic micro-organisms. *J. Fluid Mech.*, 195:223, 1988.

F. Perrin. Mouvement brownien d'un ellipsoïde - I. Dispersion diélectrique pour des molécules ellipsoïdales. *J. Phys. Radium*, 5:497, 1934.

K. Pickl. *Fully Resolved Simulation of Self-propelled Microorganisms on Supercomputers*. PhD thesis, Computer Science Department, Friedrich-Alexander-University Erlangen-Nürnberg, 2016.

K. Pickl, J. Götz, K. Iglberger, J. Pande, K. Mecke, A.-S. Smith, and U. Rüde. All good things come in threes–three beads learn to swim with lattice Boltzmann and a rigid body solver. *J. Comput. Sci.*, 3:374, 2012.

K. Pickl, J. Pande, H. Köstler, U. Rüde, and A.-S. Smith. Fully resolved simulations of single- and many-swimmer configurations of the three-sphere microswimmer (under review). 2016.

T. Pohl, M. Kowarschik, J. Wilke, K. Iglberger, and U. Rüde. Optimization and profiling of the cache performance of parallel lattice Boltzmann codes. *Parallel Processing Lett.*, 13:549, 2003.

C. M. Pooley and J. M. Yeomans. Lattice Boltzmann simulation techniques for simulating microscopic swimmers. *Comput. Phys. Commun.*, 179:159, 2008.

C. M. Pooley, G. P. Alexander, and J. M. Yeomans. Hydrodynamic interaction between two swimmers at low Reynolds number. *Phys. Rev. Lett.*, 99:228103, 2007.

M. N. Popescu, S. Dietrich, M. Tasinkevych, and J. Ralston. Phoretic motion of spheroidal particles due to self-generated solute gradients. *Eur. Phys. J. E*, 31: 351, 2010.

E. M. Purcell. Life at low Reynolds number. *Am. J. Phys.*, 45:3, 1977.

E. M. Purcell. The efficiency of propulsion by a rotating flagellum. *Proc. Natl. Acad. Sci. USA*, 94:11307, 1997.

Y. H. Qian, D. d'Humières, and P. Lallemand. Lattice BGK models for Navier-Stokes equation. *Europhys. Lett.*, 17:479, 1992.

D. L. J. Quicke, S. N. Ingram, H. S. Baillie, and P. V. Gaitens. Sperm structure and ultrastructure in hymenoptera (insecta). *Zoologica Scr.*, 21:381, 1992.

M. Ramia, D. L. Tullock, and N. Phan-Thien. The role of hydrodynamic interaction in the locomotion of microorganisms. *Biophys. J.*, 65:755, 1993.

A. J. Reynolds. The swimming of minute organisms. *J. Fluid Mech.*, 23:241, 1965.

I. H. Riedel, K. Kruse, and J. Howard. A self-organized vortex array of hydrodynamically entrained sperm cells. *Science*, 309:300, 2005.

L. Rothschild. Non-random distribution of bull spermatozoa in a drop of sperm suspension. *Nature*, 198:1221, 1963.

J. Rotne and S. Prager. Variational treatment of hydrodynamic interaction in polymers. *J. Chem. Phys.*, 50:4831, 1969.

N. Rott. Note on the history of the Reynolds number. *Annu. Rev. Fluid Mech.*, 22: 1, 1990.

J. D. Ruby and N. W. Charon. Effect of temperature and viscosity on the motility of the spirochete *Treponema denticola. FEMS Microbiol. Lett.*, 169:251, 1998.

G. Rückner and R. Kapral. Chemically powered nanodimers. *Phys. Rev. Lett.*, 98: 150603, 2007.

E. K. Sackmann, A. L. Fulton, and D. J. Beebe. The present and future role of microfluidics in biomedical research. *Nature*, 507:181, 2014.

M. Salathe. Regulation of mammalian ciliary beating. *Annu. Rev. Physiol.*, 69: 401, 2007.

T. Sanchez, D. Welch, D. Nicastro, and Z. Dogic. Cilia-like beating of active microtubule bundles. *Science*, 333:456, 2011.

W. R. Schneider and R. N. Doetsch. Effect of viscosity on bacterial motility. *J. Bacteriol.*, 117:696, 1974.

J. Scogna, J. Olkowski, N. Fatema, P. Parameswaran, and V. Dhillon. Biologically inspired robotic microswimmers. In *2011 IEEE 37th Annual Northeast Bioengineering Conference (NEBEC)*, page 1, 2011.

J. W. Shaevitz, J. Y. Lee, and D. A. Fletcher. Spiroplasma swim by a processive change in body helicity. *Cell*, 122:941, 2005.

J. G. Shoesmith. The measurement of bacterial motility. *J. Gen. Microbiol.*, 22: 528, 1960.

R. Skalak, A. Tozeren, R. P. Zarda, and s. Chien. Strain energy function of red blood cell membranes. *Biophys. J.*, 13:245, 1973.

M. A. Sleigh, J. R. Blake, and N. Liron. The propulsion of mucus by cilia. *Am. Rev. Resp. Dis.*, 137:726, 1988.

D. J. Smith, J. R. Blake, and E. A. Gaffney. Fluid mechanics of nodal flow due to embryonic primary cilia. *J. R. Soc. Interface*, 5:567, 2008.

K. Son, J. S. Guasto, and R. Stocker. Bacteria can exploit a flagellar buckling instability to change direction. *Nat. Phys.*, 9:494, 2013.

S. E. Spagnolie and E. Lauga. Hydrodynamics of self-propulsion near a boundary: predictions and accuracy of far-field approximations. *J. Fluid Mech.*, 700:105, 2012.

S. Succi. *The Lattice Boltzmann Equation - For Fluid Dynamics and Beyond*. Clarendon Press, 2001.

S. L. Tamm and G. A. Horridge. Relation between orientation of central fibrils and direction of beat in cilia of opalina. *Proc. R. Soc. Lond. B*, 175:219, 1970.

Y. G. Tao and R. Kapral. Design of chemically propelled nanodimer motors. *J. Chem. Phys.*, 128:164518, 2008.

G. Taylor. Analysis of the swimming of microscopic organisms. *Proc. R. Soc. Lond. A*, 209:447, 1951.

G. Taylor. Low Reynolds Number Flows. *National Committe For Fluid Mechanics Films*, http://web.mit.edu/hml/ncfmf.html, 1967.

J. Throndsen. Flagellates of Norwegian coastal waters. *Norwegian J. Botany*, 16: 161, 1969.

P. Tierno, R. Golestanian, I. Pagonabarraga, and F. Sagués. Magnetically actuated colloidal microswimmers. *J. Phys. Chem. B*, 112:16525, 2008a.

P. Tierno, R. Golestanian, I. Pagonabarraga, and F. Sagués. Controlled swimming in confined fluids of magnetically actuated colloidal rotors. *Phys. Rev. Lett.*, 101:218304, 2008b.

O. Trosman. Analytical study of the bead-spring microswimmer model under the influence of inertia. Master's thesis, Friedrich-Alexander-University Erlangen-Nürnberg, 2016.

L. Turner, W. S. Ryu, and H. C. Berg. Real-time imaging of fluorescent flagellar filaments. *J. Bacteriol.*, 182:2793, 2000.

N. Ueki, T. Ide, S. Mochiji, Y. Kobayashi, R. Tokutsu, N. Ohnishi, K. Yamaguchi, S. Shigenobu, K. Tanaka, J. Minagawa, T. Hisabori, M. Hirono, and K. Wakabayashi. Eyespot-dependent determination of the phototactic sign in emphChlamydomonas reinhardtii. *Proc. Natl. Acad. Sci. USA*, 113:5299, 2016.

M. A. S. Vigeant and R. M. Ford. Interactions between motile *Escherichia coli* and glass in media with various ionic strengths, as observed with a three-dimensional tracking microscope. *Appl. Environ. Microbiol.*, 63:3474, 1997.

M. Vilfan, A. Potočnik, B. Kavčič, N. Osterman, I. Poberaj, A. Vilfan, and D. Babič. Self-assembled artificial cilia. *Proc. Natl. Acad. Sci. USA*, 107: 1844, 2010.

R. Vogel and H. Stark. Force-extension curves of bacterial flagella. *Eur. Phys. J. E*, 33:259, 2010.

R. Vogel and H. Stark. Rotation-induced polymorphic transitions in bacterial flagella. *Phys. Rev. Lett.*, 110:158104, 2013.

C. A. Wanke. To know *Escherichia coli* is to know bacterial diarrheal disease. *Clin. Infect. Dis.*, 32:1710, 2001.

G. Wellein, T. Zeiser, S. Donath, and G. Hager. On the single processor performance of simple lattice Boltzmann kernels. *Comput. & Fluids*, 35:910, 2005.

M. Werner and L. W. Simmons. Insect sperm motility. *Biol. Rev.*, 83:191, 2008.

W. B. Whitman, D. C. Coleman, and W. J. Wiebe. Prokaryotes: The unseen majority. *Proc. Natl. Acad. Sci. USA*, 95:6578, 1998.

B. J. Williams, S. V. Anand, J. Rajagopalan, and M. T. A. Saif. A self-propelled biohybrid swimmer at low Reynolds number. *Nat. Commun.*, 5:3081, 2014.

H. Winet, G. S. Bernstein, and J. Head. Spermatozoon tendency to accumulate at walls is strongest mechanical response. *J. Androl.*, 5:19, 1984.

D. M. Woolley. Motility of spermatozoa at surfaces. *Reproduction*, 126:259, 2003.

H. Wu, M. Thiébaud, W. F. Hu, A. Farutin, S. Rafaï, M. C. Lai, P. Peyla, and C. Misbah. Amoeboid motion in confined geometry. *Phys. Rev. E*, 92: 050701(R), 2015.

P. Yager, T. Edwards, E. Fu, K. Helton, K. Nelson, M. R. Tam, and B. H. Weigl. Microfluidic diagnostic technologies for global public health. *Nature*, 442:412, 2006.

L. Y. Yeo, H.-C. Chang, P. P. Y. Chan, and J. R. Friend. Microfluidic devices for bioapplications. *Small*, 7:12, 2011.

D. Yu, R. Mei, L.-S. Luo, and W. Shyy. Viscous flow computations with the method of lattice Boltzmann equation. *Prog. Aero. Sci.*, 39:329, 2003.

R. Zargar, A. Najafi, and M. Miri. Three-sphere low-Reynolds-number swimmer near a wall. *Phys. Rev. E*, 80:026308, 2009.

156

# Part IV

# Miscellaneous

# List of publications

## Publications included in this thesis

- **P1:** **J. Pande** and A.-S. Smith. Forces and shapes as determinants of micro-swimming: effect on synchronisation and the utilisation of drag. *Soft Matter*, 11:2364, 2015.

- **P2:** **J. Pande**, L. Merchant, T. Krüger, J. Harting, and A.-S. Smith. Setting the pace of microswimmers: when increasing viscosity speeds up self-propulsion. Submitted to *Proc. Natl. Acad. Sci. USA*. 2016.

- **P3:** **J. Pande**, L. Merchant, T. Krüger, J. Harting, and A.-S. Smith. Effect of body deformability on microswimming. Submitted to *Soft Matter*. 2016.

- **P4:** **J. Pande\***, K. Pickl\*, O. Trosman, U. Rüde, and A.-S. Smith. Microswimming with inertia. Submitted to *New J. Phys.* 2016.

- **P5:** K. Pickl, **J. Pande**, H. Köstler, U. Rüde, and A.-S. Smith. Fully resolved simulations of single- and many-swimmer configurations of the three-sphere microswimmer. Submitted to *J. Phys.: Condens. Matter*. 2016.

## Publications not included in this thesis

- **P6:** K. Pickl, J. Götz, K. Iglberger, **J. Pande**, K. Mecke, A.-S. Smith, and U. Rüde. All good things come in threes–three beads learn to swim with lattice Boltzmann and a rigid body solver. *J. Comput. Sci.*, 3:374, 2012.

- **P7:** M. Cvitković, A.-S. Smith, and **J. Pande**. General asymptotic expansions of the hypergeometric function with two large parameters. Submitted to *J. Phys. A: Math. Theor.* 2016.

# Curriculum Vitae

## PERSONAL DETAILS

**Name**      Jayant Pande

**Birth Date**      11 October 1987

**Nationality**      Indian

## SKILLS

**Technical Skills**      Mathematica, Java, C++, Bash, Adobe Illustrator, Inkscape, Latex, ParaView, Windows, GNU/Linux

**Languages**      English, Kumaoni and Hindi – native speaker
French and German – near-fluent (C1 level on the CEFR scale)

## EDUCATION

**PhD Study**
Jan. 2012 – present

**PULS GROUP, FAU ERLANGEN-NÜRNBERG, GERMANY**
Supervisor: Prof. Dr. Ana-Sunčana Smith
Thesis: *Analytical and numerical study of microswimming with the bead-spring model*

**Undergraduate Study**
Jul. 2005 – Jul. 2010

**MASTER OF SCIENCE (INTEGRATED) IN PHYSICS, INDIAN INSTITUTE OF TECHNOLOGY, KANPUR, INDIA**

Thesis: *Study of the thermal lens effect in methanol-ethanol mixtures*, under the supervision of Dr. Debabrata Goswami, Department of Chemistry, Indian Institute of Technology, Kanpur, India

## WORK EXPERIENCE

**Research Assistant**
Oct. 2010 – Jan. 2012

**CLUSTER OF EXCELLENCE: ENGINEERING OF ADVANCED MATERIALS, ERLANGEN, GERMANY**

## STUDENT CO-SUPERVISION

Jun. 2016 – present      **Master's thesis:** Thomas Scheel, FAU Erlangen-Nürnberg
Project title: *Effect of confinement on the swimming of bead-spring microswimmers*

Oct. 2015 – present      **Master's thesis:** Oleg Trosman, FAU Erlangen-Nürnberg
Project title: *Analytical perturbative model for bead-spring microswimmers with inertia*

Jun. 2014 – Aug. 2014      **DAAD RISE Programme:** Laura Merchant, University of St. Andrews, Scotland
Project title: *Swimming at the micro-scale*

Jan. 2013 – Apr. 2013      **Bachelor's thesis:** Thomas Kiendl and Matthias Späth (joint thesis), FAU Erlangen-Nürnberg
Project title: *Simulations of microswimmer clusters*

## TEACHING DUTIES

2010 – 2015     **Teaching Assistant** for the courses **Electrodynamics** (Winter 2010-11 and Winter 2011-12) and **Quantum Mechanics** (Summer 2012 and Winter 2014-15), in the Department of Physics, FAU Erlangen-Nürnberg

## INTERNATIONAL RESEARCH STAYS

Apr. 2014 – May 2014     **MESOSCOPIC TRANSPORT PHENOMENA GROUP, EINDHOVEN UNIVERSITY OF TECHNOLOGY, THE NETHERLANDS**
Collaborator: Prof. Dr. Jens Harting
Project: *Study and simulation of deformable bead-spring microswimmer models*

May 2009 – Jul. 2009     **LABORATOIRE LEPRINCE-RINGUET, ECOLE POLYTECHNIQUE, PALAISEAU CEDEX, FRANCE**
Supervisor: Dr. Vincent Boudry
Project: *Study of the events inside a semi-digital hadronic calorimeter*

## CONFERENCES AND WORKSHOPS

### Talks

| | |
|---|---|
| Mar. 2016 | German Physical Society Spring Meeting, Regensburg, Germany |
| Jul. 2015 | Discrete Simulation of Fluid Dynamics, Edinburgh, Scotland |
| Mar. 2015 | German Physical Society Spring Meeting, Berlin, Germany |
| Jul. 2014 | Dynacaps 2014: Dynamics of Capsules, Vesicles and Cells in Flow, Compiègne, France |
| May 2014 | Soft Matter Meeting, Amsterdam, The Netherlands |
| Mar. 2014 – Apr. 2014 | German Physical Society Spring Meeting, Dresden, Germany |
| Mar. 2013 | EAM Winter School, Kirchberg, Austria |
| Mar. 2013 | German Physical Society Spring Meeting, Regensburg, Germany |

### Posters

| | |
|---|---|
| Jul. 2015 | Physics of Emergent Behaviour II: From Molecules to Planets, London, England |
| May 2015 | COST Training Summer School "Interaction of microscopic structures and organisms with fluid flows", Udine, Italy |
| Apr. 2015 | Microswimmers – From Bulk to Interfaces, Bordeaux, France |
| Feb. 2015 | Symposium Physics and Medicine, Erlangen, Germany |
| Dec. 2013 | Physics and Biology of Directed Movements of Cells and Organisms, Bad Honnef, Germany |
| Sep. 2013 | International Soft Matter Conference, Rome, Italy |
| Sep. 2012 | Forces and Flow in Biological Systems, Bad Honnef, Germany |
| Sep. 2012 | |
| Jun. 2012 | Physics of Cells – From Soft to Living Matter, Hyères, France |

162

# Statutory declaration – Ehrenwörtliche Erklärung

Ich erkläre hiermit, dass ich diese Arbeit selbstständig verfasst und keine anderen als die angegebenen Quellen und Hilfsmittel verwendet habe.

Erlangen, den 05. August 2016

Jayant Pande

161

164

# Acknowledgements

I would like to take a few pages to try to express my heartfelt gratitude to a number of people and organizations that have had a direct and indelible impact on my doctoral life and the work presented here (this being the only place where I find it legitimate and appropriate to shed the garb of the collective 'we' that otherwise cloaks all my references to the self in this work). My first and foremost expression of thanks is to my supervisor, Prof. Dr. Ana-Sunčana Smith. There is nothing I could say which would adequately convey the respect, gratitude and fondness I feel, and I fear I must limit myself to a meager and insufficient 'Thank you'– Thank you for giving me this project, for taking me under your wing, for showing me, bit-by-bit, all the facets of the scientific life and how to couple it successfully to one's wider existence, for being an inexhaustible source of wisdom, positivity and strength, for constantly motivating, pushing, cajoling and encouraging me, for showing patience, for being equal parts friend and boss, for never ceasing to amaze me with short but crucial insights into innumerable aspects of my work, for running a wonderful group which it has been my scarcely-believable fortune to be a part of, for being singly most responsible for these last few years having been the most memorable of my life. Thank you for everything.

Next I would like to acknowledge the funding that I have received throughout my stay, from the Cluster of Excellence: Engineering of Advanced Materials (EAM), the European Research Council (ERC), and the Kompetenznetzwerk für Technisch-Wissenschaftliches Hoch- und Höchstleistungsrechnen in Bayern (KONWIHR).

I thank also Prof. Dr. Klaus Mecke and the entire Theorie I (theoretical physics I) group at my university (FAU), for giving me the opportunity to work in and learn from a world-class group of physicists. It has been a very valuable education, not only in physics, but also in scientific comportment and practices, and, last but

tremendous help in all administrative matters provided by the Welcome Centre in Erlangen during my first year here.

I have always thought that teaching something is the best way to deepen one's own understanding of it, and I am glad to have had this belief reinforced by the various classes for which I was a teaching assistant, and especially by the different Bachelor's and Master's students who have worked with me on their projects and theses. In particular I would like to acknowledge the research performed by Laura Merchant in her RISE program project in our group under the auspices of the DAAD academic exchange service, and by Oleg Trosman in his Master's project, both of whose efforts have found their way in some form into this thesis. Apart from the scientific value of their work, supervising both, as indeed all the others, was an enjoyable and eye-opening experience and I am much the richer for it.

Many thanks to the entire MTP group at the Eindhoven University of Technology for making my six-week stay there in the summer of 2014 a fruitful, comfortable, and very pleasant one. I loved my time in your city and have many to thank for it, but will mention in particular Florian Günther who happily showed me around town (and indeed country), Dennis Hessling who even in harried times–and he was the sys admin, so he had plenty of them–never lost his good cheer, Stefan Frijters without whose technical expertise I would have been lost, and Maarten Wouters who has always been a ready source of help in technical matters and who seems to sport a perpetual mischievous grin on his face, as though constantly planning something wicked.

Thanks also to the Institute for Multiscale Simulation headed by Prof. Dr. Thorsten Pöschel in the EAM Cluster of Excellence, for being very cooperative and pleasant fellow office-mates. Some memorable highlights of interaction with you included the regular Mensa lunches with Joanna Gargasz *neé* Smiglak, late night discussions with Nikola Topić, and that very funny group photography session led by Jonathan Köllmer.

This brings me to my own group in Erlangen (with scattered elements based in Stuttgart and now in Zagreb), or, as I have thought of it for a long time now, my family in Europe. I consider myself blessed to have known you all so closely and basked in the warmth of your hearts and the brilliance of your minds. You made sure that the vulnerable chap landing amidst an unfamiliar place and an alien culture was never made to feel less than at home, and for that I shall forever be grateful. I have spent so many special moments with so many of you that I'm afraid trying to describe their significance to me is as hopeless a task as portraying my emotion for my (original) family back in India–I could devour pages in my ardour to write and not have conveyed the least little bit of what I feel. I will nevertheless attempt both, for impossible as the tasks are, I will scarcely encounter more worthy ones. In roughly chronological order of first contact:

Waltraud Meinecke. Dear Walli, thank you for everything. Your help and

support to me began before I even arrived on these shores, and continue to this day, unbridled and unabated. Instances of your kindness are too frequent to list or even to count, and are not even the most remarkable thing about you: for me that would be the infinite good humour and cheer you have always displayed. Thank you for being such a constantly, reliably nice and fun person.

Sara Kaliman. One of my very favourite people in the world (if frequently maddening). You have been there from literally the beginning of my stay to the end, and I cannot imagine how it would have gone without you. I have learned an immense amount from you about everything in life outside the office, and look to you for advice in matters of taste and aesthetics, as in so many others.

Zoran Miličević. Your generosity is matched only by your reliability, and I look upon you as an elder brother. Our daily and discerning discussions of basketball were a needed pressure release, and I'd almost (though not quite!) anoint you as the one person to have a depth of knowledge of the NBA to outrival mine.

Zlatko Brkljača. A truly unique person (and all agree). Equal parts child, man, sage, and idiot, I see in your torments and your contradictions a soul brother. You are a giant, and–if in nothing else, in accordance with a pun that you remarkably never seem to stop making–so am I. We should have stridden galaxies together.

Karmen Čondić-Jurkić. Each time you arrived in town, it was as though you brought with you the fresh Šibenik sea breeze. My only complaint about your stays here was how short they always seemed; I'd love to have this grouse again.

Timo Bihr. By your reserved manner, few would suspect you of being a party animal, but I know better. I have seen enough instances of you out and about, in all states of tipsiness (and, ahem, undress), and never heard you decline an invitation to go out. In more everyday settings, your quiet calm voice kept everyone sane.

Daniel Schmidt. The other half of the Timo-Mimo duo, you are quite the opposite in your constant enthusiasm and urge to be *moving*. I admire your straightforwardness, friendliness, and most of all your generosity and willingness to help all who are around you, from which I have myself benefitted on many an occasion.

Mislav Cvitković. I admire everything about you, and it gives me a special happiness to see you prosper, for I see a bit of the ideal me in you. May you continue to be happy and successful (an instance of the optative mood, as I learned from you, my teacher of linguistics) in however it is you decide to affect your community. When I grow up, I want to be you.

Dragana and Damir Vurnek. You make a great couple, so much so that I cannot contemplate the one without being put in mind of the other. And now, of course, without immediately having my thoughts run to Elin, who may be my favourite Vurnek of all (which is saying something). Thanks for your unceasing generosity.

Robert Stepić. The coolest guy this side of Elvis, if given to an unfortunate (and hilarious) tendency to troll. Every day in the office is a lighter and more fun one because of you, and, talking to you, things never seem *that* bad. Thank you

for being this way.

Rachel and Robert Blackwell. These past months of getting to know you have been as enjoyable as they have been enlightening. I admire your clarity of opinion and expression (especially Rob's) and effusive and welcoming manner (especially Rachel's), and look forward to more exchanges of culture and worldview.

Past and current undergraduate students: Laura Merchant, Robert Pecoraro, Thomas Kiendl, Matthias Späth, Wolfgang Barfuß, Oleg Trosman, Thomas Scheel, David Jung, Henning Stumpf and Simone Gehrer. It has been a pleasure to have you young ones around, teaching all us old hands a thing or two about how things are done, and lightening up the office with your chatter and enthusiasm.

The new arrivals: Adriana Lepur and Maryam Aliee. Knowing you has been a pleasure so far and I look forward to deepening our acquaintance.

The Zagreb crowd, too many to list. Each time you guys came here it enlivened things up tremendously. A special mention both of Marko's very smooth, and David's very wild, dancing skills, as seen in Zoran and Zlatko's PhD defense party, each of which was delightful to watch. That was one night I'll not forget.

That about covers the group. I would also like to express my great gratitude to a few people whose friendship was crucial both to my health and my happiness here. The most prominent of these were Anika Bosse, Ruben Piepgras, Phani Kumar, Ruby Shepherd and Yassine Ben Yaakoub. Happy days spent with each of you helped lighten up my life tremendously, and I'll always be very fond, and, at some level, in debt, of each of you.

Lastly, but most importantly, there is the indescribable contribution of my family and friends back home in India in whatever I may do (India, wherever I am, will always be 'back home'). It is a simple fact that if not for the unwavering support, encouragement, belief and sacrifice of not just my parents but of a lot of my extended family, I would be very far from embarking on a project as daunting as a PhD, let alone finishing one. In particular, I would like to mention the love and support of my parents, my sisters (and my sister's family), my grandparents, my aunts, my uncles and my cousins. I could not truly thank any of them in words, but I hope to do so by my actions as long as I live.

In addition my friends from back home have also spurred me on, and, left perplexed by my often disappearing underground, have regularly asked after my well-being. Some of them I have been fortunate to know for two decades now, and I hope this is just the beginning of our relationship.